DOE/ET-0065/4

Damage Analysis and Fundamantal Studies

Quarterly Progress Report

OCT- DEC. 1978 ~~January-March, 1978~~

May 1979

U.S. Department of Energy
Assistant Secretary for Energy Technology
Office of Fusion Energy

DOE/ET-0065/4
uc-20. *20c*

Damage Analysis and Fundamantal Studies

Quarterly Progress Report
January-March, 1978

May 1979

U.S. Department of Energy
Assistant Secretary for Energy Technology
Office of Fusion Energy
Washington, DC 20545

Available from:

National Technical Information Service (NTIS)
U.S. Department of Commerce
5285 Port Royal Road
Springfield, Virginia 22161

Price: **Printed Copy:** $ 9.50
Microfiche: $ 3.00

FOREWORD

This report is the fourth in a series of Quarterly Technical Progress Reports on *"Damage Analysis and Fundamental Studies"* (DAFS) which is one element of the Fusion Reactor Materials Program, conducted in support of the Magnetic Fusion Energy Program of the U. S. Department of Energy. Other elements of the Materials Program are:

- *Alloy Development for Irradiation Performance (ADIP)*
- *Plasma-Materials Interaction (PMI)*
- *Special Purpose Materials (SPM).*

The DAFS program element is a national effort composed of contributions from a number of National Laboratories and other government laboratories, universities, and industrial laboratories. It was organized by the Materials and Radiation Effects Branch, Office of Fusion Energy, DOE, and a Task Group on *Damage Analysis and Fundamental Studies* which operates under the auspices of that Branch. The purpose of this series of reports is to provide a working technical record of that effort for the use of the program participants, for the fusion energy program in general, and for the Department of Energy.

This report is organized along topical lines in parallel to a Program Plan of the same title (to be published) so that activities and accomplishments may be followed readily relative to that Program Plan. Thus, the work of a given laboratory may appear throughout the report. Chapters 1 and 2 report topics which are generic to all of the DAFS Program: DAFS Task Group Activities and Irradiation Test Facilities, respectively. Chapters 3, 4, and 5 report the work that is specific to each of the subtasks around which the program is structured: A. Environmental Characterization, B. Damage Production, and C. Damage Microstructure Evolution and Mechanical Behavior. The Table of Contents is annotated for the convenience of the reader.

This report has been compiled and edited under the guidance of the Chairman of the Task Group on *Damage Analysis and Fundamental Studies,* D. G. Doran, Hanford Engineering Development Laboratory, and his efforts, those of the supporting staff of HEDL and the many persons who made technical contributions are gratefully acknowledged. T. C. Reuther, Materials and Radiation Effects Branch, is the Department of Energy counterpart to the Task Group Chairman and has responsibility for the DAFS Program within DOE.

Klaus M. Zwilsky, Chief
Materials and Radiation
Effects Branch
Office of Fusion Energy

CONTENTS

CONTENTS (Cont'd)

CONTENTS (Cont'd)

CONTENTS (Cont'd)

CONTENTS (Cont'd)

CONTENTS (Cont'd)

CONTENTS (Cont'd)

FIGURES

CHAPTER 3

Helium Analyses of Be(d,n)-Irradiated Pure Elements

Neutron Flux Characterizations and Damage Analysis Studies

Cross Section Prediction

FIGURES (Cont'd)

FIGURES (Cont'd)

FIGURES (Cont'd)

FIGURES (Cont'd)

FIGURES (Cont'd)

FIGURES (Cont'd)

TABLES

CHAPTER 3

TABLES (Cont'd)

CHAPTER 4

CHAPTER 5

CHAPTER 1

OAFS TASK GROUP ACTIVITIES

I. PROGRAM

Title: Irradiation Effects Analysis (WH011/EDA)
Principal Investigator: D. G. Doran
Affiliation: Hanford Engineering Development Laboratory

II. OBJECTIVE

The objective of this work is to coordinate the activities of the DAFS Task Group.

III. RELEVANT DAFS PROGRAM PLAN TASK/SUBTASK

All tasks

IV. SUMMARY

A meeting of the DAFS Task Group, augmented by representatives of the DAFS programs supported by the Office of Fusion Energy, was held on October 30-31, 1978, in Germantown. The principal objectives were a review of current programs relative to high priority needs, and the initiation of an irradiation schedule for RTNS-II. A beginning was made on the first objective by reaching a concensus on what problems are of the highest priority and discussing strategy toward the solution of some of them. Problem areas designated high priority include:

- Assessment of the significance of the He/dpa ratio; associated rate effects (relationship of accelerated damage rate dual-ion irradiations to fission reactor irradiations).
- Interaction of helium with elements of the microstructure.
- Assessment of the damaging effects of high energy neutrons relative to fission energy neutrons; efficient utilization of RTNS-II.
- Identification of the factors affecting alloy stability in a fusion environment.

- Identification of the damage mechanisms affecting mechanical behavior in a fusion environment.
- Implementation of reactor irradiations to study the above.

Some evolution of programs toward a more concentrated attack on these problems can be seen. Concern was expressed over one area that appears to be receiving less, rather than more, attention. This is the behavior of helium in irradiated metals.

The initiation of an RTNS-II irradiation schedule led to the scheduling of an RTNS-II Users' Meeting at Lawrence Livermore Laboratory for December 1978 (see Chapter 2).

Planning is underway for a Workshop on Techniques for Radiation Damage Analysis to be held March 8-9, 1979, under the sponsorship of the Materials and Radiation Effects Branch of the Office of Fusion Energy. The objective is to acquaint OFE programs with state-of-the-art microstructural diagnostic techniques. The proceedings of the Workshop will be documented. The planning committee includes P. Wilkes, U. Wisconsin, J. A. Spitznagel, W-R&D Center, and F. V. Nolfi, ANL.

CHAPTER 2

IRRADIATION TEST FACILITIES

STATUS OF IRRADIATION TEST FACILITIES

I. Rotating Target Neutron Source-I1 (RTNS-II)

The first irradiations at the Lawrence Livermore Laboratory (LLL) are expected to begin in January 1979, using the small RTNS-I targets. Maximum neutron fluxes are expected to be about 2 x 10^{12} n/cm^2-s. Full power operation with the new 50 cm diameter targets will be delayed perhaps six months due to problems in their fabrication.

II. Fusion Materials Irradiation Test (FMIT) Facility

The FMIT to be built at HEDL utilizes a linear accelerator to provide a 100 ma beam of deuterons which is stopped in a flowing lithium target. The primary deuteron energy is 35 MeV, but provisions are made for alternative operation at a lower energy of about 20 MeV. The project will enter the Title 1 design stage in January 1979. Start of construction is targeted for early 1980 and operation in 1983-84. Design and development of the'accelerator has been assigned to the Los Alamos Scientific Laboratory (LASL). Research programs are underway at both HEDL and LASL to resolve uncertainties in the lithium target and accelerator designs.

I. PROGRAM

Title: Nuclear Data for FMIT (WH025/EDK)
Principal Investigator: R. E. Schenter
Affiliation: Hanford Engineering Development Laboratory (HEDL)

II. OBJECTIVE

The objective of this work is to supply immediate nuclear data needs for the design and operation of the Fusion Materials Irradiation Test (FMIT) facility.

111. RELEVANT DAFS PROGRAM PLAN TASK/SUBTASK

All tasks that are relevant to FMIT use, with emphasis upon:
SUBTASK II.A.2.3 Flux-spectra definition in FMIT
SUBTASK II.B.1.2 Acquisition of Nuclear Data

IV. SUMMARY

Measurements and calculations have been made of neutron spectra from 35 MeV deuterons on thick lithium. These results are not described here but may be found in the section on damage production.

Measurements of the total and nonelastic cross sections have been made for neutrons on iron, calcium, oxygen, and carbon for energies of 35, 40, and 50 MeV. The data were obtained at the University of California at Davis cyclotron laboratory for the purpose of improving the accuracy of nuclear data for FMIT neutron transport calculations (e.g. shielding and calculational dosimetry) and for damage analysis.

V. ACCOMPLISHMENTS AND STATUS

A. High Energy Neutron Cross Sections for Transport and Damage Calculations -- F. P. Brady, C. Zanelli, J. L. Romero, J. L. Ullmann, P. O. Urone (U.C. Davis) D. L. Johnson (HEDL)

1. Introduction

Neutron transport calculations require extensive nuclear data for neutrons as a function of energy including differential elastic scattering cross sections, differential neutron emission spectra, and nonelastic cross sections for all important materials. Damage calculations also require elastic scattering and neutron emission data.

For FMIT, these data are required for neutron energies up to about 50 MeV. For transport calculations in the FMIT test cell (calculational dosimetry) and for damage calculations in similar spectra, data will be required to about 35 MeV for important structural materials such as iron, nickel, and chromium. For transport calculations of FMIT shielding through thick concrete, the dose is dominated by neutrons near the highest energies in the spectrum (up to ~50 MeV). Important elements for shielding are oxygen, iron, silicon, calcium, and carbon.

There is an extreme lack of data for neutron energies greater than ~14 MeV. Although there is a fair amount of data on neutron total cross sections up to 50 MeV, there is almost nothing for the other data.

Our immediate goal was to supply data for use in FMIT shielding calculations because of the impending finalization of wall specifications and because of the possibility for substantial cost savings to the FMIT project from reduced concrete requirements.

The plan is to make a few measurements in the high energy region, then to use theoretical optical model analyses to provide an evaluation of all required data as a function of neutron energy.

2. Measurements at U.C. Davis

We have made accurate measurements of the total cross section for neutrons on iron and calcium for nearly monoenergetic neutrons of about 35, 40, and 50 MeV. We are unaware of any previous data for calcium in this energy range.

We have also taken data that will yield the nonelastic cross section for neutrons on iron, oxygen, calcium, and carbon at energies of about 40 and 50 MeV.

Preliminary data have also been obtained on the differential elastic scattering for 40 MeV neutrons on iron.

VI. REFERENCES

None.

VII. FUTURE WORK

Optical model analysis of high energy neutron total, elastic, and non-elastic cross sections will be initiated in early FY 1979 in order to provide an evaluation of these data for energies greater than available in ENDF/B-V (20 MeV) for elements in FMIT shielding calculations. The data currently available may be too limited, therefore measurements of differential elastic scattering cross sections in the energy range of 20 - 50 MeV are being considered.

Additional measurements (at U.C. Davis) and calculations are planned of activation of LINAC accelerator structural materials by deuterons up

to 35 MeV and by neutrons up to 50 MeV. These data are needed to help define activity levels in the vicinity of the accelerator, however some of the data may be of use for future FMIT dosimetry needs.

Measurements and calculations are also envisioned for production of neutrons and gamma rays by deuterons incident upon accelerator and beam transport materials.

All experimental data will be used to check and modify nuclear model predictions.

VIII. PUBLICATIONS

None.

CHAPTER 3

SUBTASK A: ENVIRONMENTAL CHARACTERIZATION

I. PROGRAM

Title: Dosimetry and Damage Analysis
Principal Investigator: L. R. Greenwood
Affiliation: Argonne National Laboratory

II. OBJECTIVE

To develop dosimetry technique and to provide dosimetry and damage analysis for materials experiments at Be(d,n) facilities.

III. RELEVANT OAFS PROGRAM PLAN TASK/SUBTASK

SUBTASK II.A.2.1 Flux spectral definition in Be(d,n) field

IV. SUMMARY

Dosimetry was provided for Battelle Pacific Northwest Laboratories (PNL) at the U. C. Davis cyclotron (Be(d,n), E_d = 40 MeV) during September, 1978. Foil packets were irradiated at about 6 mm from the source to a fluence of about 5.8 x 10^{17} n/cm^2 and at 26 mm to 9.4 x 10^{16} n/cm^2.

Foil counting and analysis has been completed for an extensive field mapping study at U. C. Davis (Be(d,n), E_d = 30 MeV). Results are now being integrated with foil data from Lawrence Livermore Lab (LLL) and helium accumulation data from Rockwell International (RI).

V. ACCOMPLISHMENTS AND STATUS

A. Experiments at the U. C. Davis cyclotron, Be(d,n), E_d = 30-40 MeV-
L. R. Greenwood and R. R. Heinrich

An irradiation was conducted during September for R. Jones and D. Styris (PNL) at the U. C. Davis cyclotron at E_d = 40 MeV. Tensile wires and dosimetry foils were irradiated at two locations, about 6 and 26 mm from the center of the neutron source. The Co, Nb, Fe, Ni, Zr, and Au dosimetry foils are being counted at ANL and the Al and some Ni foils have been counted at LLL. Preliminary results for the 36 hour run at an average current of 25.4 μA indicate maximum fluences over the length of a tensile wire of about 5.8 x 10^{17} n/cm^2 in the front position and 9.4 x 10^{16} n/cm^2 in the rear location.

An extensive field mapping study was conducted at U. C. Davis (Be(d,n), E_d = 30 MeV) in July 1977. Irradiated specimens were placed close to the target and on 5, 15, and 30 cm arcs. Helium accumulation monitors have now been analyzed at RI and dosimetry foils have been counted at LLL and ANL. All dosimetry foils are now being weighed at RI to insure consistency. All of the data will then be integrated to obtain a flux-spectral map.

VI. REFERENCES

None

VII. FUTURE WORK

A complete flux-spectral analysis with damage calculations and errors is planned at 24 different locations for the PNL irradiation. Selected Ni tensile specimens will also be counted to insure proper geometric corrections.

The E_d = 30 MeV effort with LLL and RI should be completed next quarter. Due to the large variety of specimens, excellent integral cross section comparisons will be obtained and helium data can be included in the dosimetry unfolding methodology.

VIII. PUBLICATIONS

The work for PNL will be presented at the First Topical Meeting on Fusion Reactor Materials, January 29–31, 1979, in Miami Beach, Florida.

I. PROGRAM

Title: Helium Generation in Fusion Reactor Materials
Principal Investigators: D. W. Kneff, Harry Farrar IV
Affiliation: Energy Systems Group, Rockwell International

II. OBJECTIVE

The objectives of this work are to measure helium generation rates of materials for Magnetic Fusion Reactor applications in the broad-band Be(d,n) neutron environment, to characterize the Be(d,n) neutron fluence and neutron energy distributions as a function of position relative to the neutron source, particularly in the high-flux region, and to develop helium accumulation fluence monitors for neutron fluence and energy spectrum dosimetry for fusion-program neutron irradiations.

III. RELEVANT DAFS PROGRAM PLAN TASK/SUBTASK

SUBTASK II.A.2.1	Flux-Spectral Definition in the Be(d,n) Field
SUBTASK II.A.4.3	Be(d,n) Helium Gas Production Data
SUBTASK II.A.5.1	Helium Accumulation Monitor Development

IV. SUMMARY

An additional 27 specimens of pure elements irradiated in the Be(d,n) neutron field using 30-MeV deuterons have been analyzed for helium. These specimens were multiple samples of Al, Fe, Ni, Cu, and Au from wire rings incorporated in the experiment for helium accumulation dosimetry and cross section measurements. Results from several of these and previously-analyzed specimens have been used to obtain a rough estimate of the relative helium generation rates for Al, Fe, Ni, and Cu.

V. ACCOMPLISHMENTS AND STATUS

Helium Analyses of Be(d,n)-Irradiated Pure Elements -- D. W. Kneff, Harry Farrar IV, and M. M. Nakata (Energy Systems Group, Rockwell International)

Helium analyses are continuing of the materials irradiated in the joint Rockwell International-Argonne National Laboratory (ANL)-Lawrence Livermore Laboratory (LLL) Be(d,n) irradiation experiment. The irradiation was conducted with the 76-inch isochronous cyclotron at the University of California at Davis using 30-MeV deuterons. The objectives of this irradiation experiment were to measure the spectrum-integrated helium generation cross sections of a large number of materials of potential fusion reactor design interest, characterize the Be(d,n) neutron environment in detail, and evaluate and use helium accumulation materials as neutron dosimeters. A detailed description of the experiment and the previous analysis results are given in previous Rockwell International reports.(1-3)

An additional 27 segments from the eleven Al, Fe, Ni, Cu, and Au pure element rings incorporated in the irradiation capsule were analyzed for helium during the report period. A total of 79 Be(d,n) helium analyses have now been made using the high-sensitivity gas mass spectrometer at Rockwell International. The results of these measurements have been used to estimate the relative helium generation rates for four of these materials: Al, Fe, Ni, and Cu.

The relative locations of the pure element wire rings are shown schematically in Figure 1, reproduced from Reference 1. The rings, labeled "dosimetry wire rings" in Figure 1, are shown in cross section as open circles. Each ring was oriented concentrically with the capsule axis, which in turn was aligned approximately with the neutron source axis. Figure 2 plots the helium generation results for six of these

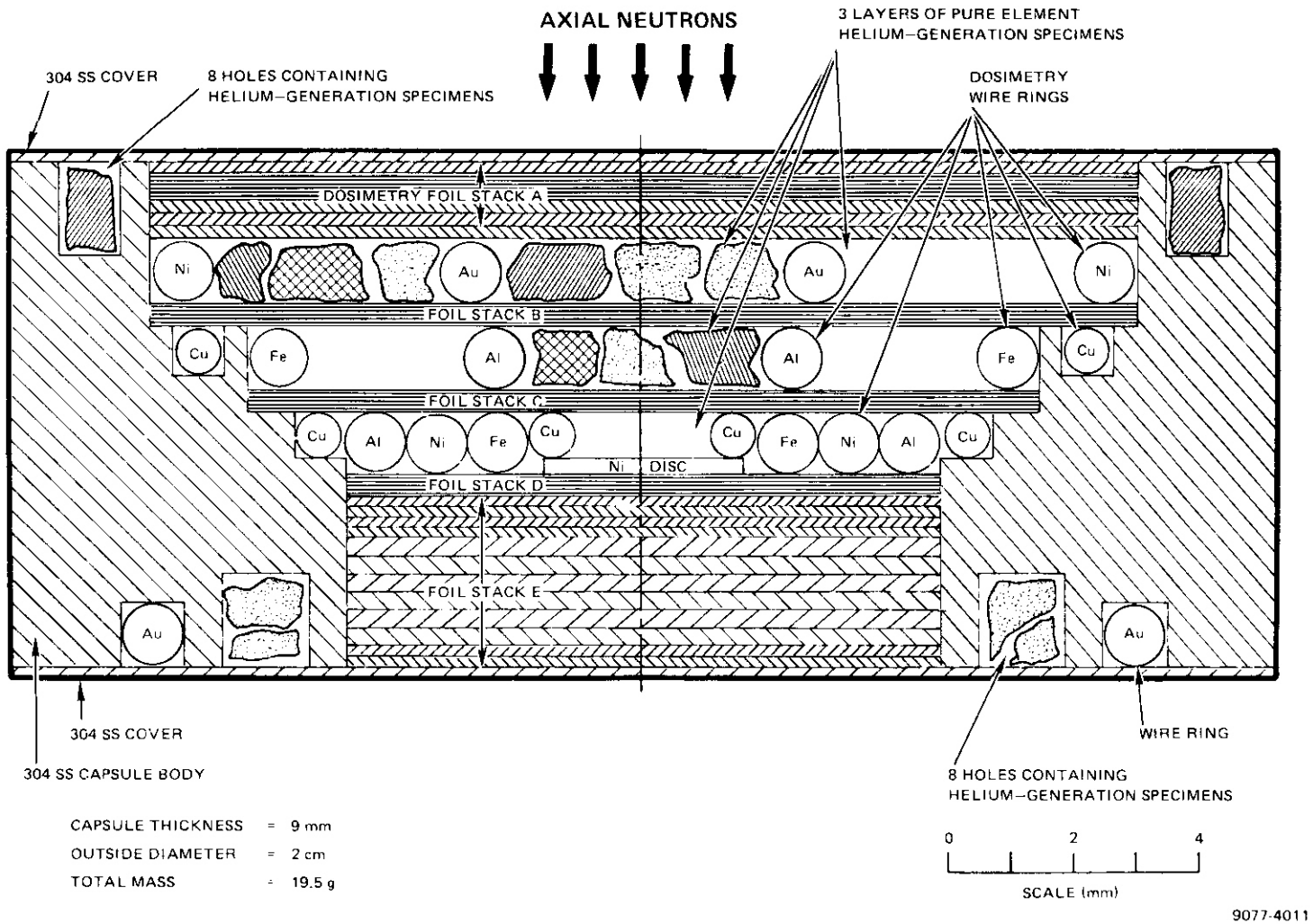

FIGURE 1 View of Capsule.

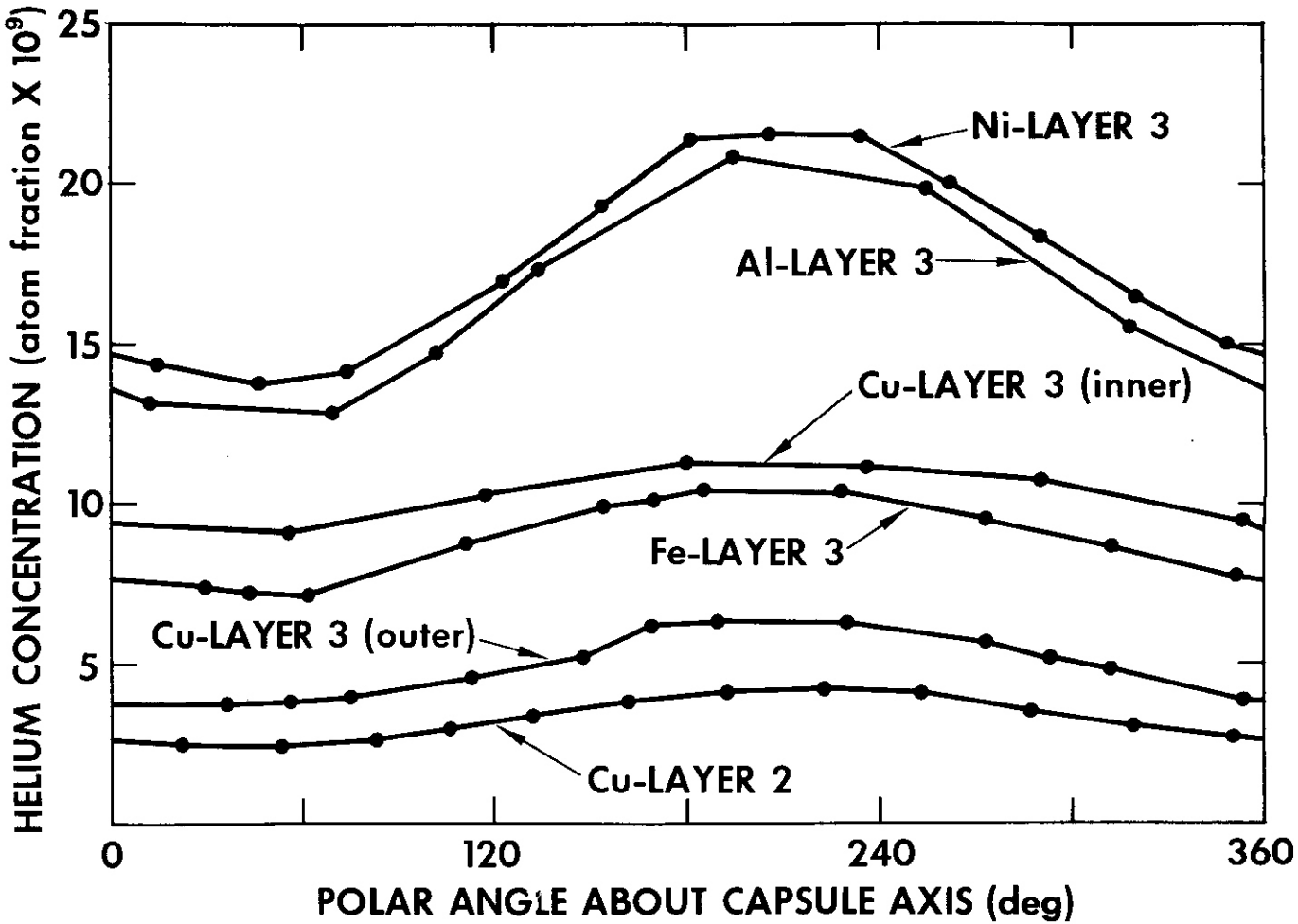

FIGURE 2 Measured Helium Generation in B(d,n)-Irradiated Pure Element Ring Segments

rings as a function of polar angle about the capsule axis. These rings include the five rings in Layer 3 (between foil Stacks C and D), and the copper ring from Layer 2 (below foil Stack B). All six rings were approximately the same distance from the beryllium target (~15 mm).

Examination of Figure 2 shows a consistent trend in all six curves: an approximate single-cycle sine wave with a broad maximum at ~210°. The shape is attributed primarily to a slight offset of the irradiation capsule from the time-averaged neutron source axis, with some contribution by nonuniformities in the wire rings'. The results from the helium accumulation dosimetry rings are significantly more sensitive to such an offset for this Be(d,n) experiment than observed for the T(d,n) experiment~,(~because of the steeper fluence gradients in the Be(d,n) field. Additional independent measurements of this offset will be made using microphotometer scans of a number of autoradiographs that were taken of several irradiated capsule foils immediately following the irradiation.

Figure 2 was used to estimate the ratios of the measured helium generation in these wires. The results are given in Table 1, normalized to nickel. Table 1 includes three sets of relative numbers: Column 2

Element	Be(d,n) Geometry-Corrected	T(d,n) RTNS-I (Reference 5)	EBR-II Core (Reference 6)
Ni	1	1	1
Fe	0.38	0.49	0.075
cu	0.41	0.52	0.076
Al	1.21	1.46	0.14

gives the measured ratios as determined directly from Figure 2 and corrected for the average neutron source angles intercepted by these rings; Column 3 gives the cross section ratios previously determined for the T(d,n) spectrum of the Rotating Target Neutron Source-I (RTNS-I);[5] and Column 4 gives, for comparison, the cross section ratios measured for an EBR-II core neutron spectrum.[6] The corrections to the Be(d,n) ratios were based on the relative Be(d,n) neutron fluxes measured as a function of angle for 33-MeV deuterons by Meulders, et at.[7] The Layer 3 rings intercepted average angles ranging from 5^{o} to 19^{o}, and the Layer 2 copper ring intercepted an average angle of $\sim 28^{o}$. The helium generation ratios for the three individual copper rings, averaged in Table 1, were 0.43 (Layer 3 inner ring), 0.36 (Layer 3 outer ring), and 0.43 (Layer 2 ring). Their agreement suggests that the copper total helium generation cross section relative to that of nickel is not very sensitive to the shape of the Be(d,n) neutron energy spectrum. Comparison of the corrected Be(d,n) results (Column 2) with the T(d,n) results (Column 3) indicates that the *relative* helium generation rates in the two neutron environments are similar.

It must be cautioned that the Be(d,n) numbers presented in Table 1 are no more than initial estimates, and must be so interpreted. They treat several important factors in a very approximate manner; including the finite dimensions of the neutron source spot, differences in ring distance from the beryllium target, wire shape nonuniformities, capsule axis offset effects, and helium generation cross section variations with angle. These factors are important because of the steep neutron fluence and energy spectrum changes with neutron source angle. These ratios will be reevaluated (with consideration for energy spectrum changes), and the cross sections will be determined, when the neutron fluence/energy spectra are mapped out in detail.

Initial analyses of the gold dosimetry wire between foil Stacks A and B (Figure 1) indicate that this gold ring had a total helium generation of only ~0.3 appb (3×10^{-10} atom fraction). This is a factor 60

less than that of nickel - without making corrections for the gold's significantly closer irradiation distance - and the levels of helium released by segments of wire (–6 x 10^9 atoms) were too small for accurate measurement at this time. Gold thus appears to be less useful as a dosimeter for short-term irradiations such as the present 93-hour experiment, which had a total fast (>6 MeV) neutron fluence of ~10^{17} n/cm^2 at the center of the capsule assembly.

A series of helium analysis runs was also made during the report period to establish optimum procedures for analyzing chromium and tin with the high-sensitivity gas mass spectrometer. Mass spectrometer analyses have subsequently been initiated for both T(d,n)- and Be(d,n)-irradiated chromium, but the results are not yet available. The weighing of the radiometric dosimetry foil segments counted by LLL for the Be(d,n) experiment was also completed at Rockwell International during this period, and the results were transmitted by letter to LLL.

VI. REFERENCES

1. D. W. Kneff and H. Farrar IV, Helium Generation in Fusion Reactor Materials, Technical Progress Report for Period April - September 1977, AI-DOE-13219, Atomics International, Canoga Park, CA, January 1978.

2. D. W. Kneff, H. Farrar IV, and M. M. Nakata, "Helium Generation in Fusion Reactor Materials," in Damage Analysis and Fundamental Studies, Quarterly Progress Report April - June 1978, DOE/ET-0065/2, U.S. Department of Energy (in press).

3. D. W. Kneff, H. Farrar IV, and M. M. Nakata, "Helium Generation in Fusion Reactor Materials," in Damage Analysis and Fundamental Studies, Quarterly Progress Report July - September 1978, DOE/ET-0065/3, U.S. Department of Energy (in press).

4. D. W. Kneff and H. Farrar IV, "Helium Generation in Fusion Reactor Materials," in Damage Analysis and Fundamental Studies, Quarterly Progress Report January - March 1978, DOE/ET-0065/1, U.S. Department of Energy, August 1978.

5. H. Farrar IV and D. W. Kneff, "Helium Generation in Twelve Pure Elements by 14.8-MeV Neutrons," Trans. Am. Nucl. Soc. 28, 197 (1978).

6. E. P. Lippincott, W. N. McElroy, and H. Farrar IV, "Helium Production in Reactor Materials," in Nuclear Cross Sections and Technology, Vol. I, R. A. Schrack and C. D. Bowman, eds., pp. 375-377, National Bureau of Standards Special Publication 425, U.S. Department of Commerce (1975).

7. J. P. Meulders, P. Leleux, P. C. Macq, and C. Pirart, "Fast Neutron Yields and Spectra from Targets of Varying Atomic Number Bombarded with Deuterons from 16 to 50 MeV," Phys. Med. Biol. 20, 235 (1975).

VII. FUTURE WORK

The helium analyses of the Be(d,n)-irradiated pure elements will continue, with initial emphasis placed on chromium helium-generation specimens; and additional nickel and iron wire segments at varying irradiation angles. Mapping of the Be(d,n) neutron fluence and neutron energy profiles as a function of position in the irradiation capsule will begin, based on the ANL and LLL radiometric counting results and the helium accumulation dosimetry information. The final map will be combined with the helium analyses of the other pure element specimens to determine helium-generation cross sections for this neutron environment.

VIII. PUBLICATIONS

None.

I. PROGRAM

Title: Damage Analysis and Dosimetry Radiation Damage Analysis
Principal Investigator: A. N. Goland
Affiliation: Brookhaven National Laboratory

II. OBJECTIVE

Radiation damage analysis studies associated with the use of electrical insulators in fusion reactors.

III. RELEVANT DAFS PROGRAM PIAN TASK/SUBTASK

SUBTASK II.A.2.4 Flux Spectral Definition in FMIT.

SUBTASK **II.B.l** Calculation of Displacement Cross Sections.

IV. SUMMARY

The variation of recoil-atom damage and gas production with depth in a test assembly located adjacent to a Li(d,n) neutron source has been evaluated with the damage code DON. Neutron fluxes within the assembly have been determined with the neutron transport code MORSE incorporating a source routine to generate neutrons from Li(d,n) reactions. Damage calculations have been made for C, Al, and Fe using the modified Kinchin-Pease relation and for Al_2O_3 and Si_3N_4 using the total displacement functions of Parkin and Coulter.

V. ACCOMPLISHMENTS AND STATUS

A. Neutron Flux Characterizations and Damage Analysis Studies --

A. N. Goland, H. C. Berry, G. F. Dell, and O. W. Lazareth (BNL)

1. Neutron Generation

A description of the method of generating neutrons from Li(d,n) reactions has been reported previously.[1] The method has been updated to achieve better agreement at large angles with the spectra measured by Saltmarsh et al.[2] An estimate of the total neutron yield from 40 MeV deuterons was obtained by extrapolating Saltmarsh's time of flight yields beyond 90^{o} and by integrating over the total solid angle. This estimated total yield was fitted to the total yields at lower energies[3] and a value of 2.2×10^{17} neutrons/Coulomb was obtained for the total yield of neutrons from 30 MeV deuterons on lithium. This conversion factor has been used in obtaining the flux values reported below.

2. Flux Estimators

In the past an upper limit was placed on the magnitude of an individual flux contribution from the probabilisitic flux estimators used in MORSE. This limit was used to avoid unreasonably large flux contributions when the distance between a neutron and a given detector was quite small. Limitation of the magnitude of the flux estimate resulted in the initial increase of the damage with depth that was reported previously.[1] This limitation is no longer used. Singularities in the probabilistic flux estimators are now avoided by limiting the minimum neutron-detector distance to an arbittary value of 1 mm and of removing any limitation to the magnitude of the flux estimate. With this change in the flux estimators, the collided flux at first increases, but the uncollided and the total flux decrease with increasing depth in in the test assembly, Fig. 1.

3. Gamma Generation

Estimates of the gamma ray flux and the gamma ray spectra have been obtained by using MORSE to solve the coupled neutron-gamma ray transport problem. At each collision point a test for gamma generation is performed. Whenever a gamma ray is generated, it is stored in the particle bank while the history of the parent neutron is completed. Each gamma ray is considered as a separate particle and is followed throughout its history using the same techniques and the same flux estimators that are used for neutrons. The dependence of the neutron and gamma ray fluxes upon depth within a test assembly is shown in Fig. 2, and the neutron and gamma ray spectra at a point near the lithium source are shown in Fig. 3.

4. Damage Calculations

The influence on the neutron spectra of the material in a typical test assembly has been simulated by using MORSE with the cross sections of Alsmiller and Barish[4] to determine the neutron spectra at several depths within a 30 x 20 x 20 cm^3 block of iron located adjacent to the lithium target. At each depth the recoil-atom damage and the gas generation have been determined for several materials by using the appropriate neutron spectrum as input to the damage program DON. Cross sections used with DON are ENDF/B-IV cross sections for neutron energies up to 20 MeV. Above 20 MeV, the cross sections are equated to their value at 20 MeV.

Damage calculations were performed for the monatomic materials C, Al, and Fe. Displacements for these materials were related to damage energy $\nu(T)$ by the usual relation:

$$N_{dis} = \frac{0.8\nu(T)}{2\,E_d}$$

The spectrum averaged displacement cross sections as well as the spectrum averaged cross sections for gas generation have been determined for C, Al, and Fe with E_d = 25 eV. The values of these quantities at a depth of 1 cm within the test sample is given in Table 1.

Recoil-atom damage and gas generation in the binary insulators Al_2O_3 and Si_3N_4 were calculated by using in DON the total displacement functions for these materials as generated by Parkin and Coulter[5]. For binary materials there are four total displacement functions that give the number of displacements of each atomic species that are produced by primary knock-on atoms of each species. For example, displacements of aluminum atoms in Al_2O_3 were obtained by using the appropriate total displacement functions to determine the number of aluminum atoms displaced by aluminum PKA's and the number of aluminum atoms displaced by oxygen PKA's. These displacements were then weighted according to the atomic fractions of Al and O in Al_2O_3 and were then summed to give the total number of aluminum displacements in Al_2O_3. The process was then repeated for oxygen using the appropriate displacement functions to obtain the number of oxygen atoms that are displaced.

Gas generation in binary materials was determined from the weighted sum of the gas generation from each species. A comparison of the total gas generation in Al_2O_3 and in Si_3N_4 is shown in Fig. 4, and recoil-atom damage and gas generation for these two binary insulators are listed in Tables 2 and 3 respectively.

Based upon the criterion of gas generation, Al_2O_3 should be a better insulator candidate material than Si_3N_4. However, the spectrum averaged displacement cross section for Al in Al_2O_3 is more than twice as large as the spectrum averaged displacement cross section for either Si or N in Si_3N_4. Based on the criterion of displacements, Si_3N_4 should be a better insulator candidate material than Al_2O_3. This latter result

depends upon the displacement energies used in generating the total displacement functions. These displacement energies are listed below.

	E_d(eV)
Al	18
O	72
Si	60
N	60

The value of E_d previously used for the displacement energy of A3 in Al_2O_3 was E_d = 40 eV.[5] However, Phillips[6] has recently reported a value of E_d = 18 eV for Al in Al_2O_3, and this lower value of E_d has been used in generating the total displacement functions for Al_2O_3. Use of this lower value of E_d is reflected in the large spectrum averaged displacement cross section of Al in Al_2O_3. Hence the displacement cross section for aluminum may be large.

Evaluation of an insulator candidate material on the basis of gas generation seems to be straightforward. Evaluation of a material on the basis of displacements is more complicated and is made uncertain both by uncertainties in displacement energies as well as by the possibility of displacements arising from ionization processes in insulators. Both of these sources of uncertainty need further investigation.

VI. REFERENCES

1. A. N. Goland, Damage Analysis and Fundamental Studies Quarterly Technical Progress Report July - September 1978, DOE/ET-0065/3, p. 29.

2. M. J. Saltmarsh, C. A. Ludemann, C. B. Fulmer, and R. C. Styles, Nuclear Instruments and Methods 145, p. 81 (1977).

3. P. J. Persiani, W. Becker, and J. Donahue, Symposium on Neutron Cross-Sections from 10 to 40 MeV, Brookhaven National Laboratory, May 3-5, 1977, BNL-NCS-50681, p. 151.

4. R. G. Alsmiller, Jr. and J. Barish, Neutron-Photon Multigroup Cross Sections for Neutron Energies ≤ 60 MeV., ORNL/TM-6486, August 1978.

5. D. M. Parkin and C. A. Coulter, Damage Analysis and Fundamental Studies Technical Progress Report January - March 1978, DOE/ET-0065/1, p. 113.

6. G. P. Pells and D. C. Phillips, The Temperature Dependence of the Displacement Threshold Energy of α - Al_2O_3, AERE-R9138, August 1978.

7. Proceedings of the Meeting on CTR Electrical Insulators, May 17-19, 1976 at Los Alamos Scientific Laboratory, CONF-760558, p. 5.

VII. FUTURE WORK

Future work will include a survey of recoil-atom damage and gas generation in binary and ternary insulators of interest for fusion reactors.[7] In addition the treatment of damage will be extended to include recoil damage resulting from the scattering of energetic electrons produced by Compton scattering of and pair production from energetic gamma rays. Damage resulting from ionization induced by gamma rays as well as by charged particles produced in reactions such as (n,p) and (n,α) is to be considered.

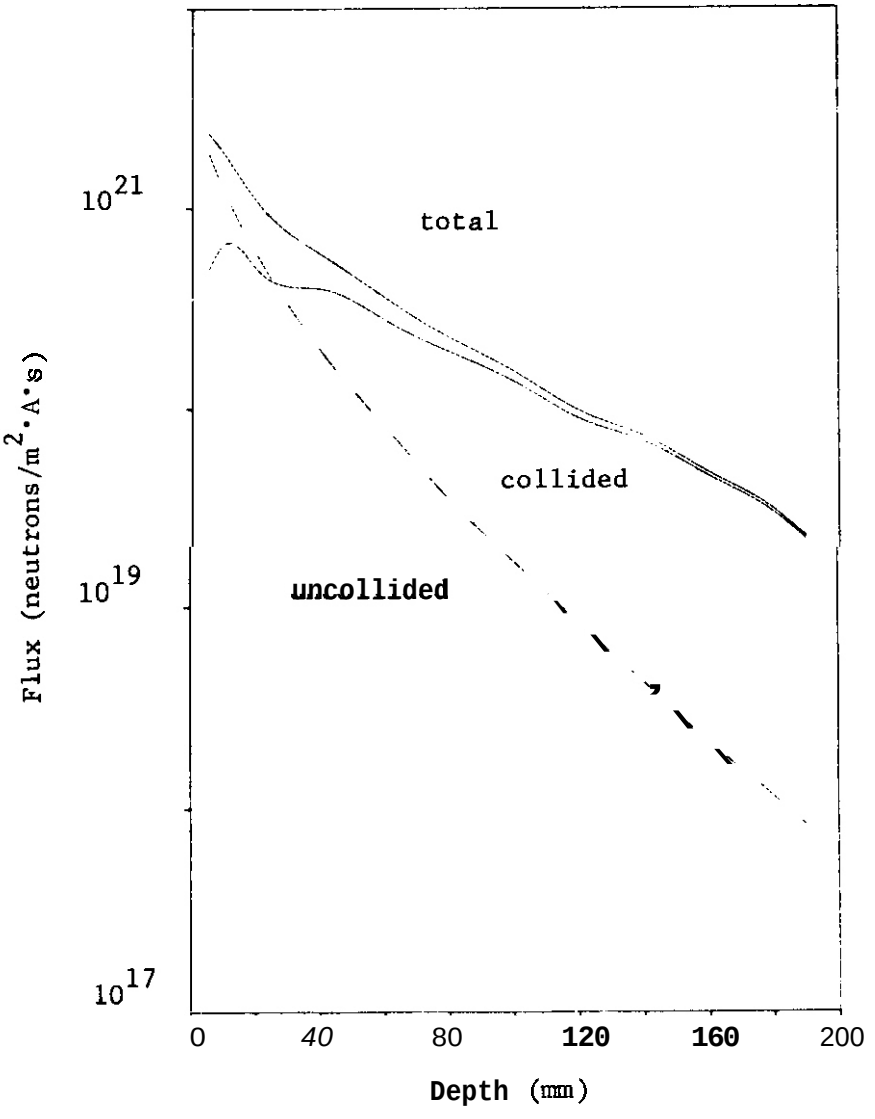

FIGURE 1. **Variation with depth in the test assembly of the uncollided, collided, and total neutron flux.**

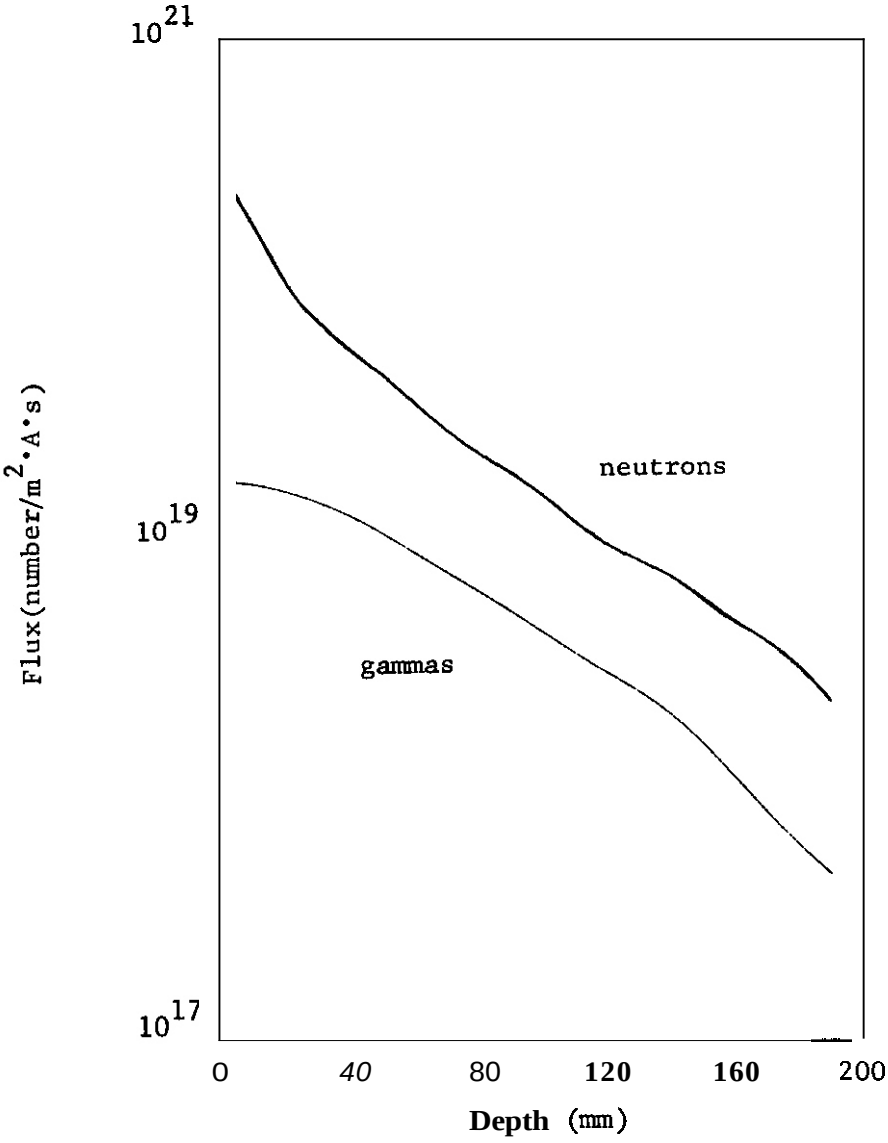

FIGURE 2. **Variation with depth in the test assembly of total neutron and gamma ray fluxes.**

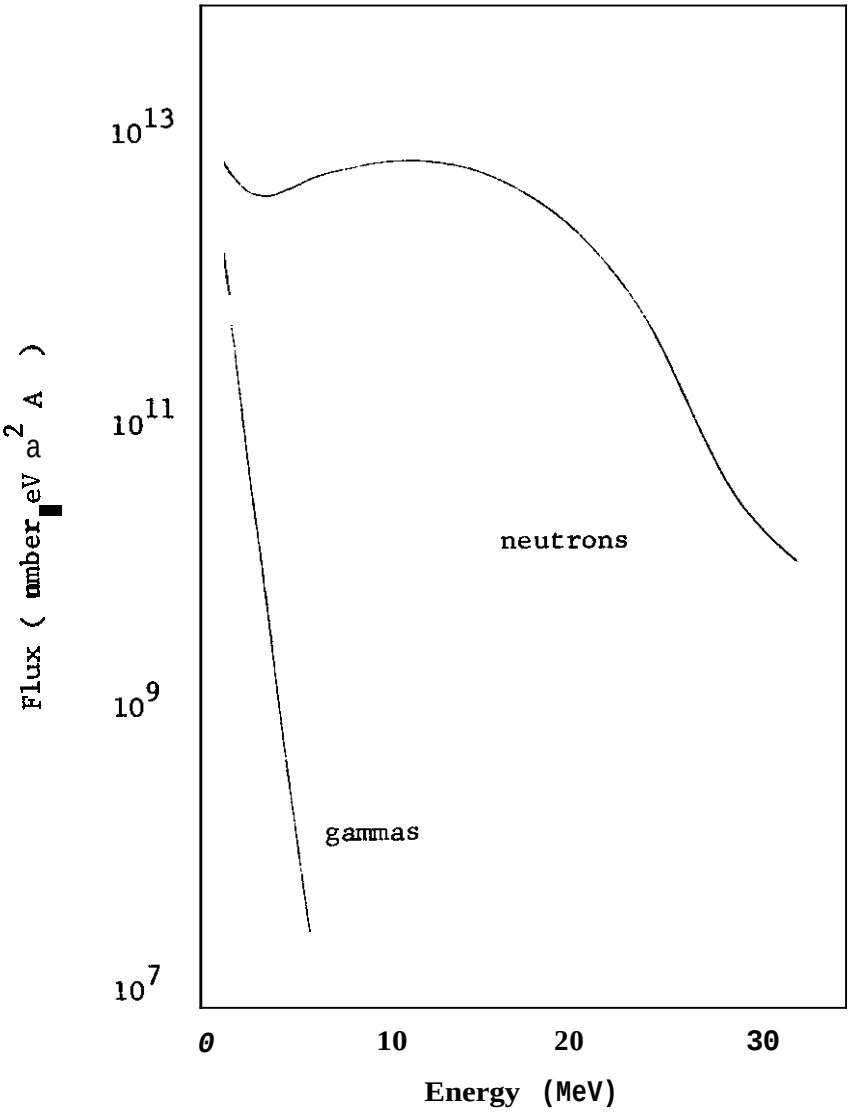

FIGURE 3. **Neutron and gamma ray spectra at a depth of 5 mm within the test assembly.**

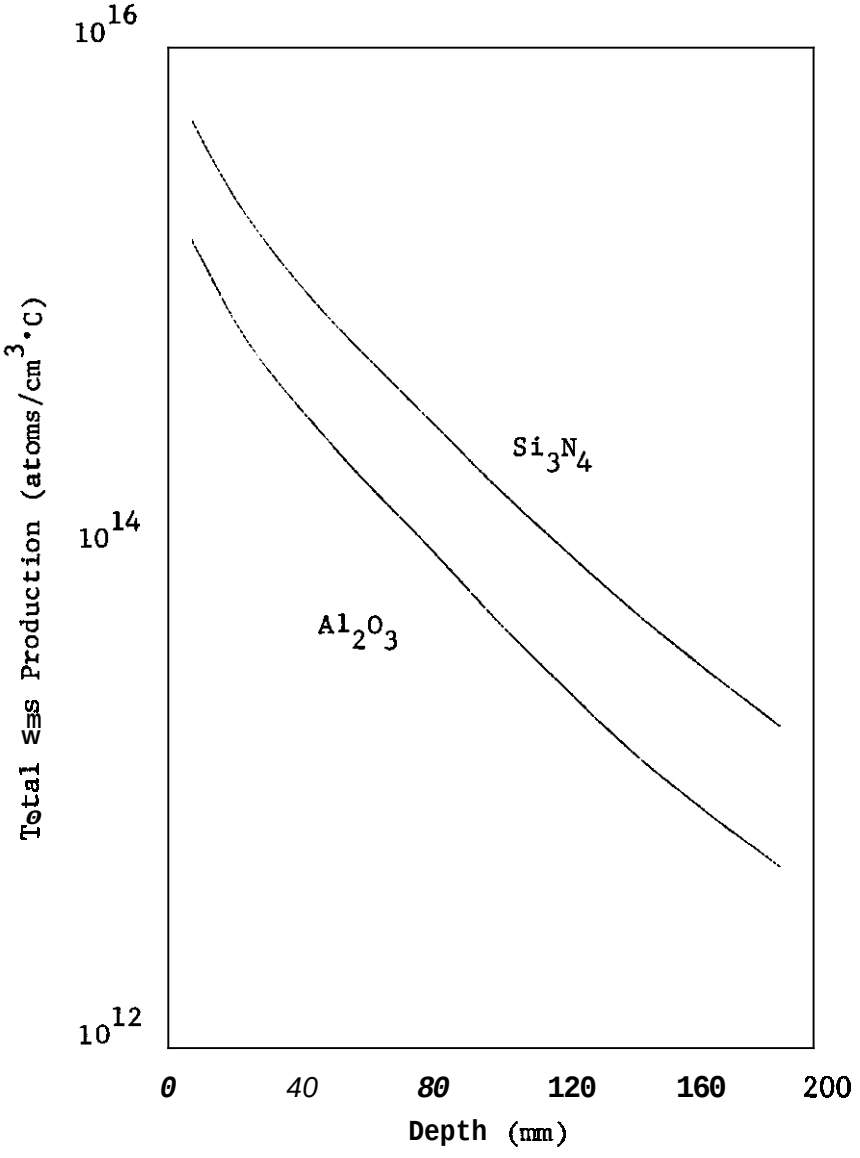

FIGURE *4*. **Variation with depth in the test assembly of the total gas generation in Al_2O_3 and Si_3N_4.**

TABLE 1.

Spectrum averaged displacement and gas production cross sections for C, Al, and Fe at a sample depth of 10 mm.

Material		C	Al	Fe
Flux (10^{20} $\frac{\text{neutrons}}{\text{m}^2 \cdot \text{C} \cdot \text{s}}$)		1.87	1.87	1.87
$\bar{E}_n$	(MeV)	11.27	11.27	11.27
$\bar{\sigma}_d$	(kb)	0.751	2.312	3.464
$\bar{\sigma}_H$	(mb)	-	39.1	109.9
$\bar{a}_D$	(mb)	-	9.90	10.6
$\bar{a}_T$	(mb)	-	3.60	6.39
$\bar{\sigma}_{^4He}$	(mb)	52.0	39.9	29.3
$\bar{\sigma}_t$ (gas)	(mb)	52.0	92.5	158.2

TABLE 2.

Spectrum averaged displacement and gas production cross sections for Al_2O_3

Sample depth (mm)		5.0	10.0	20.0	40.0	80.0	140.0	190.0
Flux (10^{20} $\frac{\text{neutrons}}{m^2 \cdot C \cdot s}$)		2.38	1.87	1.09	0.587	0.224	0.0722	0.0226
$\bar{E}_n$	(MeV)	11.04	11.27	8.93	8.27	6.21	3.50	3.60
$\bar{\sigma}_d$(Al)	(kb)	1.067	1.073	1.025	0.996	0.932	0.782	0.869
$\bar{\sigma}_d$(O)	(kb)	0.411	0.413	0.395	0.385	0.361	0.304	0.337
$\bar{\sigma}_H$	(mb)	23.7	23.0	21.7	18.9	13.7	6.85	7.13
$\bar{\sigma}_D$	(mb)	5.31	5.54	5.00	3.85	3.07	1.57	1.78
$\bar{\sigma}_T$	(mb)	1.29	1.44	0.990	0.902	0.660	0.361	0.358
$\bar{\sigma}_{^4He}$	(mb)	49.0	45.7	46.0	40.5	29.0	14.1	14.6
$\bar{\sigma}_t$(gas)	(mb)	73.9	75.7	73.7	64.1	46.5	22.9	23.9

TABLE 3.

Spectrum averaged displacement and gas production cross sections for Si_3N_4

Sample depth (mm)		5.0	10.0	20.0	40.0	80.0	140.0	190.0
Flux (10^{20} $\frac{\text{neutrons}}{m^2 \cdot C \cdot s}$)		2.38	1.87	1.09	0.587	0.224	0.0722	0.0226
$\bar{E}_n$	(MeV)	11.04	11.27	8.93	8.27	6.21	3.50	3.60
$\bar{\sigma}_d$(Si)	(kb)	0.365	0.366	0.345	0.329	0.290	0.229	0.246
$\bar{\sigma}_d$(N)	(kb)	0.423	0.421	0.398	0.380	0.335	0.266	0.285
$\bar{\sigma}_H$	(mb)	106.1	108.4	94.8	86.9	65.5	39.0	39.1
$\bar{\sigma}_D$	(mb)	10.4	10.1	9.86	8.15	6.11	2.98	3.20
$\bar{\sigma}_T$	(mb)	6.50	5.98	5.95	4.88	3.64	1.90	2.02
$\bar{\sigma}_{^4He}$	(mb)	127.7	127.8	111.8	101.6	75.5	42.7	43.1
$\bar{\sigma}_t$(gas)	(mb)	250.7	252.3	222.4	201.5	150.8	86.6	87.4

I. PROGRAM

Title: Nuclear Data for Damage Studies and FMIT (WH025/EDK)
Principal Investigator: R. E. Schenter
Affiliation: Hanford Engineering Development Laboratory (HEOL)

II. OBJECTIVE

The objective of this work is to supply nuclear data needed for damage studies and in the design and operation of the Fusion Material Irradiation Testing (FMIT) facility.

III. RELEVANT DAFS PROGRAM PLAN TASK/SUBTASK

SUBTASK	II.A.2.4	Flux Spectra Definition in FMIT
TASK	II.A.4	Gas Generation Rates
SUBTASK	II.A.5.1	Helium Accumulation Monitor Development
SUBTASK	II.B.1.2	Acquisition of Nuclear Data

IV. SUMMARY

The computer code HAUSER, which predicts nuclear cross sections, has been modified to include pre-equilibrium and statistical direct effects, enabling cross sections to be calculated to above 50 MeV.

The thick target neutron yield from 35 MeV deuteron bombardment of lithium has been experimentally determined for neutron energies greater than ~1 MeV for 10 angles ranging from 0 to 150 degrees. The microscopic neutron model used in predicting FMIT fluxes has been updated to include these new data.

V. ACCOMPLISHMENTS AND STATUS

A. Cross Section Prediction -- F. M. Mann (HEDL) and C. Kalbach (Triangle Universities Nuclear Laboratory)

The Hauser-Feshbach nuclear cross section prediction computer code HAUSER*4 has been extended (and renamed HAUSER*5) to include pre-equilibrium and statistical direct effects. Such effects become important for (n, nucleon) reactions above incident energies of ~10 MeV and for (n,α) reactions above ~15 MeV. As a test case, helium production resulting from neutron bombardment of copper for neutron energies between 10 and 40 MeV was calculated, $(n,\alpha\gamma)$, $(n,\alpha n)$, and $(n,n\alpha)$ reactions were explicitly calculated for ^{63}Cu and ^{65}Cu, while $(n,\alpha p)$, $(n,p\alpha)$, $(n,2\alpha)$, and $(n,2n\alpha)$ were estimated using the cross sections named above and other explicitly calculated cross sections. There is excellent agreement for $^{63}Cu(n,\alpha\gamma)^{60}Co$ between ENDF/B-IV (which is heavily based on experiment) and the calculations. As seen in Figure 1, the calculations for total helium production from copper agree well with experiments at 14.8 MeV (Farrar and Kneff[1] and Grimes et al.[2]) but are lower than the only other available data, calculations from ORNL[3].

The calculation of recoil spectra and hence of damage cross sections for high incident neutron energies has been hindered by the very limited ability to calculate angular distributions for nonelastic events. Systematic trends have now been observed which will allow calculation of the angular distribution and hence recoil energy of the residual nuclei.

B. Neutron Yield Experiments -- D. L. Johnson, F. M. Mann (HEDL) J. Watson, J. Ullmann, and W. G. Wyckoff (University of California at Davis

In order to provide calculational dosimetry for the FMIT facility, a microscopic neutron yield model heavily based on experimental data is

needed. Therefore, thick target d + Li neutron yields measurements have been conducted using the 76 inch cyclotron of the Crocker Nuclear Laboratory at the University of California at Davis. Neutrons produced by the 35 MeV deuterons incident upon the 2 cm thick * 2.5 cm diameter lithium were detected by a 5.0 cm * 5.0 cm diameter NE213 liquid scintillator, whose efficiency was calculated and measured. Neutron energy determination was by the time-of-flight method with pulse shape discrimination between gamma ray and neutron events employed. Measurements for θ = 0, 4, 8, 12, 20, 30, 45, 70, 105, and 150 degrees were taken with two flight path lengths to maximize neutron energy resolution, allowing neutron energies as low as $\sim$1 MeV and as high as 50 MeV (the maximum energy available in the reaction) to be measured. Typical preliminary results are shown in Figure 2. Because of the extreme sensitivity of the detector efficiency near the detection threshold, the neutron yield below 2 MeV is more uncertain than for higher energies as seen in Figure 3. In December, preliminary runs aimed at this region were concluded.

C. Microscopic Neutron Yield Model -- F. M. Mann (HEDL)

A microscopic neutron yield model ($d^3\sigma/dE_d dE_n d\Omega$) based on the Serber[4] and evaporation models was developed last year. With the analysis of the HEDL - U.C.D. d + Li experiment, it became obvious that the normalizations used in the model, 40 MeV ORNL data[5], were discrepant with the new data. Disgarding the dosimetry experiment used in the ORNL experiment allowed determination of model parameters yielding yield predictions only slightly higher than the 35 MeV results. An example is included as Figure 4.

In addition, the HEDL - U.C.D. experiment clearly shows a high energy plateau (E_n > 32 MeV) resulting from reactions to the ground and first excited state of ^{8}Be. This plateau cannot be accurately predicted by the Serber model (a classical model) and therefore this structure is entered explicitly into the model. The model is used as a source term

for determining flux averaged damage parameters as explained elsewhere in this quarterly (Irradiation Effects Analysis).

VI. REFERENCES

1. H. Farrar and D. W. Kneff, Sym. of Neutron Cross Sections from 10 to 40 MeV, BNL (1977).

2. S. Grimes, et al., Sym. of Neutron Cross Sections from 10 to 40 MeV, BNL (1977).

3. C. Y. Fu and F. Perey, J. Nucl. Mat., 61, p. 153 (1976).

4. R. Serber, Phys. Rev., 72, p. 1008 (1947).

5. M. J. Saltmarsh, C. A. Ludeman, C. B. Fuller, and R. C. Styles, Cross Sections and Yields for High Energy Neutron Source Reactions, National Bureau of Standards, NBSIR 77-1279, p. 24, (1977). Also Oak Ridge report TM-56-96 (1976).

VII. FUTURE WORK

The computer code HAUSER*5 will be used to calculate helium production and reactions needed for damage cross sections for selected materials. Materials will be selected after consultation with H. Farrar of Rockwell International and D. Doran of HEDL.

The preliminary low energy measurements (E_n < 2 MeV) will be analyzed with final measurements due in April. This analysis will be combined with analysis of high energy data for a final report.

The microscopic yield model will be updated using the new neutron yield analysis. In addition, in anticipation of the use of the alternate deuteron energy at FMIT (E_d = 25 MeV), the model will be extensively compared to lower energy data.

VIII. PUBLICATIONS

A paper entitled Measurements and Calculations of Neutron Spectra from 35 MeV deuterons on Thick Lithium for the FMIT Facility (HEDL-SA-1608) by D. L. Johnson, F. M. Mann, J. Watson, J. Ullmann, and W. G. Wyckoff has been accepted for presentation at the First Topical Meeting on Fusion Reactor Materials, Miami Beach, Florida (January 1979).

A report entitled HAUSER*5, A Computer Code to Calculate Nuclear Cross Sections (HEDL-TME-78-83) is in the final editing states.

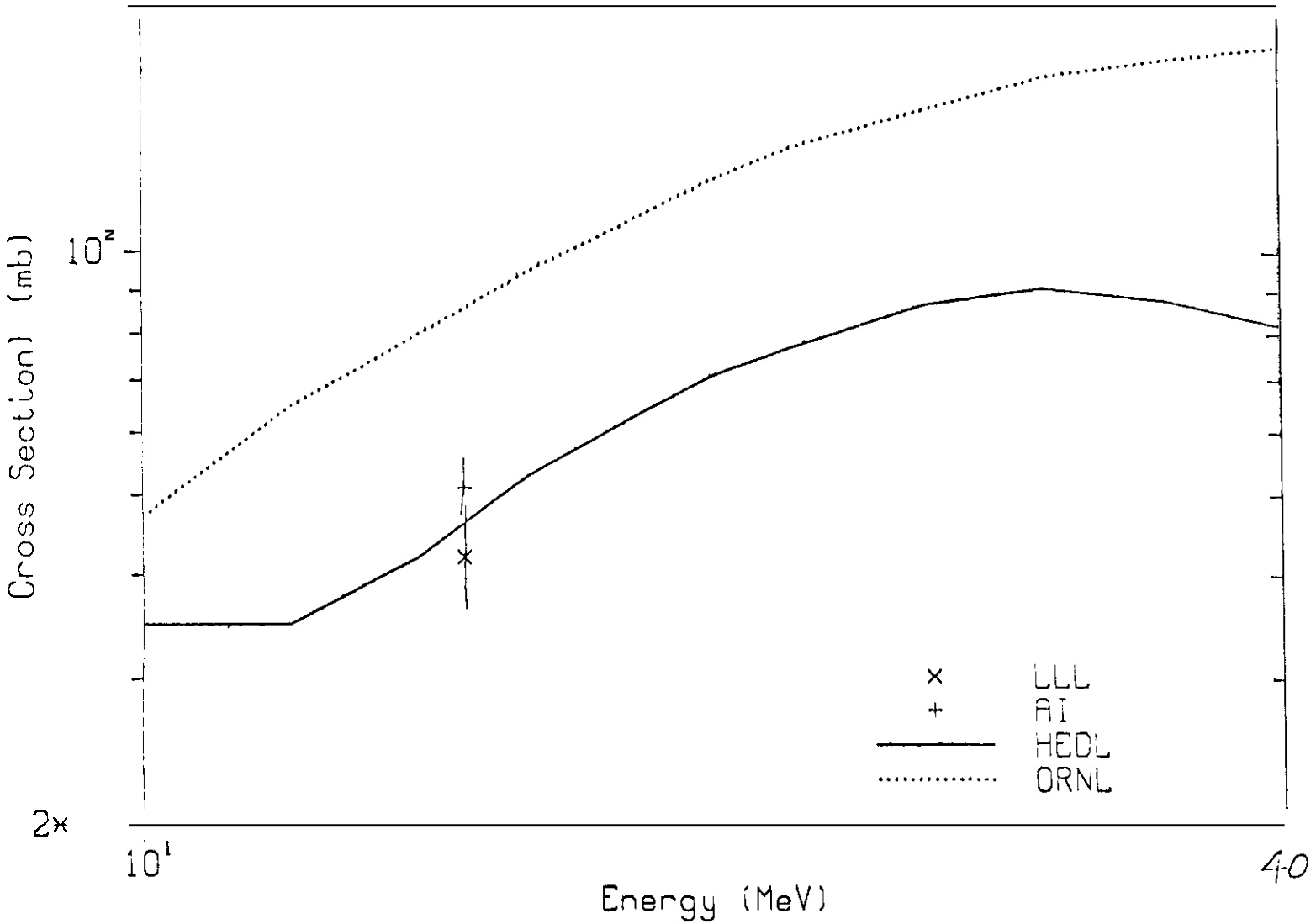

FIGURE 1. Helium Production from Neutron Bombardment of Copper.

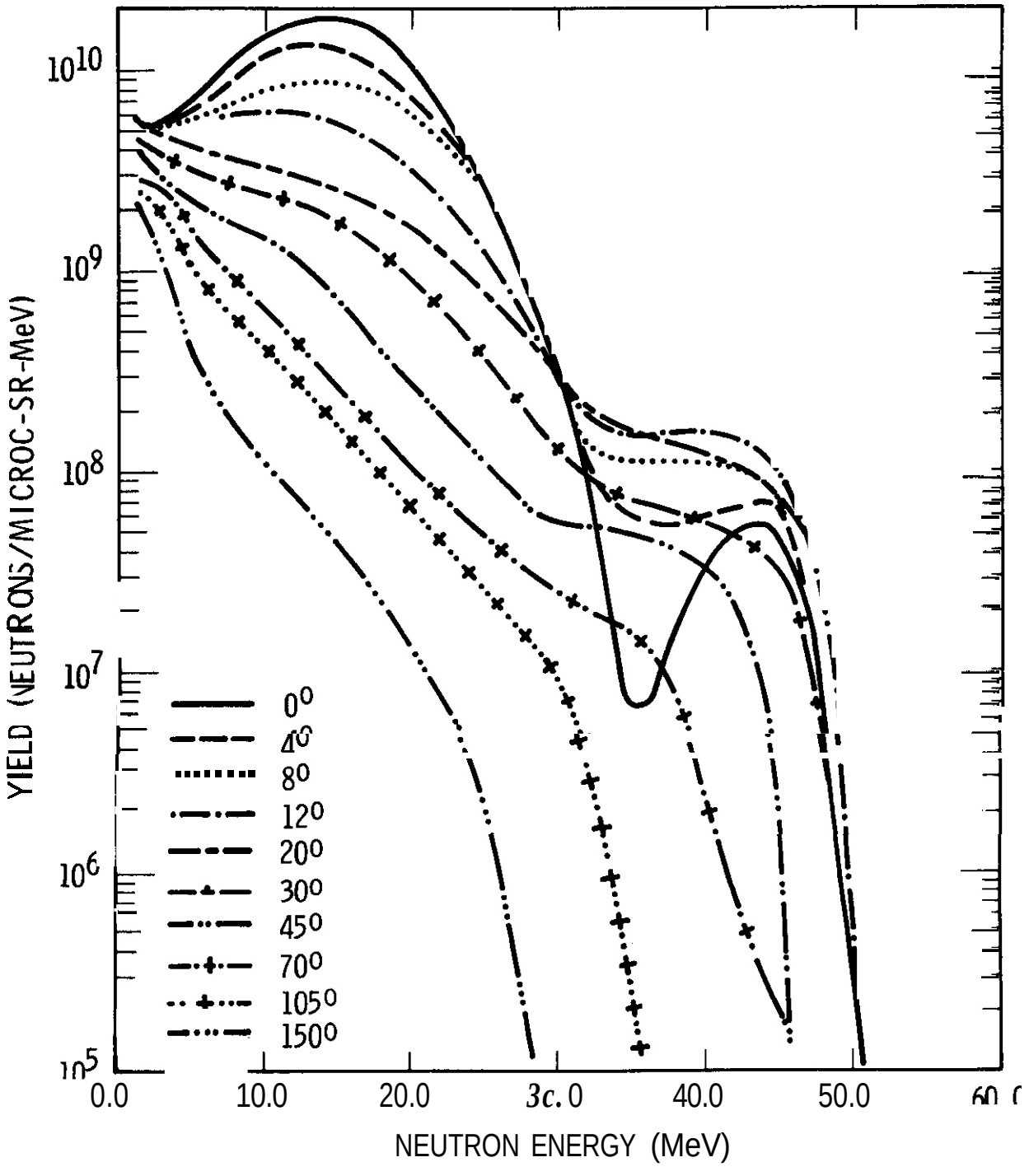

FIGURE 2. Preliminary Results for the Neutron Yield from 35 MeV Deuterons Bombarding a Thick Lithium Target.

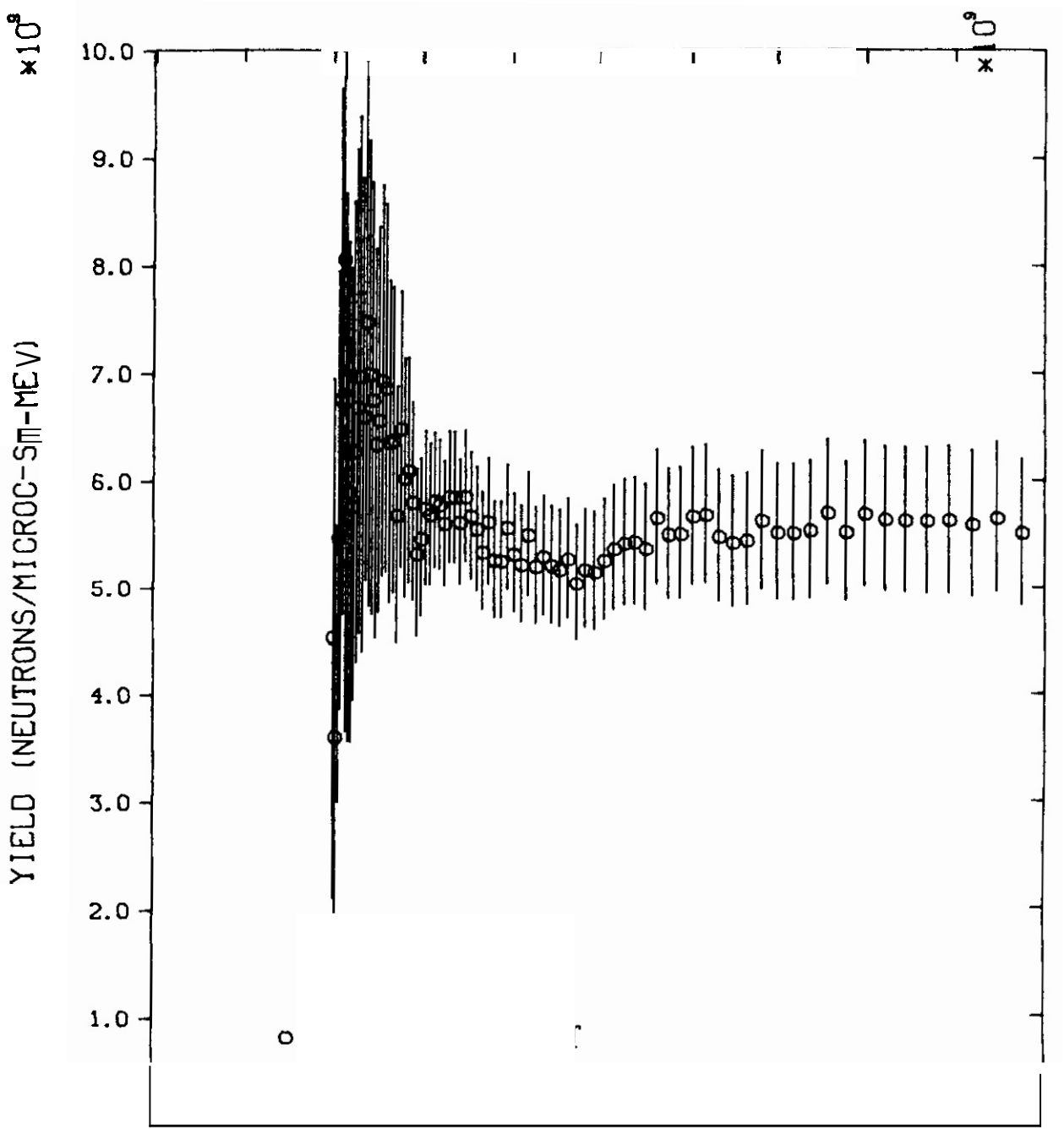

FIGURE 3. Preliminary Results for the Low Energy Neutron Yield at 12" for 35 MeV Deuterons Bombarding a Thick Lithium Target.

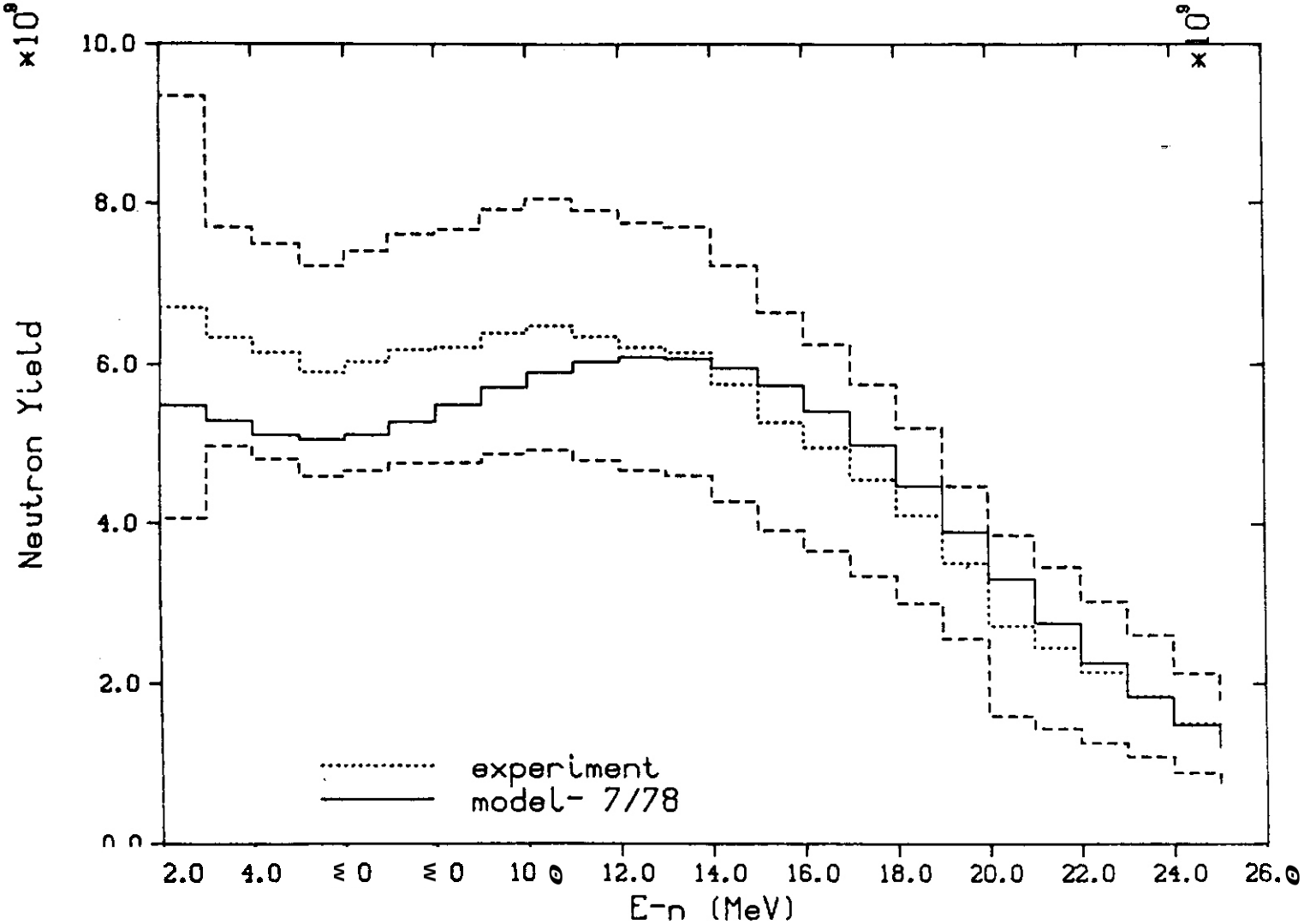

FIGURE 4. Comparison between the Preliminary Experimental Results and a Model Calculation for the Neutron Spectrum at 12° resulting from 35 MeV Deuterons Bombarding a Thick Lithium Target.

I. PROGRAM

Title: Irradiation Effects Analysis (WH011/EDA)
Principal Investigator: 0. G. Doran
Affiliation: Hanford Engineering Development Laboratory

II OBJECTIVE

The objective of this work is to predict the spatial variations of radiation damage parameters within the test volume of the Fusion Materials Irradiation Test (FMIT) facility, and the sensitivity of these parameters to cross section and spectrum uncertainties.

III. RELEVANT DAFS PROGRAM TASK/SUBTASK

SUBTASK II.A.2.4 Flux Spectrum Definition in FMIT
SUBTASK II.B.1.5 Calculation of Displacement Cross Sections

IV. SUMMARY

The major conclusion thus far is that the variation in damage rates will be dominated by changes in flux, not spectrum. Throughout the test region where the flux is greater that 10^{14} n/cm^2·s, the flux varies by a factor of about 20, while the spectral-averaged displacement and helium production cross sections for copper vary by less than factors of two and four, respectively. The corresponding helium-to-dpa ratios bracket a fusion reactor first wall value for copper (i.e., 7.7 appm He/dpa). With the Li(d,n) yields, and copper damage energy and helium production cross sections used in this study, the test volumes for which the displacement and total helium production rates are greater than those at a D-T fusion reactor first wall (with a loading of 1.0 MW/m^2) are about 139 and 208 cm^3, respectively.

V. ACCOMPLISHMENTS AND STATUS

A. Spatial Variations of Damage Parameters in FMIT and Their Implications - J. O. Schiffgens, R. L. Simons, F. M. Mann, and L. L. Carter

1. Introduction

The Fusion Materials Irradiation Test (FMIT) facility is an accelerator-based neutron source which will provide, within a reasonable test volume, a high damage rate with high energy neutrons in potential fusion reactor materials.[1] In FMIT, neutrons from Li(d,n) reactions are expected to populate spectra throughout the test volume which are broadly distributed in energy compared with fusion first wall spectra, as shown in Figure 1. Until a fusion test reactor is operating, data from FMIT, Rotating Target Neutron Source-I1 (RTNS-II), fission reactors, and charged particle irradiation facilities, together with a strong understanding of the physical processes that occur during irradiation will provide the basis for initial component design-life criteria.

The Damage Analysis and Fundamental Studies (DAFS) program has been formulated primarily to develop damage correlation models and procedures. A key step in the strategy is the verification of the methodology in FMIT. Hence, the Program Plan specifically calls for characterization of the FMIT neutron field, theinitial step of which requires analyses of the spatial variation of damage parameters in the irradiation test cell. Characterization of the expected neutron field in terms of damage parameters is also essential for the development of appropriate experimental test assemblies and for the determination of required data accuracies. Since both needs must be reflected in the design of the facility, an FMIT damage parameter sensitivity study is in progress.[2,3] This paper summarizes some of the results thus far obtained.

Spectrum and rate variations among neutron irradiation facilities are typically described in terms of primary knock-on atom (PKA) spectra, spectral-averaged cross sections for displacements per atom (dpa) and gas atoms generated from transmutation reactions (appm He or H), and the respective production rates. We have concentrated on the calculations of displacement and helium production, with emphasis on the assessment of the variations anticipated under likely operating conditions at locations of most interest for irradiation testing (i.e., where the displacement rate in stainless steel is greater than about 6 dpa/yr). Because both damage energy and helium production cross sections areavailable for copper over the energy range of interest,[4] copper was chosen as the reference material for this study. The results of some stainless steel and iron dpa calculations are also included for comparison. The damage energy[4] and helium production[5] cross sections used in this study are presented in Figure 2.

2. Results

FMIT preliminary design calls for a 0.1 amp beam of 35 MeV deuterons to strike the surface of a stream of flowing lithium 2 cm thick. The deuteron ion density is to peak at the center of the target area and be Gaussian in the vertical and horizontal directions with full-widths-at-half maximum (FWHM) of 1 cm and 3 cm, respectively. Calculations of the spatial variations of damage parameters have been made for the pristine neutron field as well as for the field perturbed by a representative irradiation test module. The materials in regions A, B, and C of the test module, as shown in Figure 3, have bulk densities which are 50, 25, and 10 percent that of stainless steel.

a. Pristine Neutron Field

Contour maps for copper displacement rate and helium production rate in the pristine neutron field are plotted in Figures 4 and 5. Note that the volumes for which the dpa and the total helium production

rates are greater than those in a D-T fusion reactor first wall with a wall loading of 1.0 MW/m^2 are about 139 and 208 cm^3, respectively. Current fusion reactor design studies envision wall loadings up to 3-5 MW/m^2. Note that the smallest contours in Figures 4 and 5, enclosing 6-11 cm^3, have displacement and helium production rates in excess of those corresponding to a first wall loading of 5 MW/m^2. The rates at which these volumes shrink with increasing damage rate is further demonstrated in Figures 6 and 7. These figures show plots of dpa rate and helium production rate versus distance (x) normal to the flowing lithium surface for various y-z coordinates. The damage rate in the x-direction changes fastest near the beam axis where the damage rate is highest.

While test volumes in FMIT are small compared with those available in fission reactors, damage rates are expected to be much higher. Figure 8 shows a bar chart comparing the neutron flux and damage rates in FMIT to those in other neutron irradiation facilities, namely HFIR, EBR-II, FTR, and RTNS-II. The data are presented as the ratio of the neutron flux, the displacement rate, and the total helium production rate in the given facility to the corresponding quantity at the first wall of a 1.0 MW/m^2 D-T fusion reactor. The FMIT source[6] and fission reactors produce displacements at an accelerated rate relative to the first wall, but, unlike FMIT, fission reactors produce transmutants at a far lower rate (except for helium production in nickel). RTNS-II, like FMIT, will produce helium-to-dpa ratios comparable to a first wall, however, low fluxes in RTNS-II prohibit producing damage rates close to or greater than those produced at a first wall. Note that with the damage energy corss sections used in this study (see Figure 2), the displacement rate in copper at the first wall is 16.7 dpa/yr while that in stainless steel is 12.5 dpa/yr.

b. Test Module Perturbed Neutron Field

Figure 3 shows the configuration and composition of a representative irradiation test module. Neutron spectra were calculated with and without this test module in the irradiation cell. Both the pristine

and test module perturbed spectra at four positions are plotted in Figure 1. As shown in Table 1, at points near the source the total flux is higher in the perturbed spectra than in the unperturbed spectra, and the reverse is true far from the source. These effects are due to neutron backscattering throughout the test assembly. The backscattering lowers the high energy flux and raises the low energy flux, as shown, with the result that the spectral-averaged damage energy and helium production cross sections are lower in the perturbed spectra. However, the test module lowers the helium-to-dpa ratio by less than ten percent throughout the volume encompassed by the module (see Table 1). Note that the copper helium-to-dpa ratios in FMIT bracket the first wall value for copper (7.7 appm He/dpa).

3. Conclusions

- FMIT test volumes for which the displacement and the total helium production rates in copper are greater than those at a D-T fusion reactor first wall, with a loading of 1.0 MW/m^2, are about 139 and 208 cm^3, respectively.

- The copper helium-to-dpa ratio in the FMIT test cell is within a factor of two of that at the fusion reactor first wall (7.7 appm He/dpa).

- While throughout the cell volume encompassed by the test module the neutron flux varies by as much as a factor of twenty, the helium-to-dpa ratio varies by less than a factor of two. Hence, damage rates are expected to be much more affected by variations in flux than variations in spectra.

VI. REFERENCES

1. J. O. Schiffgens, R. L. Simons, and F. M. Mann, Damage Analysis and Fundamental Studies Quarterly Technical Progress Report, January - March 1978, p. 43, DOE/ET-0065/1.

2. J. O. Schiffgens, R. L. Simons, F. M. Mann, and L. L. Carter, Damage Analysis and Fundamental Studies Quarterly Technical Progress Report, April - June 1978, p. 39, DOE/ET-0065/2.

3. J. O. Schiffgens, R. L. Simons, F. M. Mann, and L. L. Carter, Damage Analysis and Fundamental Studies Quarterly Technical Progress Report, July - September 1978, p. 42, DOE/ET-0065/3.

4. C. Y. Fu and F. G. Perey, J. Nucl. Mat. 61, p. 153 (1976).

5. The total helium production cross section for copper which was used here was derived as part of this study and agrees well with recent measurements, see H. Farrar IV and D. W. Kneff, Damage Analysis and Fundamental Studies Quarterly Technical Progress Report, January - March 1978, p. 58, DOE/ET-0065/1.

6. D. L. Johnson, F. M. Mann, J. W. Watson, J. Ullman, and W. G. Wyckoff, "Measurement Calculations of Neutron Spectra From 35 MeV Deuterons on TiC Lithium From FMIT Facilities," HEDL-SA-1608, January 1979.

VII. FUTURE WORK

Calculations to define the effect of data uncertainties for FMIT will continue including analyses of PKA spectral variations.

VIII. PUBLICATIONS

This information is to be presented at the First Topical Meeting on Fusion Reactor Materials, January 29-31, 1979, Miami Beach, Florida.

TABLE 1

SPECTRAL-AVERAGED CROSS ∃≤CTIONS FOR COPPER WITHIN THE FMIT TEST VOLUME;
E_d = 35 MeV, I = 0.1 amp, 1 x 3 cm Gaussian Source

	Position			Pristine					Perturbed				
	x (cm)	y (cm)	z (cm)	ϕ (10^{14}n/cm^2≤)	E_n (MeV)	$\langle\sigma_{disp}\rangle$ (10^3b)	$\langle\sigma_{He}\rangle$ (10^{-3}b)	appm He / dpa	ϕ (10^{14}n/cm^2≤)	E_n (MeV)	$\langle\sigma_{disp}\rangle$ (10^3b)	$\langle\sigma_{He}\rangle$ (10^{-3}b)	appm He / dpa
1	0.0	0.0	0.0	22.3	9.17	2.75	23.0	8.4	24.0	8.48	2.59	20.9	8.0
2	5.0	0.0	0.0	3.54	12.60	3.45	36.4	10.6	2.88	11.0	3.09	31.1	10.1
3	10.0	0.0	0.0	1.53	13.12	3.56	38.7	10.9	.969	11.5	3.18	33.2	10.4
4	15.0	0.0	0.0	.837	13.31	3.61	39.6	11.0	.419	12.1	3.32	35.9	10.8
5	0.0	2.0	0.0	9.49	8.45	2.60	20.3	7.8	10.4	7.71	2.4∃	18.1	7.5
6	5.0	2.0	0.0	2.13	11.96	3.31	10.2	10.2	1.83	10.1	2.8∃	27.6	9.5
7	10.0	2.0	0.0	1.07	12.78	3.49	37.1	10.6	.721	10.9	3.0≥	30.9	10.1
m	0.0	4.5	0.0	1.o≥	5.9	2.11	11.3	5.3	1.9	5.z8	1.93	9.63	5.0
m	z.0	4.5	0.0	.∃∃6	7.7	2.40	16.6	6.9	73	6.z1	2.09	13.2	6.3
10	0.0	0.0	2.0	3.2∃	6.21	2.15	11.9	∃.5	3.72	5.56	1.98	10.3	5.2
11	2.0	0.0	2.0	2.3∃	9.14	2.72	22.6	∃.3	2.64	7.81	2.42	18.6	7.7
12	5.0	0.0	2.0	1.4∃	11.04	3.12	30.1	∃.6	1.48	9.24	2.72	24.3	9.0
13	10.0	0.0	1.5	1.0∃	12.74	3.47	36.8	1o.6	.780	10.8	3.03	30.4	10.0
14	0.0	z.0	2.0	2.1≥	∃.∃6	2.08	10.7	m.1	2.e7	m.1∃	1.91	9.1z	4.8
15	2.0	z.0	2.0	1.6≥	∃.e4	2.58	20.0	r-.8	1.∃9	r-.0e	2.27	16.1	7.1
16	5.0	z.0	2.0	1.1o	1o ≥	3.01	28.0	∃.3	1.14	∃.6≥	2.59	22.2	8.6
17	0.0	0.0	3.0	1.5≥	5 ≤6	z.0∃	∃∃∃	4∃	1 ∃1	4∃∃	1 ∃≥	e 4∃	4 ≥

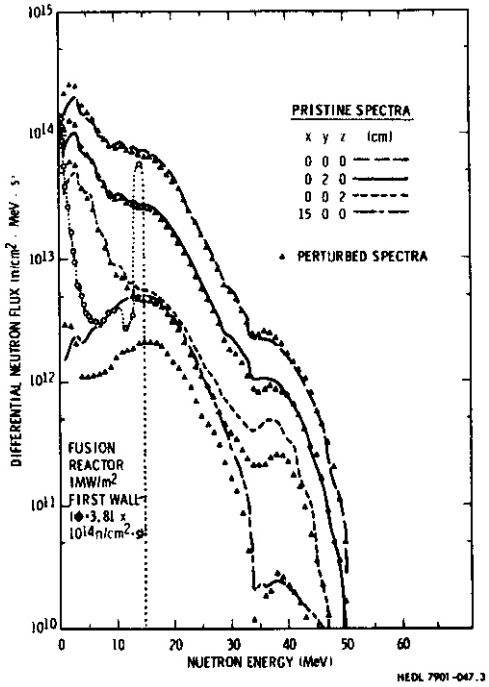

FIGURE 1. Calculated Neutron Spectra at Four Positions Within the FMIT Irradiation Cell (for E_d = 35 MeV and I = 0.1 amp) Compared With a D-T Fusion Reactor First Wall Spectrum. The total flux at each position is shown in Table 1.

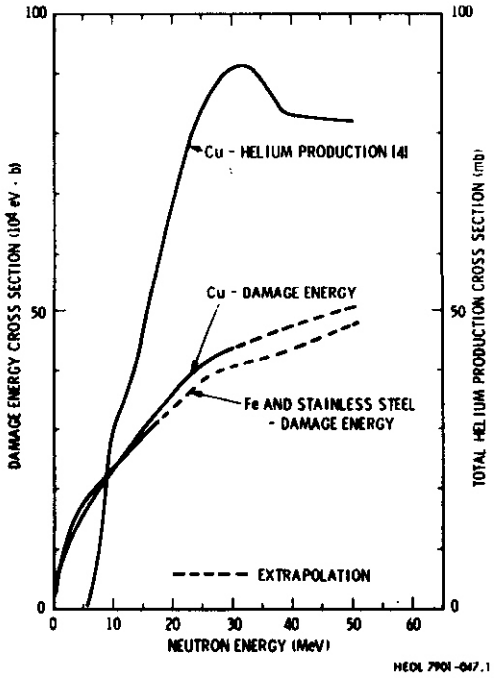

FIGURE 2. Damage Energy and Helium Production Cross Sections Versus Neutron Spectra.

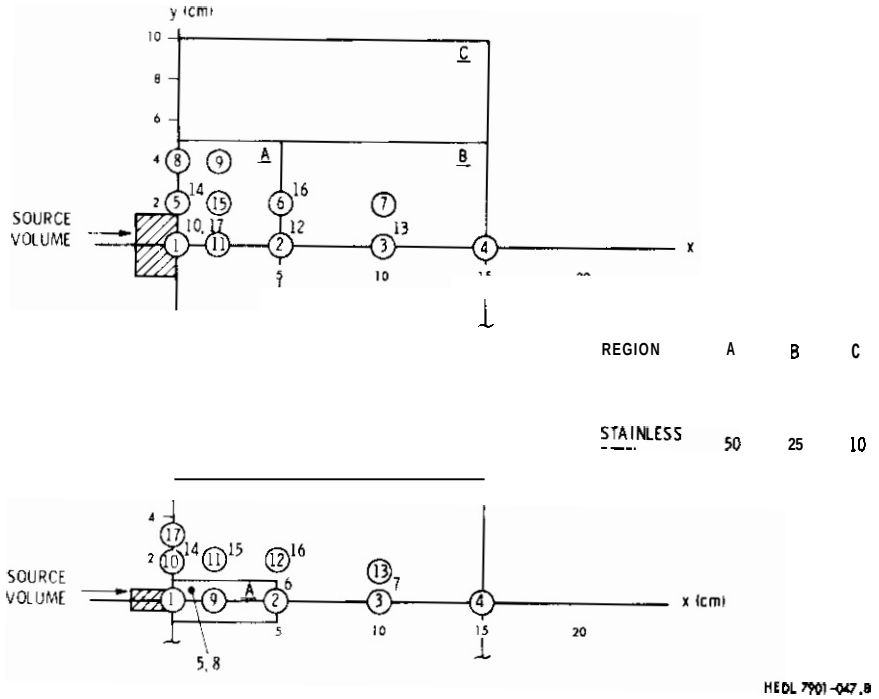

FIGURE 3. Configuration of a Representative Irradiation Test Module and Positions at Which Neutron Spectra Were Calculated.

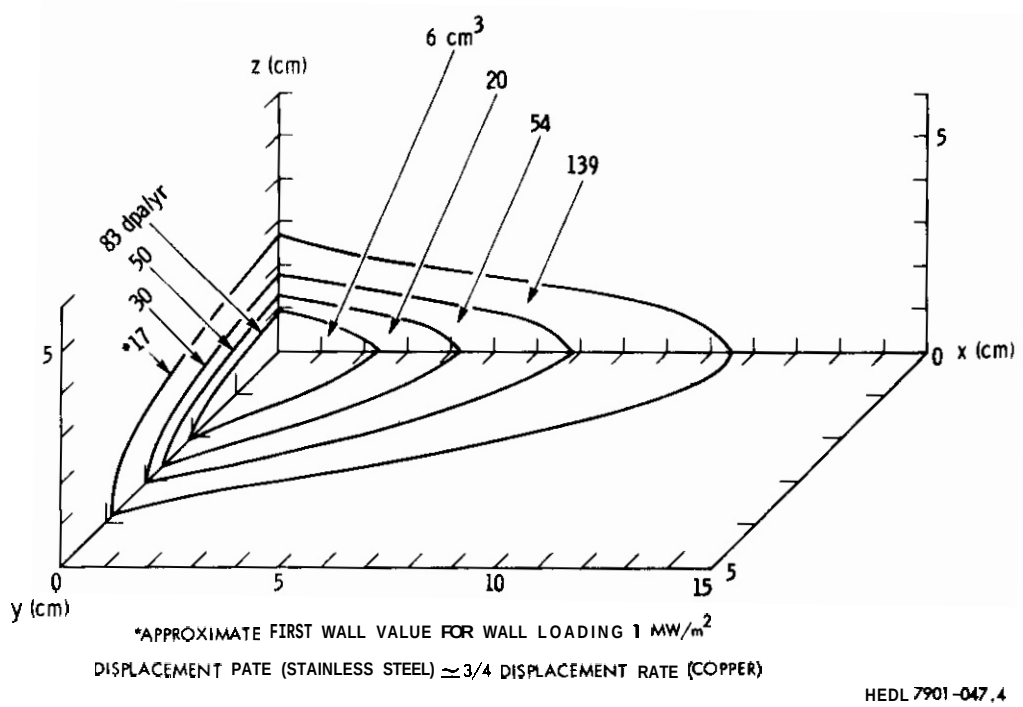

FIGURE 4. First Quadrant Displacement Rate Contour Naps for a 1 x 3 cm FWHM Gaussian Source Distribution (E_d = 35 MeV and I = 0.1 amp). Total volumes within the contours are shown.

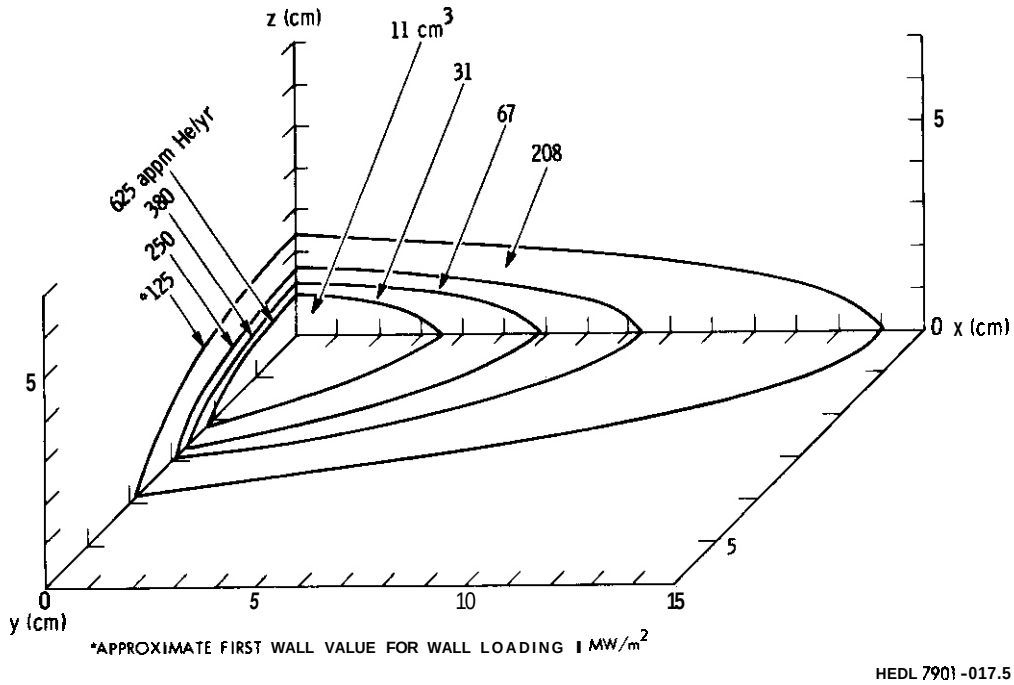

FIGURE **5.** First Quadrant Helium Production Rate Contour Maps for a 1 x 3 cm FWHM Gaussian Source Distribution (E_d = 35 MeV and I = 0.1 amp). Total volumes within the contours are shown.

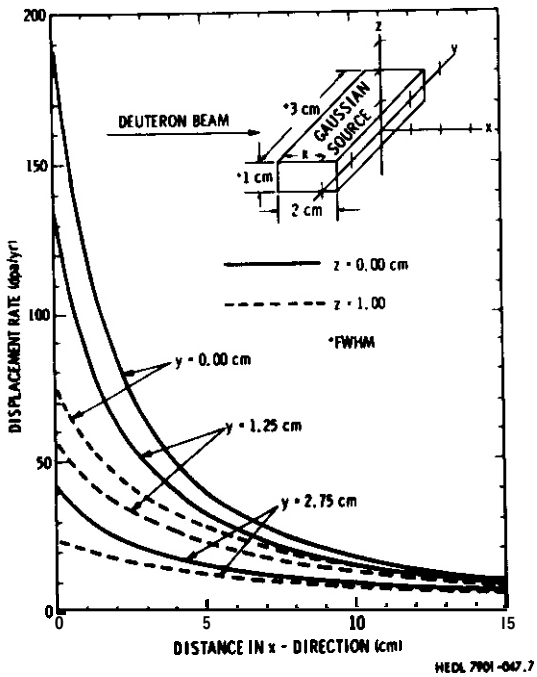

FIGURE **6.** Displacement Rate Versus Distance Normal to the Source Surface.

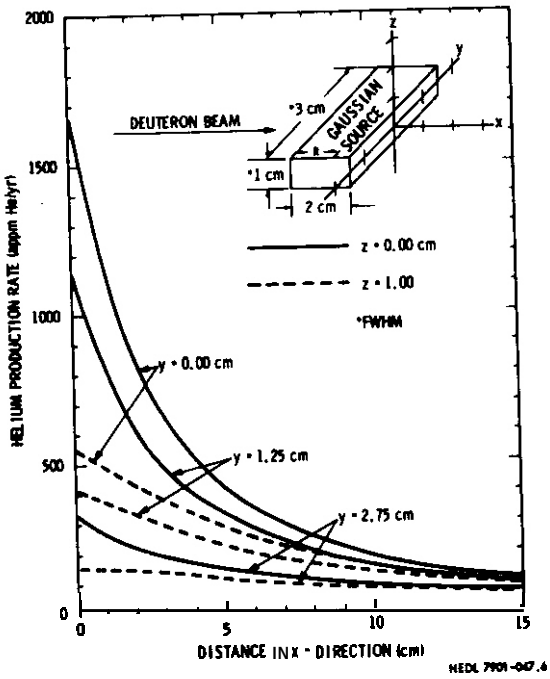

FIGURE 7. Helium Production Rate Versus Distance Normal to the Source Surface.

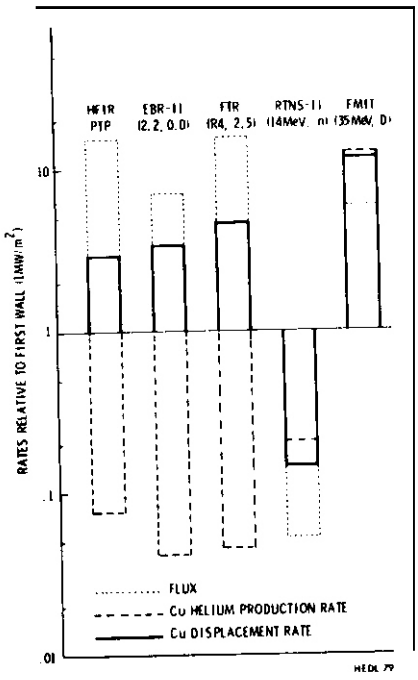

FIGURE 8. Ratios of Flux and Damage Rates in Various Neutron Irradiation Facilities to Values at a 1.0 MW/m^2 D-T Fusion Reactor First Wall

I. PROGRAM

Title: Dosimetry and Damage Analysis
Principal Investigator: L. R. Greenwood
Affiliation: Argonne National Laboratory

II. OBJECTIVE

To determine damage parameters and their uncertainties in various neutron fields.

III. RELEVANT OAFS PROGRAM PLAN TASK/SUBTASK

SUBTASK II.A.3.1 Evaluate damage parameter sensitivity to flux-spectra uncertainities

Task II.B.I Calculation of defect production cross sections

IV. SUMMARY

The ANL damage cross section files have been extended to 50 MeV for Cr, Fe, Ni, Cu, and Nb using recent cross section calculations from ORNL. Routine calculations with error analysis are illustrated in a Be(d,n) field. Results are compared to 14 MeV and ^{235}U fission cross sections.

V. ACCOMPLISHMENTS AND STATUS

A. Calculation of Damage Cross Sections for Cr, Fe, Ni, Cu, and Nb to 50 MeV -- L. R. Greenwood

Neutron spectra generated at Be or Li(d,n) sources such as

the U.C. Davis cyclotron or FMIT extend to 40-50 MeV. Damage calculations at such facilities are hampered by a lack of neutron cross section data above 20 MeV, the energy at which the ENDF/B-IV files end. Recently the required cross sections have been calculated to 32 MeV for Cu and Nb (Ref. 1) and to 60 MeV for a variety of elements (Ref. 2). We have used these calculated cross sections for the elastic, inelastic, (n, 2n), (n, p+), and (n,α+) channels and extrapolated them where necessary to 50 MeV. Damage cross sections and recoil distributions were then calculated using the DISCS[3] code. Elastic angular distributions were assumed to remain constant above 20 MeV and all charged particle reactions were lumped into the (n,p) or (n,α) channels. The latter approximation is not too important since the elastic, inelastic, and (n, 2n) cross sections contribute most of the damage. A Lindhard cutoff of 40 eV was used in all cases.

Figure 1 shows the calculated damage cross sections. for Cr, Fe, and Ni. The results for Cu and Nb are very similar to those published in Ref. 1. Table I compares spectra-averaged damage rates for a Be(d,n) source (0^o, E_d = 40 MeV), a 14 MeV source, and a ^{235}U fission spectrum. As can be seen, the Be(d,n) results are very similar to those at 14 MeV This is not surprising since the average Be(d,n) neutron energy is close to 14 MeV.

Damage calculations for an actual irradiation for PNL at U.C. Davis (Be(d,n), E_d = 40 MeV) are listed in Table 11. The errors are derived from a Monte Carlo analysis of the dosimetry, including uncertainties in the foil activities, nuclear cross sections, and input spectra. The errors do not include uncertainties in the damage cross sections. Such errors are unknown, but may not be too large in the present example since about 90% of the damage is generated between E_n = 1 - 30 MeV. For iron, only 1% of the damage is generated below 1 MeV; 9% below 5 MeV; 10% above 30 MeV; and only 4% above 35 MeV. Integral errors in damage rates are thus low (<10%) since the flux-

spectrum can be determined quite accurately (~10-30%) in the energy region where most of the damage is generated.

VI. REFERENCES

1. C. Y. Fu and F. G. Perey, J. Nucl. Mat. 61, 153 (1976).

2. R. G. Alsmiller and J. Barish, ORNL/TM-6486 (1978)

3. G. R. Odette and D. R. Dorian, Nucl. Tech. 29, 346 (1976).

4. J. A. Grundl and C. M. Eisenhauer, Conf. on Nucl. Cross Sections and Tech., Washington, NBS 425, Vol. I 250 (1975)

VII. FUTURE WORK

We plan to add several new elements to our extended damage file including Al and Au (Ref. 1) and C, O, and Si (Ref. 2). Other elements will be added when cross sections become available.

VIII. PUBLICATIONS

None

TABLE I: Spectral Averaged Damage Cross Sections, keV-b

Element	Fission[a]	14.25 MeV	Be(d,n), 40 MeV[b]
Al	98.3	173	—
Ti	95.7	269	—
Cr	91.6	272	240
Fe	80.3	272	242
Ni	82.2	299	286
cu	81.3	268	259
Nb	79.5	260	259
316SS	83.0	274	251
Au	50.5	219	—

[a] ^{235}U Maxwellian from Ref. 4; $N(E) = 0.7501 \sqrt{E}\ EXP(-1.5\ E/1.97)$

[b] Zero degree, time-of-flight spectrum

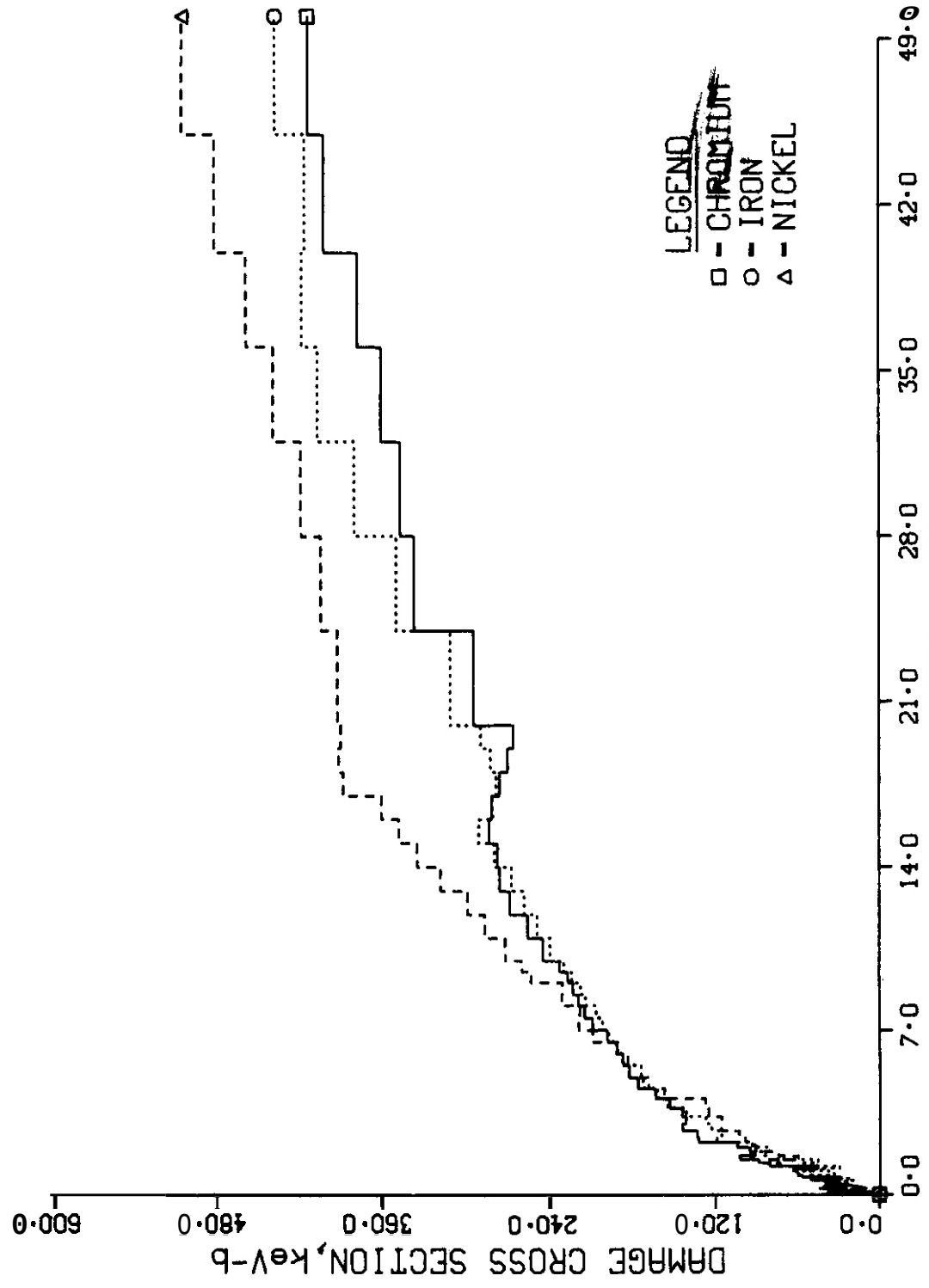

FIGURE 1. Displacement Damage Cross Sections are Shown for Cr, Fe, and Ni. Damage Energy Cross Sections are a Factor of Ten Higher if a Lindhard Cut Off of 40 eV is Assumed.

TABLE 11: Integral fluence and calculated damage rates for Be(d,n), E_d = 40 MeV. Errors due to dosimetry only. Nuclear cross sections from Ref. 1 and 2.

	Energy Limits, MeV				
Fluence	Total	>4	>10	>20	>30
10^{17} n/cm^2	2.95 ± .16	2.29 ± .12	1.58 ± .07	0.53 ± .06	0.17 ± .04

Spectral Averaged Parameters	Ni	Cu	Nb	316SS
$\langle\bar{\sigma}_D\rangle$, keV-b	257 ± 10	233 ± 9	230 ± 8	225 ± 11
$\langle T_D, >$kev	82f 4	72 ± 4	54 ± 3	78 ± 5
$\langle\bar{\sigma}_{He}\rangle$, mb	112 c 4	39 ± 2	7.9 ± 0.4	38 ± 3

	PKA Distributions, %			
Energy, keV				
0.04 - 1	5.8 ± 1.4	4.6 ± 0.9	6.0 ± 1.2	3.8 ± 0.8
1 - 10	19.2 ± 3.5	19.8 ± 3.0	29.8 ± 5.5	17.7 ± 2.7
10 - 40	24.9 ± 2.2	25.4 ± 2.3	23.8 ± 2.5	24.6 ± 2.2
40 - 100	14.2 ± 0.7	15.1 ± 1.1	13.3 ± 1.2	15.2 ± 1.0
100 - 500	25.1 ± 1.3	28.5 ± 1.4	24.8 ± 1.0	29.4 ± 1.4
500 - 1000	8.9 ± 0.5	5.8 ± 0.4	2.2 ± 0.3	8.1 ± 0.6
>1000	1.9 ± 0.2	0.8 ± 0.2	0.1 ± 0.03	1.2 ± 0.2

CHAPTER 4

SUBTASK B: DAMAGE PRODUCTION

I. PROGRAM

Title: Radiation Damage Analysis and Computer Simulation
Principal Investigator: Don M. Parkin
Affiliation: Los Alamos Scientific Laboratory of the University of California

II. OBJECTIVE

The objective of this work is to develop displacement functions for polyatomic materials.

III. RELEVANT DAFS PROGRAM PLAN TASK/SUBTASK

SUBTASK II.B.2.3 Cascade Production Methodology
II.B.4.1 Interface With Other Designs and Other Tasks
II.B.4.2 Develop Theory of Spectral and Rate Effects

IV. SUMMARY

The computer code DISPLC which calculates displacement functions in monatomic and polyatomic materials and the computer code ALLØY which calculates damage energies in monatomic and polyatomic materials have been used to calculate universal displacement functions for monatomic materials. The results show the role of threshold effects and that the number of displacements is essentially proportional to damage energy at energies above a few keV.

. ACCOMPLISHMENTS AND STATUS

A. Displacement Functions for Monatomic Materials - D. M. Parkin (LASL) and C. A. Coulter (University of Alabama)

1. Results

Analytical functions that represent the results of calculations of displacement functions for monatomic materials have been obtained. Two displacement functions, the total displacement function, $n(E)$, defined to be the average number of atoms displaced from their sites in a displacement cascade including the PKA, and the net displacement function, $g(E)$, defined to be the average number of atoms displaced from their sites and not recaptured in subsequent replacement collisions in a displacement cascade including the PKA, were calculated. The results are closely approximated by

$$\begin{matrix} n(E) \\ g(E) \end{matrix} = 1 + \chi \left[1 - (E_T/E)^{N_1}\right]^{N_2} \nu(E)/2E_d \qquad (1)$$

for $E \geq E_T$. The function $\nu(E)$ is the damage energy and is described below. The parameters N_1, N_2, χ, and E_T are equal to 0.88, 1.5, 1.01, and E_D for $n(E)$ and 1.0, 1.39, 0.79, and $2E_D$ for $g(E)$.

The damage energy used in eq. 1 is that obtained using the ALLØY code. In both the **DISPLC** and ALLØY codes, a numerical **fit** to the tabular values of the Lindhard et al.[1] function, $f(\xi)$, is used which for small ξ gives $f(\xi) \propto \xi^{0.35}$. The calculated values of damage energy by Lindhard et al.[2] hence, the damage energy formula obtained by Robinson[3] were obtained using the more approximate form $f(\xi) \propto \xi^{1/3}$. The ALLØY results are about 6% lower than the Lindhard et al. calculations in agreement with their statement that the $\xi^{1/3}$ approximation over-estimates $\nu(E)$ by "several percent." Using the method of Robinson and Lindhard et al. we obtain

$$\bar{g}(\varepsilon) = \bar{c}_1\varepsilon^{0.15} + \bar{c}_2\varepsilon^{0.75} + \bar{c}_3\varepsilon \qquad (2)$$

where Robinson obtained

$$g_R(\varepsilon) = 3.4008\varepsilon^{1/6} + 0.40244\varepsilon^{0.75} + \varepsilon. \quad (3)$$

The best-fit coefficients $\bar{c}_i$ were obtained over the scaled-energy range $0 \leq \varepsilon \leq 5000$ for values of $k_L = 0.12,\ 0.15,\ 0.18$. Since for most materials $k_L \approx 0.15$, we have elected to use these results. Thus,

$$\bar{g}(\varepsilon) = 3.3967\varepsilon^{0.15} + 0.9863\varepsilon^{0.75} + 0.8490\varepsilon. \quad (4)$$

Eq. 4 approximates the damage energy function

$$\nu(E) = \frac{E}{1 + k_L g(\varepsilon)} \quad (5)$$

to 5% or better for $0.12 \leq k_L \leq 0.18$ and $0 \leq \varepsilon \leq 5000$. In a practical sense, there is no advantage in using eq. 4 rather than eq. 3 other than that eq. 4 is consistent with eq. 1. In eq. 1 the term $[1 - (E_T/E)^{N_1}]^{N_2}$ represents the deviation from proportionally of $n(E)$ and $g(E)$ with $\nu(E)$. Values of $[1 - (E_T/E)^{N_1}]^{N_2}$ for $E_d = 25$ eV are shown in the table. It can be seen that for energies above a few keV $[1 - (E_T/E)^{N_1}]^{N_2} \approx 1$ and $n(E)$ and $g(E)$ are proportional to $\nu(E)$. Further, since $\chi = 0.79$ for $g(E)$ and eqs. 3 and 4 give similar results, above a few keV, the results for $g(E)$ are essentially the same as those obtained using

$$N = \frac{0.8}{2E_D}\,\nu(E). \quad (6)$$

VI. REFERENCES

1. J. Lindhard, V. Nielson and M. Scharff, Mat. -fys. Medd. 36, No. 10 (1968).

2. J. Lindhard, M. Scharff and H. E. Schiøtt, Mat. -fys. Medd. 33, No. 14 (1963).

3. M. T. Robinson, Proceedings of the B.N.E.S. Nuclear Fusion Reactors Conference at Culham Laboratory, p. 364 (1969).

TABLE 1

VALUES OF $[1 - (E_T/E)^{N_1 N_2}]$ FOR n(E) and g(E) ASSUMING E_d = 25 eV

E(eV)	n(E)	g(E)
5×10^1	0.309	0.0
1×10^2	0.592	0.382
2×10^2	0.769	0.670
4×10^2	0.872	0.831
1 x 103	0.942	0.931
3 x 103	0.978	0.977
1 x 104	0.992	0.993

VII. FUTURE WORK

Future work will focus on obtaining analytical fits for n(E) and g(E) in polyatomic materials.

VIII. PUBLICATIONS

None reported.

I. PROGRAM

Title: Damage Analysis
Principal Investigator: M T. Robinson
Affiliation: Oak Ridge National Laboratory

II. OBJECTIVE

The objective of this work is to construct both atomistic and continuum (transport theory) models of collision cascade development in solids and to apply these models to radiation damage production, to sputtering, and to plasma particle backscattering problems.

III. RELEVANT DAFS AND PMI TASK/SUBTASK

DAFS SUBTASK II.B.2.3: Cascade Production Methodology

PMI SUBTASK III.B.1.3: Developnent of Theoretical Model Descriptions of Reflection and Backscattering

PMI SUBTASK III.C.1.6: Developnent of Theoretical Models for Physical and Physichemical Sputtering

IV. SUMMARY

Application of nunerical transport theory to particle range distributions in solids has been comnenced, on the example of 100 keV ^{196}Au recoils in Au. Comparisons of the BCA code MARLOWE and the dynamical code COMENT have been made with respect to their treatments of linear collision sequences.

V. ACCOMPLISHMENTS AND STATUS

A. Range Calculations Using Multigroup Transport Methods --

T. J. Hoffman and M. T. Robinson (ORNL) and H. L. Dodds, Jr. (University of Tennessee, Knoxville)

The application of the discrete ordinates transport theory code ANISN to calculations of light-ion sputtering yields was discussed in a previous report.[1] We have now applied similar methods to the calculation of particle range distributions. These techniques are illustrated by analysis of ^{196}Au atoms recoiling from (n,2n) reactions in gold. The results of these calculations agree well with range calculations performed with the atomistic code MARLOWE. Although some detail of the atomistic model is lost in the multigroup transport calculations, the improved computational speed may prove useful in the solution of fusion material design problems.

The transport calculations used the well-known WSS approximation to describe the atomic scattering.[2] Multigroup cross sections were constructed as before[1] and used in the codes ANISN (one-dimensional discrete ordinates[3]) and MORSE (three-dimensional Monte Carlo[4]) to compute range distributions. The MARLOWE calculations were based on Molière potential scattering. Table 1 shows comparisons among the three codes of several calculated range parameters. While the differences are likely to be results of the slightly different scattering models employed, current work is directed to exploring the situation in more detail, to determine if this is indeed the case, or whether more fundamental modelling differences are responsible.

Table 1. Comparison of Range Parameters for 100 keV ^{196}Au Slowing Down in Gold

Parameter	ANISN	MORSE[a]	MARLOWE[a]
$\langle x^0 \rangle$	1.000	0.991±0.008	1.0
$\langle x^1 \rangle$, Å	128.4	125.5±2.0	121.3t.7
$\langle x^2 \rangle$, Å^2	23407.	22676.±573.	19350.
Radial Spread, Å	b	86.80k1.84	67.53k0.42
Vector Range, Å	b	161.0±2.7	144.1k0.7
cpu time (IBM 360/91),[c] min.	4.8	9.8 d	108.0[d]

[a] Based on 10,000 histories.

[b] Not amenable to one-dimensional analysis.

[c] The ANISN and MORSE computation times do' not incude the 17.4 min. required on the IBM 360/91 to generate the multigroup cross sections.

[d] Run on the IBM 360/195; a conversion factor of 2.0 was used.

B. Study of the Low Energy Responses of the BCA code MARLOWE

M. T. Robinson (ORNL)

An efficient methodology for displacement cascade simulation requires the use of codes based on the binary collision approximation (BCA) at high energies, since dynamical methods require too great an investment in computational resources. At sufficiently low energies, the BCA is no longer an adequate representation of the motion of the recoiling atoms, mainly because individual collisions become difficult to identify. In order to determine a reasonable (lower) energy 1imit for BCA calculations, comparisons of the BCA code MARLOWE[5] with the dynamical code COMENT[6] and the "quasidynamical" code ADDES[7] are being made. Some contributions to the BCA part of this comparison are described here.

A potentially important parameter in MARLOWE is p_m, the maximum impact parameter allowed in any collision. This quantity establishes the effective sizes of the atoms in the crystal. If fcc crystals are described by first and second neighbors only, $(1/6)^{1/2} < p_m/a < (5/8)^{1/2}$ is required to obtain correct generation of crystal by the program, where a is the cubic unit cell edge. As a first study of this parameter, a series of recoil range calculations was made, for Cu primaries slowing down in Cu, using 1000 primaries in each group. No simple dependence of the range on p_m is observed, the differences being attributed to statistical effects alone. Thus, for range calculations, which are

Table 2. Effects of the Maximum Impact Parameter on Primary Vector Ranges Calculated with MARLOWE (Version 11). Cu atoms slowing down to 4.5 eV in Cu.

Initial Primary	Mean Primary Vector Range (units of a)			
	p_m/a = 0.41	0.50	0.62	0.71
0.01	0.420r.003	.406±.002	.408±.002	0.414t.002
0.1	1.299r.010	1.274t.010	1.292r.010	1.301±.010
1	3.614r.045	3.634r.046	3.642r.043	3.667r.044
10	15.77t.40	15.77t.36	16.09t.42	15.81t.36
100	94.46t2.53	95.17±2.17	100.40r3.36	101.82r3.09

determined mainly by energies near the initial primary energy, the results are insensitive to the impact parameter cut-off. This reflects the very small amount of energy lost in the large impact parameter encounters.

In an earlier report,[7] Schiffgens and Schwartz reported a series of comparisons of 1inear collision sequences (LCS's) evaluated by COMENT and ADDES. These same LCS's have also been examined with MARLOWE, using the same Molière potential and screening length (a_{12} = 0.0738 A). Each atom was bound to its lattice site by an amount E_b. Other work has shown that perfectly focussed <011> LCS's in

this potential require $E_b \approx 0.5$ eV for MARLOWE to give agreement with dynamical results. Preliminary studies of LCS's with Version 11 of MARLOWE suggested several modifications of the program, particularly with respect to improving the procedure for avoiding unphysical repetitive cycles of collisions with small sets of targets. Table 3 shows the lengths of the LCS's evaluated by MARLOWE, using the improved version 11.1, for various choices of the parameters p_m and E_b. In general, MARLOWE <011> sequences are shorter than those in COMENT, although it is clear that LCS's close to the axis could be matched to COMENT for some choice of the parameters. The best selection for this purpose could be made only on the basis of more extensive calculations with both codes. In contrast to <011> LCS behavior, the <001> and <111> sequences generated by MARLOWE are longer than those in COMENT, and these lengths are less sensitive to the choice of parameters. Both aspects accord with expectations based on the approximations used in MARLOWE.

Table 3. Comparison of Linear Sequences in Cu Evaluated by the Programs COMENT and MARLOWE (Version 11.1). Molière potential with $a_{12} = 0.0738$ Å. MARLOWE sequences terminated at $E_c = 4.5$ eV.

LCS axis		A [101]	B [101]	C [101]	D [001]	E [001]	F [111]
Initial angle from axis, deg.		1.2	3.6	6.0	1.0	2.0	2.0
Initial energy, eV		25	38	50	40	30	150
Replacements per sequence found using:							
COMENT		34	13	7	6	4	5
MARLOWE							
E_b, eV	p_m/a						
0.50	0.50	23	10	6	11	6	8
0.50	0.62	20	12	6	11	8	8
0.50	0.71	20	10	6	11	8	8
0.35	0.71	24	10	6	12	8	8
0.00	0.71	51	10	6	13	9	8

VI. REFERENCES

1. T. J. Hoffmann, et al., Damage Analysis and Fundamental Studies Quarterly Progress Report, January-March 1978, pp. 82-3.
2. K. B. Winterbon, P. Sigmund, and J. B. Sanders, Kgl. Danske Videnskab Selskab, Mat.-fys. Medd. 37, No. 14 (1970).
3. W. W. Engle, Jr., A User's Manual for ANISN, Report K-1693 (1967).
4. M. B. Emmett, The MORSE Monte Carlo Radiation Transport Code System, Report ORNL-4972 (1975).
5. I. M. Torrens and M. T. Robinson, Phys. Rev. B 9, 5008 (1974).
6. J. O. Schiffgens and R. O. Bourquin, J. Nucl. Mater. 69/70, 790 (1978).
7. J. O. Schiffgens and O. M. Schwartz, Damage Analysis and Fundamental Studies Quarterly Progress Report, January-March 1978, DOE/ET-0065/1, pp. 88-111.

VII. FUTURE WORK

Further study of the numerical transport theory technique will be directed to determining the extent to which differences between transport theory and atomistic calculations are caused by differences in the scattering laws and the extent to which they are caused by more fundamental model differences. Comparisons of MARLOWE and COMENT will be continued.

VIII. PUBLICATIONS

T. J. Hoffman, H. L. Dodds, Jr. M. T. Robinson, and D. K. Holmes, "Sputtering calculations with the Discrete-Ordinates Method," Nucl. Sci. Eng. 68, 204 (1978).

M. Hou and M. T. Robinson, "Mechanisms for the Reflection of Light Atoms from Crystal Surfaces at Kilovolt Energies," Appl. Phys. 17, 295 (1978).

M. Hou and M. T. Robinson, "The Conditions for Total Reflection of Low-Energy Atoms from Crystal Surfaces," Appl. Phys. 17, 371 (1978).

O. S. Oen and M. T. Robinson, "Computer Simulation of the Reflection of Hydrogen and Tribium from Solid Surface," Proc. Symp. Atomic Surf. Phys. '78, edited by W. Lindner, F. Howorka, and F. Egger (Inst. Atomphysik. Innsbruck, 1978), p. 39.

I. PROGRAM

Title: Irradiation Effects Analysis (WHO11/EDA)
Principal Investigator: D. G. Doran
Affiliation: Hanford Engineering Development Laboratory

II OBJECTIVE

The objective of this work is to develop computer models for the simulation of high energy cascades which will be used to generate defect production functions for correlation analyses of radiation effects.

111. RELEVANT DAFS PROGRAM TASK/SUBTASK

SUBTASK II.B.2.3 Cascade Production Methodology

IV. SUMMARY

A modification of the quasi-dynamical computer code ADDES has been developed to allow for the simulation of defect production in high energy cascades. In the first of a two-stage modeling process, the cascade is allowed to develop until no atom has more than a relatively high cut-off energy. As atoms fall below the cut-off, they are tagged and removed from consideration during the remainder of the development. The second stage is the evaluation of defect production by energetic atoms tagged in the first stage using a defect yield function determined from dynamical simulations of low energy events. This code is used to simulate defect production in 10 keV cascades in several directions in copper, and the results are compared with those of the binary collision code MARLOWE. Good agreement is obtained when an effective recombination radius of 2.2 lattice units is assumed for each.

V. ACCOMPLISHMENTS AND STATUS

A. The Application of Dynamical Computer Models to High Energy Cascades - H. L. Heinisch, J. O. Schiffgens (HEDL), and D. M. Schwartz (California State University at Northridge)

1. Introduction

Computer simulations are an important aspect of the investigation of the effects of radiation damage in fusion reactor materials. Simulations can provide damage parameters for correlating and extrapolating experimental data, and phenomenology for guiding and analyzing experiments, as well as a basis for understanding the fundamental aspects of radiation damage. It is important to be able to model the damage produced by the high energy (up to MeV range) primary knock-on atoms (PKAs) generated in first wall materials by the substantial component of high energy neutrons.

High energy is operationally defined here as greater than 1 keV, which is about the upper limit (in copper) for the usual dynamical models of cascades. Most of the simulations reported on here were 10 keV PKAs. It is probably not necessary to be able to model in detail cascades of energy higher than about 100 keV in copper; since above perhaps 30 keV, PKAs may begin to produce sub-cascades. Each of the sub-cascades can thus be modeled separately once the energies of the cascade producing secondary knock-on atoms is determined.

As the energy of a high energy PKA is dissipated during the formation of the cascade, the initial, high energy collisions can be well-described as binary collisions. As the atoms reach lower energies, there are collisions which are strongly influenced by many-body effects. When simulating PKAs of any energy, it is necessary to be able to correctly model the low energy mechanisms of damage production such as replacement collision sequences.

Since dynamical models explicitly include many-body effects and assume only an interatomic potential as initial physical information, they can provide the most realistic simulations of radiation damage phenomena. However, because of limitations of computational time and computer size, dynamical models are limited to simulating low energy events. For example, the dynamical code COMENT[1] has been successfully applied to PKAs of not more than about 500 eV in copper, and dynamical simulations of up to keV range PKAs in tungsten[2] have also been performed.

By employing the binary collision approximation, the computer code MARLOWE[3] is very easily able to treat PKAs having energies of tens of keVs. It is fast, and can economically generate large numbers of cascades for statistical analysis. However, it is not clear that MARLOWE accurately models the lower energy aspects of a cascade, where many-body interactions are important. Also, MARLOWE does not simulate the time development of a cascade, since it treats only one binary collision at a time. MARLOWE has been run at low energies[4] and can be made to give about the same defect yields and replacement sequence lengths as dynamical codes by assuming an effective binding energy and an effective recombination radius. A more valid calibration of MARLOWE would be accomplished by comparing MARLOWE and dynamical simulations of fairly high energy cascades, where a realistic mix of high and low energy collisions occurs.

Unfortunately, COMENT is limited to less than 1 keV, but lying between the codes COMENT and MARLOWE, in concept and in energy range, is the code ADDES,[4] often labeled a quasi-dynamical code. It treats many-body interactions, but it can be made to ignore all but the most important interactions in the material by allowing only atoms having energies above a minimum value to participate. By optimizing parameters,[5] AODES can be made to model the essential dynamics of low energy events significantly faster than the fully dynamical codes. Thus, ADDES can be used to bridge the gap between the low energy COMENT code and the high energy MARLOWE code, having a considerable region of overlap with each. ADDES has already been carefully calibrated against COMENT for low energy PKAs in copper,[5]

but until now it has not been applied to many high energy events. The aim of the present work is to compare MARLOWE with ADDES simulations of PKAs at the highest possible energies.

2. The Model

The highest energy PKA ADOES can handle easily is about 1 keV when using parameter settings which produce the best fit to low energy results of COMENT. Defect production by PKAs up to 80 keV have been simulated, however, in two stages. Using ADDES, the cascade is allowed to develop until no atom has more than a relatively high cut-off energy (300-800 eV). As energetic atoms fall below the cut-off energy, they are tagged and removed from consideration during the remainder of the development of this first stage. In this way the gross features of the cascade are obtained without having to monitor the activities of every atom involved in each time step.

To get to the higher energies in reasonable times without affecting the dynamics, some changes had to be made to the original version of ADDES. In particular, throughout the event, the time step size is scaled by a fractional power of the instantaneous kinetic energy of the most energetic atom. Care was taken to allow energetic atoms to be "frozen" in such a way as to not affect the dynamics of major collisions. Freezing may happen only if the atom has been active for a minimum number of iterations, has reached a maximum of its kinetic energy, and has less than a prescribed cut-off value of potential energy. The result of the first stage is a "frozen" cascade, which contains energetic but temporarily fixed atoms as well as some atoms which have come to rest away from their lattice sites.

The second stage of the process is the evaluation of the damage produced by the energetic atoms tagged in the first stage. Although PKAs of identical energies and directions can be simulated by both ADDES and MARLOWE, it would be meaningless to attempt to compare the results on

a collision-by-collision basis. In ADDES, the many-body effects are a large enough perturbation on high energy collisions that minute differences in initial conditions can make major differences on the atomic level. One criterion for comparison which should be meaningful is the total defect production. The end result of an ADDES or MARLOWE simulation is a list of Frenkel pairs and their separations. The usual criterion for stability of a pair is that the defect separation is greater than a recombination radius empirically determined to give the appropriate defect yield.

In the second stage of the ADDES model, the defect yield of the frozen cascade (i.e., with temporarily frozen but energetic atoms) is determined analytically using an expression for the yield as a function of energy. The Frenkel pair yield determined for each energetic atom is added to the number of already existing pairs which meet the recombination criterion for stability.

ADDES was calibrated at low energies in copper with a modified Moliére-Englert potential.[6] The first stage of the high energy cascade modeling is being done using only the repulsive Moliére potential with the same screening radius (.00738 nm) as in the low energy simulations. Interactions above 5 eV are the same with either potential, and MARLOWE in its present configuration (Version 11) works best with the Moliére potential. Inelastic energy losses in MARLOWE are turned off so that they do not have to be included in ADDES.

3. Results

Calculations have been done with MARLOWE and ADDES for 10 keV PKAs in several directions in copper. This energy was chosen because it is high enough that directional effects should be small, yet the computations are still manageable. Simulations of 25 keV and 80 keV cascades have been performed with both MARLOWE and the two-stage ADDES models. At 80 keV it was necessary to increase the value of the threshold for displacement in both models, making the results somewhat questionable until further

testing of these paremeter settings can be done.

A study[7] comparing ADDES with experimental data at low energies concluded that a recombination radius of about 2 lattice units gives reasonable agreement. Throughout this work for both ADDES and MARLOWE, a recombination radius of 2.2 lattice units gave the best correlation of results.

The defect yield function used in this work (see the figure) was chosen to provide a reasonable fit to the defect yields obtained with COMENT using the Moliére-Englert potential for PKAs up to 200 eV. The function was linearly extrapolated to 800 eV. A further test of this yield function was that it should give the same total yield regardless of the ADDES freezing energy. The simple yield function shown in the figure gives the total yields indicated in Table 1 for a 10 keV PKA in a high index direction for cut-off energies ranging from 300 eV to 800 eV. Within a few percent these values are the same for all cut-off energies. The average value is 119 pairs.

Table 2 contains the yields obtained with a cut-off energy of 500 eV for 10 keV PKAs in several directions in copper.

As expected in this energy, the yield is fairly isotropic. Directional properties, associated with crystal lattice symmetries, become important at a few hundred eV and below. Once the 10 keV is distributed into amounts that small, however, sufficiently large numbers of randomly oriented secondary atoms are generated to make the defect yield independent of PKA direction. The isotropy also indicates that the application of a single yield function to the frozen atoms in the developing cascades is a valid procedure; that *is,* the spatial distribution of the momenta of frozen atoms is sufficiently random (or at least similar) for all PKA directions. At much lower energies, the two-stage model may not be useful because the small number of frozen secondary atoms would not provide an adequate statistical basis.

MARLOWE was used to model the same 10 keV PKAs in copper as done with ADDES. Table 2 contains the MARLOWE defect yields. The average MARLOWE and ADDES results agree very well considering the small number of runs. At 10 keV in copper, MARLOWE and ADDES, using the same effective recombination radius, give the same defect yields.

As an interesting comparison, MARLOWE was also made to run as a two-stage model with various cut-off energies. These MARLOWE runs were analyzed in the same manner as the ADDES runs using the same yield function. The yields for the same 10 keV PKA with cut-off energies between 300 eV and 800 eV along with the result with the usual MARLOWE model (a 5 eV cut-off) are included in Table 1. The results are similar to those of ADDES, and the two-stage MARLOWE models agree well with the usual MARLOWE result. Operating in the two-stage mode, and carefully fitted to experimental yield data at lower energies, MARLOWE could be used to determine defect yields for extremely high energy PKAs.

The energy distributions of the atoms in the two-stage MARLOWE and two-stage ADDES models are considerably different (in ways consistent with differences in the models), but both give the same defect yields. Thus, at least with respect to this yield function, both models partition the energy among the atoms of the cascade in the same way. This can be interpreted as a reaffirmation of the validity of the binary collision approximation.

The average yield for the 10 keV PKAs, about 117 pairs, is not meant to be indicative of the measurable number of defects for a 10 keV cascade. Inelastic losses will diminish this total by about 10% according to MARLOWE. In addition, since many of the atoms in the vicinity of the depleted zone still have energies considerably higher than thermal energies, a good deal of additional recombination may be expected. Understanding this recombination process may be the critical link between the models and directly measurable quantities.

The spatial distributions of defects in ADDES and MARLOWE cascades cannot be compared easily, at least at the present level of development, because in the two-stage ADDES model, the ultimate positions of the atoms are never determined. One fact regarding spatial distribution may be noted: In both models, the same yield results from the same recombination radius. This may be a necessary condition for the two models to give defect distributions of the same density, though it, of course, implies nothing about the actual shape or extent of the cascade. Some qualitative comparisons may be possible on the basis of the distribution of the momenta of the energetic frozen atoms. For example, one may see the potential for particular shapes to form, etc. However, quantitative comparisons can only be done on a statistical basis.

4. Conclusions

It has been demonstrated that dynamical models can be made tc simulate defect production yields in high energy cascades by the two-stage method described above. This is accomplished by applying a yield functior for lower energies which is consistent with dynamical simulations of low energy events, and which is independent of the cut-off energy in the two-stage model.

There is very good agreement between this model and MARLOWE for 10 keV PKAs in copper. Thus, the link between dynamical models and the binary collision model has been established at a fairly high energy.

VI. REFERENCES

1. J. O. Schiffgens and R. D. Bourquin, J. Nucl. Mat. 69, p. 790 (1978).

2. M. W. Guinan, Magnetic Fusion Energy Annual Report, July 1975 - September 1976, VCRL-50002-76 (1976).

3. M. T. Robinson and I. M. Torrens, Phys. Rev. 9, p. 5008 (1974)

4. D. M. Schwartz, J. O. Schiffgens, D. G. Doran, G. R. Odette, and R. G. Ariyasu, Computer Simulation for Materials Application, NBS 1, p. 75 (1976).

5. R. G. Ariyasu, D. M. Schwartz, and H. L. Heinisch, Jr., DAFS Progress Report, July - September 1978, DOE/ET-0065/3.

6. J. O. Schiffgens, D. M. Schwartz, R. G. Ariyasu, and S. E. Cascadden, Rad. Effects (accepted for publication).

7. G. R. Odette and D. M. Schwartz, Trans. Am. Nucl. Soc. 1977 Winter Meeting, San Francisco, p. 316 (1977).

VII. FUTURE WORK

A comparison of the spatial distribution of defects by MARLOWE and ADDES will continue to be investigated. Using MARLOWE, a systematic study of defect production by high energy PKAs will be done.

VIII. PUBLICATIONS

This information is to be presented at the First Topical Meeting on Fusion Reactor Materials, January 29-31, 1979, Miami Beach, Florida.

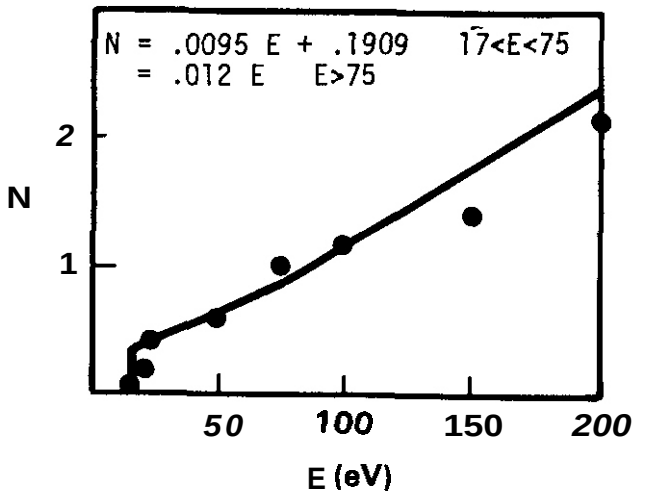

FIGURE 1. The Defect Yield, N, as a Function of Energy, E, used in the Analysis of Two-Stage Cascade Models. The points are results using COMENT.

TABLE 1

DEFECT YIELDS FOR A 10 KeV PKA IN COPPER BY TWO-STAGE ADDES AND MARLOWE MODELS

cut-off Energy in eV	Defect Yields	
	ADDES	MARLOWE
300	120	119
500	121	120
600	119	119
800	117	120
5	-	120

TABLE 2

DEFECT YIELDS FOR 10 KeV PKAs IN COPPER BY THE TWO-STAGE ADDES MODEL WITH A 500 eV CUT-OFF ENERGY AND BY MARLOWE

PKA Direction			Defect Yields	
θ	ϕ		ADDES	MARLOWE
90.0	0.3	~[100]	112	110
89.7	44.7	~[110]	119	110
54.8	44.9	41111	116	125
83.3	18.9		121	120
			117	116

CHAPTER 5

SUBTASK C: DAMAGE MICROSTRUCTURE EVOLUTION AND MECHANICAL BEHAVIOR

I. PROGRAM

Title: Radiation Effects in Fusion Reactor Structural Materials

Principal Investigator: J.A. Sprague

Affiliation: Naval Research Laboratory

II. OBJECTIVE

The objective of this study is to determine the effects of high-fluence neutron irradiation on the microstructure of refractory metals and alloys.

III. RELEVANT DAFS PROGRAM PLAN TASK/SUBTASK

II.C.1 Effects of Material Parameters on Microstructure

IV. SUMMARY

The refractory metals molybdenum, niobium, and vanadium, and the alloys TZM, niobium - 1% zirconium, and vanadium - 20% titanium examined by transmission electron microscopy following irradiation at 650°C to fluences of 5.4×10^{26} n/m^2, E >0.1 MeV (all materials except V-20% Ti) and 8.4×10^{26} n/m^2, E >0.1 MeV (Mo and V-20% Ti). Voids representing significant volume swelling were observed in the Mo (2.3 - 3.0%), TZM (4.0%), Nb (1.5%) and V *(3.6%)*. Some precipitation occurred during irradiaton in all materials except the Mo and V. The results indicate that void swelling can probably be controlled at moderate levels at this temperature in refractory alloys. Degradation of mechanical properties due to irradiation - enhanced or - induced precipitation may, however, be a more serious problem.

V. ACCOMPLISHMENTS AND STATUS

The Microstructures of Neutron - Irradiated Refractory Metals and Alloys - J. A. Sprague, F.A. Smidt, Jr., and J.R. Reed (Naval Research Laboratory, Washington, DC 20375).

1. Introduction

Alloys based on the bcc refractory metals are of interest for fusion reactor first-wall and blanket applications, principally because they offer higher reactor operating temperatures than would be possible using iron-, nickel-, or titanium-based alloys. The use of refractory alloys in fusion reactors will require the expansion of our current data base on these materials and their behavior following high-fluence irradiation at elevated temperatures. The present experiments were undertaken to survey the microstructural response of molybdenum, TZM, niobium, niobium - 1% zirconium, vanadium, and vanadium - 20% titanium to high-fluence neutron irradiation at 650%. These results supplement previous work by a number of investigators to provide a basis for the more systematic and comprehensive experiments that will be required to adequately define the irradiation response of refractory metals and alloys.

2. Experimental Procedures

The pure Mo (>99.95%), Nb (>99.99%), and V(>99.95%) were obtained from Materials Research Corporation in the form of 50-um thick foil. (Note that the above nominal purities are for substitutional solutes only.) The TZM (Mo-0.5 wt.% Ti-0.1 wt.% Zr), Nb-1 wt.% Zr, and V-20 wt.% Ti materials were rolled to 50-um thick foil from commercial-grade stock. Following the punching of 3-mm dia. disks, the metals and alloys were all annealed in a vacuum of 1.3×10^{-4} Pa for 1 hour at 1430°C, except for the V and V-20 Ti, which were annealed at 885%. The foils were packed into close-fitting stainless steel tubes which were evacuated, back-filled with helium, and welded shut. The foil tubes were loaded into sodium-filled heat-pipesontrolled irradiation capsules (1) for irradiation in the EBR-II reactor. Two capsules were used in the present experiments, both designed to operate at 650 ±10°C. The first (EBR-II subassembly (X-200), which contained **all** materials except the V-20 Ti, was irradiated in Row 7 to a fluence of 5.4×10^{26} neutrons/m , E>0.1 MeV. The second capsule (EBR-II subassembly X-255) containing the Mo and

V-20 Ti was irradiated in several positions, mostly in Row 2, to a fluence of 8.4 x 10^{26} neutrons/m^2, E>0.1 MeV. Following irradiation, the foils were electrochemically thinned and examined by transmission electron microscopy.

3. Results and Discussions

The experimental results will be discussed in each of the following subsections by comparing each pair of pure metal and alloy, in turn. The quantitative void distribution data for those materials that exhibited significant void formation are all collected in Table 1, and will be referenced in each subsection, as needed.

TABLE 1

VOID DISTRIBUTIONS OBSERVED AFTER NEUTRON IRRADIATION AT 650°C

Material	Fluence (E-0.1 MeV)	Void Density (m^{-3})	Mean Diam. (nm)	Swelling %
Mo	5.4 x 10^{26}	1.0 x 10^{23}	7.8	3.0
Mo	8.4 x 10^{26}	9.8 x 10^{22}	7.2	2.3
TZM	5.4 x 10^{26}	5.2 x 10^{22}	10.5	4.0
Nb	5.4 x 10^{26}	2.1 x 10^{23}	4.6	1.5
V	5.4 x 10^{26}	5.5 x 10^{20}	42.1	3.6

3.1 Mo and TZM

The microstructures of the Mo at both fluences and the TZM at the lower fluence were similar, consisting of imperfectly ordered void lattices and moderate densities of dislocation loops and line segments. Examples of these microstructures are shown in Fig. 1. The total dislocation density in each of the

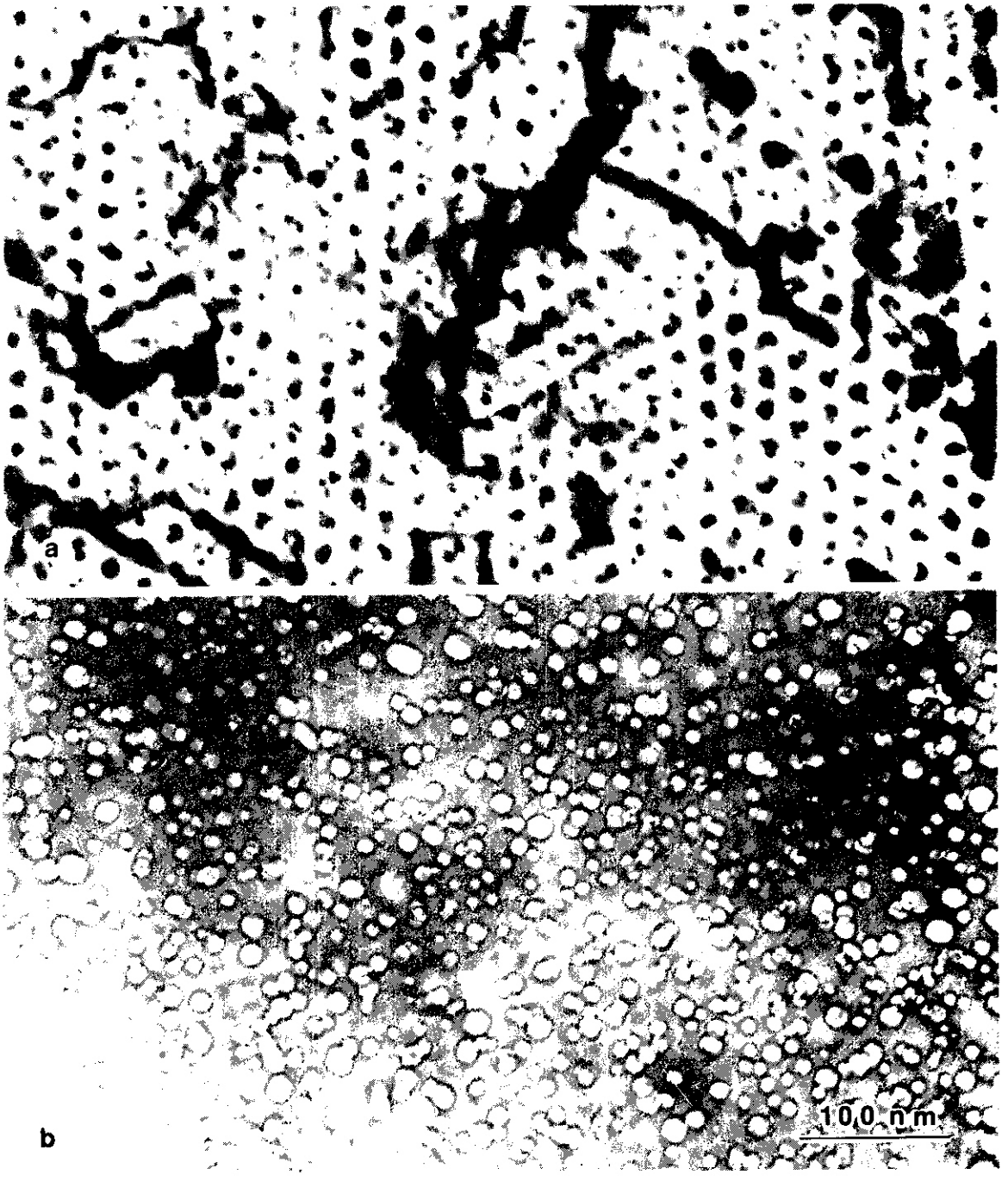

Fig. 1 Representative microstructures observed in (a) Mo, and (b) TZM after neutron irradiation at 650°C. The voids in Mo appear dark due to a combination of strain contrast and overfocus.

specimens examined was in the range 5 - 7 x $10^{13} m^{-2}$. A low density of globular precipitates were observed in the TZM. In the pure Mo, a void lattice parameter of 30 nm was measured for both fluences, which is in good agreement with previous lower-fluence measurements of void lattice parameter as a function of irradiation temperature (2,3). Some ordering, onapproximately the same scale as in the Mo, could be detected in the TZM, but a good void lattice parameter determination could not be made, due to the relatively large size of the voids and the imperfections in the ordering. Referring to the void distribution data in Table 1, it can be seen that the swelling measured in TZM at the lower fluence was slightly greater than that in the pure Mo, although the difference was within the error limits for these determinations. At the higher fluence, where the only data was for the pure Mo, the swelling was actually smaller than at the lower fluence, although the difference was again within error limits. Both void densities and mean diameters in the Mo were similar at both fluences. The TZM contained a lower density of significantly larger voids, a number of which appeared to have coalesced from multiple smaller voids formed earlier in the irradiation. A final observation was that the voids in the pure Mo were surrounded by strong strain fields, which were easily visible in dark field, using a $\langle 110 \rangle$ g-vector. No strain fields of similar magnitude were observed surrounding the voids in TZM.

The present observations of the relative swelling in Mo and TZM agree fairly well with previously reported results of other investigators. At low neutron fluences ($\sim 10^{24} n/m^2$), Bentley, et all (4) reported a complete suppression of void formation in TZM over the temperature range 330 - 850 °C, while voids were observed in pure Mo for all of these conditions. At higher fluences of 2.5 -4.4 x $10^{26} n/m^2$, E>0.1 MeV, Bentley and Wiffen (2) observed comparable swelling in Mo and TZM at 425 and 585 °C, and slightly greater swelling in TZM at 790 and 1000 °C. Their conclusion, which is supported by the present results, was that the minor alloying additions in TZM suppress swelling at low fluences, probably by slowing down void nucleation, and enhance swelling at high fluences, by increasing void growth. More observations at higher fluence will be required to determine if the apparent saturation in the swelling of Mo is maintained, and if the enhanced void growth in TZM produces really significantly larger swelling with increased exposure.

3.2 Nb and Nb - 1% Zr

The Nb contained a very high density of small voids, as illustrated in Fig. 2a, as well as a much lower density of small (~10 nm) precipitates in the matrix. The void lattice parameter, assuming a bcc structure, was 24 nm. The swelling, as seen from the data in Table I, was considerably less than that in the other pure metals or the TZM. The Nb-1Zr, was shown in Fig. 2b, contained a high density of precipitates. A few voids, ~5 nm in diameter, were observed in isolated areas of the foil, but these did not represent any significant swelling. This observation of suppression of swelling in Nb-1Zr agrees with the results of Michel and Moteff (5) and Jang and Moteff (6), who both reported significant swelling in Nb-1Zr only over the temperature range 700-900°C at a fluence of 5 x 10^{26} n/m^2, E>0.1 MeV. The void distribution observed in the present study, however, was quite different from that reported by Michel and Moteff, in that the voids observed here were smaller, and the number density was approximately an order of magnitude larger. The reasons for this difference cannot be determined unambiguously, but they are probably related to the impurity contents of the materials in the two studies. First, the material used in Michel and Moteff's work was commercial-grade Nb, as opposed to the high-purity stock used in the present experiment. Second, the specimens in the present study were annealed as 50-um thick foil in a 1.3 x 10^{-4} Pa vacuum at 1430°C. Although the specimen holder in the furnace was made of tantalum, considerable contamination (on the order of a few thousand parts per million) by interstitial impurities probably occurred (7). This conclusion is reinforced by the precipitation which occurred during irradiation. The pre-irradiation annealing conditions for the material used in Michel and Moteff's work were not specified. It seems reasonable, :therefore, that interactions of substitutional and interstitial impurities were responsible for the different void distributions.

3.3 V and V - 20 % Ti

The microstructure of the irradiated pure V was quite different from those of the Mo and Nb, as shown in Fig. 3a. The pre-irradiation annealing treatment had produced a fine grain size (5 - 10 μm), and after irradiation, each grain

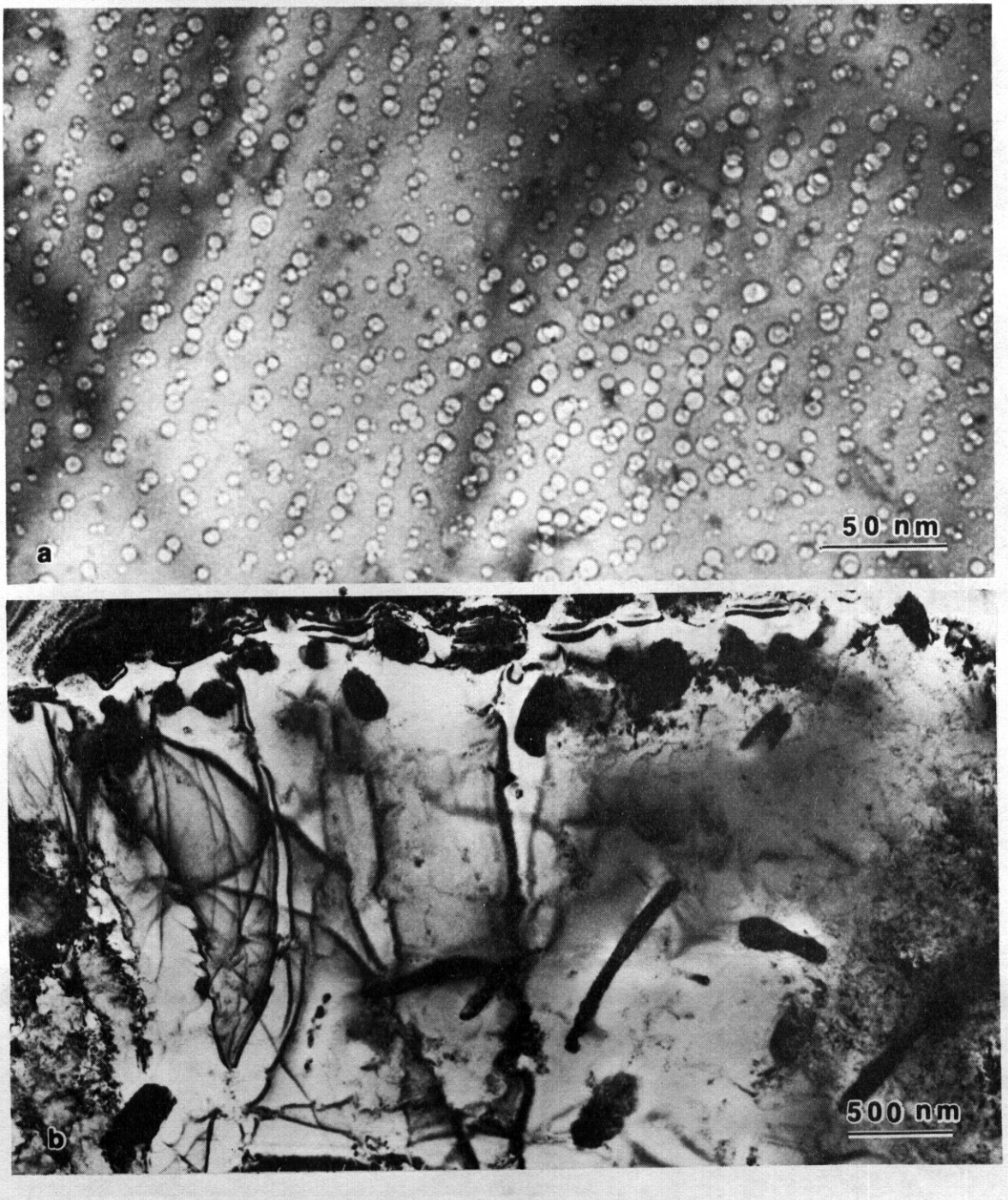

Fig. 2 Representative microstructures observed in (a) Nb, and (b) Nb - 1 % Zr after neutron irradiation at 650°C. Note different magnifications in the two micrographs.

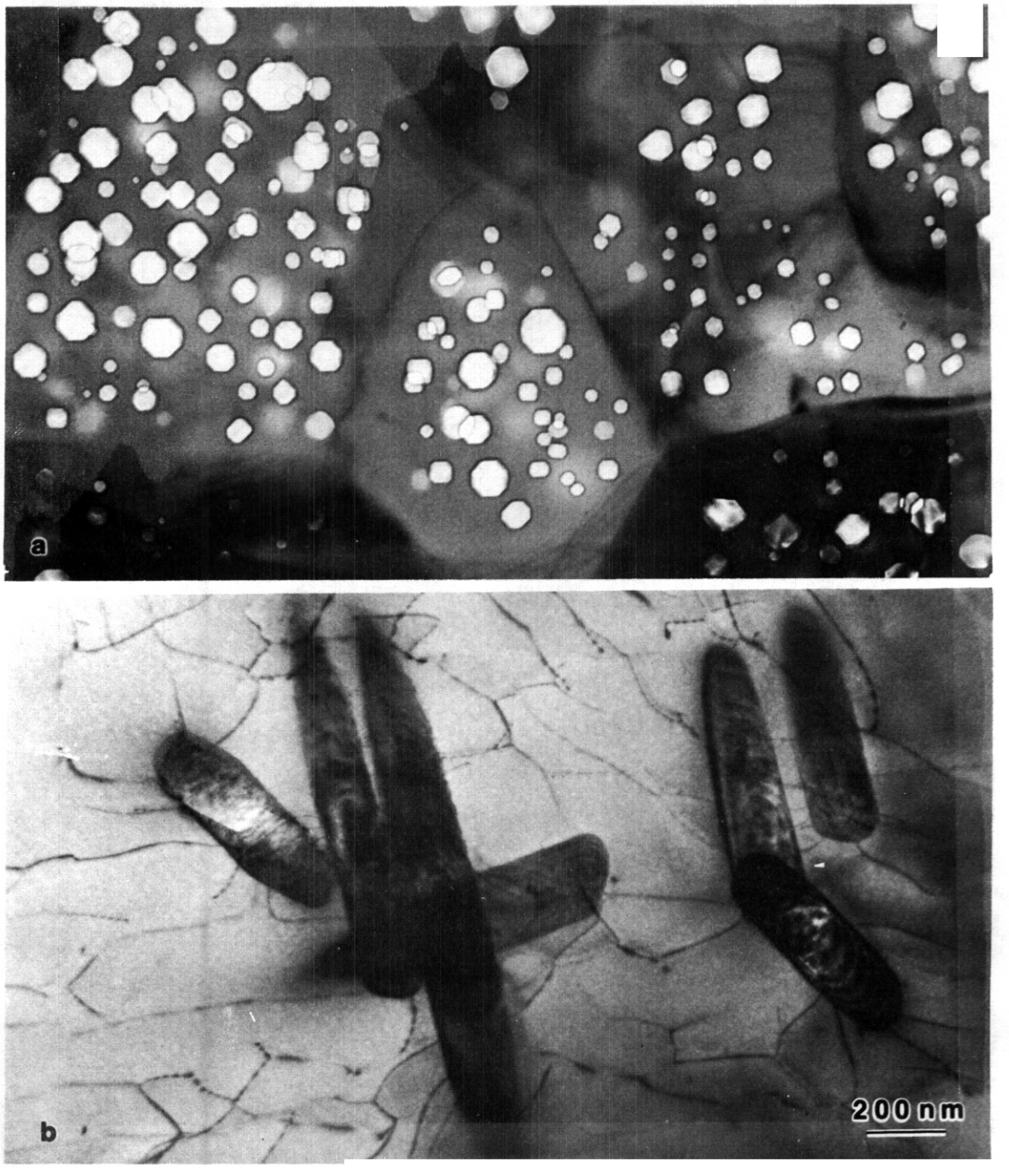

Fig. 3. Representative microstructures observed in (a) V, and (b) V - 20 % Ti after neutron irradiation at 650°C.

contained a moderate density of fairly large voids. The voids were denuded near each grain boundary. The dislocation density in the grain interiors was low, ~1 x 10^{13} m^{-2}, although many dislocations were observed in subgrain boundaries. No precipitates were observed. The V-20Ti, which was irradiated to the higher fluence of 8.4 x $10^{26}/m^2$, E>0.1 MeV, contained a high density of small precipitates of various morphologies, as shown in Fig. 2b. The dislocation density in this material was low, and no voids were observed.

The complete suppression of void formaton by the addition of 20% Ti to V agrees with the results of Bentley and Wiffen (8), who examined V-20Ti irradiated to fluences of 1.3 - 6.1 x 10^{26} n/m^2, E >0.1 MeV, at temperatures between 470 and 780°C. They also observed precipitates in their specimens after irradiation. Carlander (9) reported a few voids in V-20Ti after irradiation to 6 x 10^{26} n/m^2, E>0.1 MeV, at 600°C, although these voids did not represent any significant swelling. The void microstructures in the pure V are difficult to correlate with those reported previously for lower fluence irradiations (9,10), due to differences in starting materials and irradiation temperatures, but the observation of 3.6% swelling at 5.4 x 10^{26} n/m^2 is consistent with approximately linear swelling with fluence, when compared with the 1.54% swelling reported by Carlander (9) for irradiation to 2.5 x 10^{26} n/m^2 at 625 C and the 1.47% swelling reported by Stiegler (10) for irradiation to 1.4 x 10^{26} n/m^2 at 600°C (all fluences for E> 0.1 Mev).

4. Conclusion

The present microstructural observations of refractory metals and alloys after high-fluence neutron irradiation at 650°C indicate that, at least at this temperature, void swelling will probably not be the most serious obstacle to the application of this class of alloys to fusion reactor structures. The swelling of even the pure metals is only moderate, and with the possible exception of Mo alloys, it appears possible to control void formation further by alloying. Changes in mechanical properties due to radiation-induced precipitation and the formation of high densities of small voids may be far more serious problems. Theoretically, the precipitation could be controlled by reducing the concentrations of interstitial

impurities, but more comprehensive studies on thoroughly characterized materials will be required to examine this possibility. If detrimental changes in microstructure can be avoided by careful control of impurities, fabrication technologies and reactor operating conditions will still have to be developed to maintain this impurity control in large structures. If these developments can be made, however, refractory metal alloys appear to be potentially valuable for fusion reactor first-wall and blanket applications.

VI. REFERENCES

1. J.E. Deverall and H.E. Watson, "Temperature Control in Irradiation Experiments with Gas-Controlled Heat Pipes," Proc. ANS Topical Meeting on Irradiation Experimentation in Fast Reactors, American Nuclear Society (1973) 267.

2. J. Bentley and F.W. Wiffen, "Neutron Irradiation Effects in Molybdenum and Molybdenum Alloys," Technology of Controlled Nuclear Fusion, CONF-760935-PI (1976) 209.

3. J. Moteff. V.K. Sikka, and H. Jang, "The Influence of Neutron Irradiation Temperature on the Void Characteristics of BCC Metals and Alloys," Proc. Consultant Symposium on The Physics of Irradiation Produced Voids, AERE-R7934, United Kingdom Atomic Energy Authority (1975) 101.

4. J. Bentley, B.L. Eyre, and M.H. Lorreto, "Suppression of Void Formation in Neutron Irradiated TZM," in Radiation Effects and Tritium Technology for Fusion Reactors, CONF-750989 (1976) 1-277.

5. D.J. Michel and J. Moteff, "Voids in Neutron Irradiated and Annealed Niobium and Niobium - 1% Zirconium Alloy," Rad. Effects 21 (1974) 235.

6. H. Jang and J. Moteff, "The Influence of Neutron Irradiation Temperature on the Void Characteristics of Niobium and Niobium - 1% Zirconium Alloy", in Radiation Effects and Tritium Technulogy for Fusion Reactors, CONF-750989 (1976) I-106.

7. B.A. Loomis, A. Taylor, and S.B. Gerber, "Void Swelling of Nb and Nb-1% Zr Induced by Ni Bombardment," J. Nuclear Material 56 (1975) 25.

8. J. Bentley and F.W. Wiffen, "Swelling and Microstructural Changes in Irradiated Vanadium Alloys," Nucl. Technology 30 (1976) 376.

9. R. Carlander, S.D. Harkness, and A.T. Santhanam, "Effects of Fast Neutron Irradiation on Tensile Properties and Swelling Behavior of Vanadium Alloys," in Effects of Radiation on Substructure and Mechanical Properties of Metals and Alloys, ASTM STP 529, American Society for Testing and Materials (1973) 399.

10. J.O. Stiegler, Void Formation in Neutron-Irradiated Metals," in Radiation-Induced Voids in Metals, AEC Symposium Series 26 (1972) 292.

II. FUTURE WORK

Following the identification of the precipitate phases observed in this study, work on this set of materials will be completed. Further microstructural examinations of irradiated refractory metals and alloys in the Fusion Materials Program will concentrate on well-characterized materials in the program and more comprehensive irradiation matrices to fully understand the behavior of this class of materials.

VIII. PUBLICATIONS

A paper, entitled "The Microstructure of Neutron-Irradiated Refractory Metals and Alloys," has been submitted to the First Topical Meeting on Fusion Reactor Materials, Miami Beach, Florida, 29-31 January 1979. The proceedings of this conference will be published in Journal of Nuclear Materials.

I. PROGRAM

Title: Effects of Irradiation on Fusion Reactor Materials
Principal Investigator: F. V. Nolfi, Jr.
Affiliation: Argonne National Laboratory

II. OBJECTIVE

The objective of the work is to determine the extent and chanracteristics of solute redistribution during irradiation of candidate classes of MFR alloys and its concomitant effect on phase stability and materials properties.

III. RELEVANT DAFS PROGRAM PLAN TASK/SUBTASK

SUBTASK II.C.1.1 Phase Stability Mechanism Experiments

IV. SUMMARY

Radiation-induced solute segregation (RIS) to external surface in Fe-18Cr-8Ni; Fe-18Cr-8Ni-1Si; Fe-18Cr-8Ni-1Mo; and Type 316 stainless steel (MFE Ht. #15893) alloys under 3.5 MeV $^{58}Ni^{+}$ ion irradiation has been investigated in order to determine the segregation behavior of alloying additives in complex engineering alloys. Chemical depth profiling by Auger electron spectroscopy of the irradiated surfaces revealed that Ni and Si (when present) segregate to the surface while Cr and Mo (when present) segregate away from the surface.

V. ACCOMPLISHMENTS AND STATUS

A. Radiation-Induced Solute Segregation — V. K. Sethi

Recent experimental observations on a number of alloy systems subjected to displacement-producing irradiation show significant RIS of

alloying elements to and away from external surfaces, grain boundaries and other internal sinks[1-8]. The phenomenon is a general one, and can adversely affect alloy properties that are known to be composition dependent. An understanding of RIS and its extent in complex engineering alloys is thus of considerable importance to fusion reactor technology.

The direction of segregation of solutes viz., towards or away from point-defect sinks, has been predicted on the basis of size-effect by Okamoto and Wiedersich[3]; undersize solutes are enriched and oversize solutes are depleted at point-defect sinks.

Evidence exists that the extent of segregation is significantly affected by minor alloying additions. For example, small quantities of Si in Fe-20Ni-15Cr alloy enhance segregation of all the alloying constituents[8]. Our initial results on the effects of minor additions of various elements on RIS in Fe-Cr-Ni base alloys are presented in this report.

Samples in the form of 3 mm disks were punched out from rolled stock of Fe-18Cr-8Ni; Fe-18Cr-8Ni-1Si; Fe-18Cr-8Ni-1Mo and Type 316 stainless steel (FME Heat #15893). Samples were solution annealed in vacuum for 2 h at 1050°C and air cooled. Stainless steel samples were aged at 800°C for 8 h after the solution anneal. Prior to irradiation, one surface of each samples was metallographically polished optically flat and then electropolished to remove any cold-worked surface material.

Irradiations were performed by P. R. Okamoto at the Argonne National Laboratory Dual-ion Irradiation Facility with 3.5 MeV $^{58}Ni^{+}$ ions in 10^{-8} torr vacuum. An infra-red pyrometer was used to monitor the individual sample temperatures during irradiation. Alloy samples were irradiated at various temperatures to various dose levels at a peak damage-rate of $\sim 2 \times 10^{-3}$ dpa/s. Damage doses were calucalted by the Brice codes RASE3 and DAMG2[9] using a displacement energy of 40 eV.

Chemical depth profiling by Auger electron spectroscopy was performed with the assistance of A. Purohit, using a primary electron beam of 3KV and 10μA to excite the transitions. Depth profiling was accomplished by sputtering with 1kV argon ions in an argon atmosphere at 5 x 10^{-6} torr. Sputtering was interrupted periodically to record the Auger spectra. The concentrations of major elements were calculated using sensitivity factors determined from standard alloys. For minor elements, viz., Si and Mo, the sensitivity factors used were those available in the literature.(10)

Figure 1 illustrates the composition-depth profiles of Fe-18Cr-8Ni and Fe-18Cr-8Ni and Fe-18Cr-8Ni-1Mo alloys that were irradiated at 600°C to a peak dose of 60 dpa. Figures 2 and 3 show the composition-depth profiles of Fe-18Cr-8Ni-1Si and Type 316 stainless steel at comparable peak doses (-3 dpa) and temperatures. The highlights of these profiles are discussed in the following.

1. In all the alloys, at all temperatures the segregation behavior of the major alloying elements is qualitatively similar, and is consistent with predictions of the size-effect model. Ni is an undersize solute and is enriched in the near surface region, while Cr is an oversize solute in these alloys and is depleted. Similarly, the segregation behavior of minor alloying additives is consistent with the size-effect model; Si is enriched while Mo is depleted at the surface.

2. Comparison of the RIS profiles in Figure 1 reveals that the addition of Mo significantly alters the composition profiles of each of the major alloying elements.

3. RIS is temperature dependant, Figures 2 and 3, and maximum segregation occurs in the 400-500°C range. The available data is too limited to define the maximum segregation temperature more precisely.

VI. REFERENCES

1. P. R. Okamoto, S. D. Harkness and J. J. Laidler, ANS Tans., Vol. 16, 1973, p. 70.

2. P. R. Okamoto, A. T. Santhanam, H. Wiedersich and A. Taylor, Nucl. Technol., Vol. 22, 1974, p. 45.

3. P. R. Okamoto and H. Wiedersich, J. Nucl. Mater., Vol. 53, 1974 p. 336.

4. E. A. Kenik, Scripta Met., Vol. 10, 1976, p. 733.

5. A. Barbu and A. J. Ardell, Scripta Met., Vol. 9, 1975, p. 1233.

6. K. Farrell, J. Bentley, and N. D. Braski, Scripta Met., Vol. 11, 1977, p. 243.

7. D. I. Potter, L. E. Rehn, P. R. Okamoto and H. Wiedersich, International Conference on Radiation Effects in Breeder Reactor Structural Materials, 1977, p. 377.

8. W. G. Johnston, W. G. Morris and A. M. Turkalo, International Conference on Radiation Effects in Breeder Reactor Structural Materials, 1977, p. 421.

9. D. K. Brice, Sandia Laboratories, Albuquerque N. M., Research Report SLA-73-0416 (1973).

10. "Handbook of Auger Electron Spectroscopy" Physical Electronics Industries, Inc. (1976).

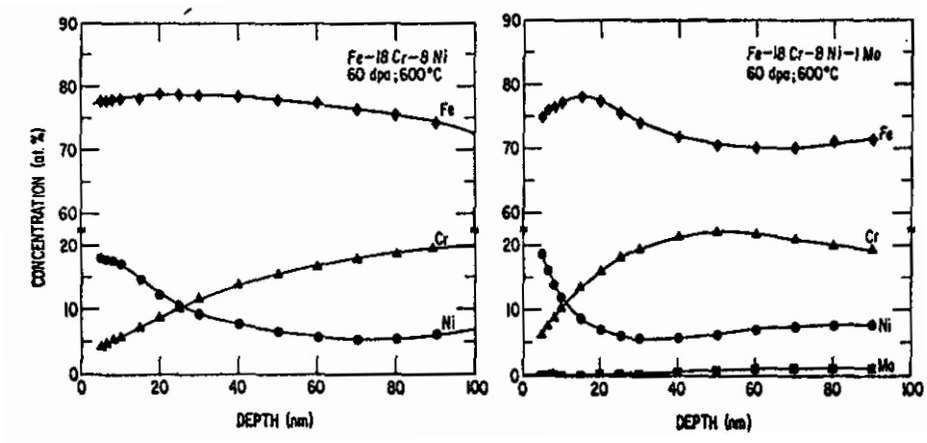

FIGURE 1. RIS profiles of Fe-18Cr-8Ni and Fe-18Cr-8Ni-1Mo alloys.

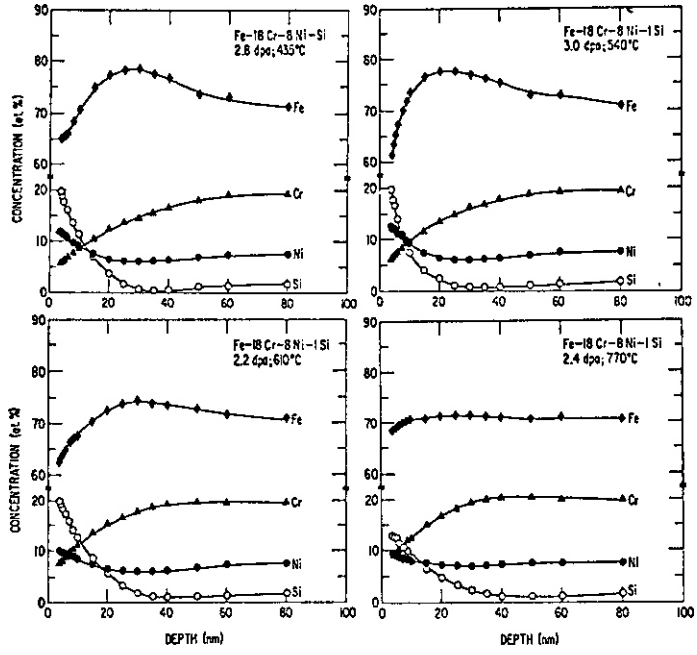

FIGURE 2. RIS profiles for Fe-18Cr-8Ni-1Si alloy for various temperatures.

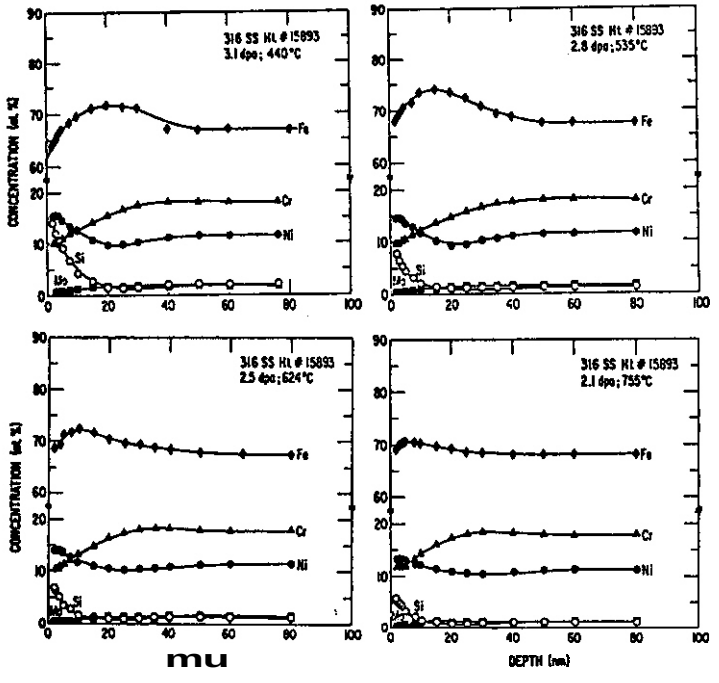

FIGURE 3. RIS profiles for Type 316 stainless steel (MFE Ht. #15893) for various temperatures.

I. PROGRAM

Title: Irradiation Response of Materials
Principal Investigators: J. A. Spitznagel, W. J. Choyke
Affiliation: Westinghouse Research and Development Center

II. OBJECTIVE

The objective of this work is to assess the phenomenology and mechanisms of microstructural evolution in materials exposed to simultaneous helium injection and creation of atomic displacement damage by a second ion beam.

III. RELEVANT DAFS PROGRAM PLAN TASK/SUBTASK

SUBTASK II.C.2.1. Helium Mobility, Distribution and Bubble Nucleation

IV. SUMMARY

Helium distribution in Mo was shown to depend on the choice of electronic stopping law used.

V. ACCOMPLISHMENTS AND STATUS

In the previous quarterly report[1] earlier work[2] at the High Energy Ion Bombardment Simulation (HEIBS) Facility at the University of Pittsburgh, under separate funding using the *a-a* scattering technique to measure helium distribution was briefly summarized. The technique is sufficiently sensitive to distinguish whether helium transport occurs on the scale of 1-100 μm (i.e. over distances on the order of the grain size in solution annealed metals) or tenths of a micron. However, measurement of helium motion on the

order of 10^0-10^2 nanometers (i.e. the typical intersink spacing in an irradiated metal) is not possible with this technique. It is possible that a nuclear reaction technique such as the $^3He(d,p)\alpha$ reaction could give information on the effects of momentum transfer, detrapping and radiation-enhanced diffusion on a scale of tens of nanometers. The nuclear reaction technique has the advantage of requiring only the 2 Mv Van de Graaff and, unlike the *u-a* scattering technique, does not tie up the large accelerator needed for the dual ion irradiation experiments. However, uncertainties in the projected range (Rp) and straggle (ΔRp) of implanted ^3He ions, and the necessity for using shielding and low ion beam currents to minimize the neutron irradiation hazard present formidable problems.

As a result of work funded by sources outside DoE, it is evident that the experimentalist is faced with a confusing array of choices for calculating light ion ranges and range straggling in metals and non-metals. Figure 1 shows several possible choices for the energy dependence of the electronic stopping power of ^3He ions in Mo. The result of using this variety of current electronic stopping formulations to calculate projected ranges and straggle with the EDEP-1 code is ~50% uncertainty in R_p and up to 100%uncertainty in ΔR_p. It is clear that this can seriously affect helium doping of specimens for ion or neutron irradiation and complicate studies of helium transport. Consequently, Choyke[3] has recommended a DoE funded workshop of "experts" to determine which data tables and which calculations should be used.

VI. REFERENCES

1. J. A. Spitznagel and W. J. Choyke, DAFS Quarterly Progress Report No. 3, p. 146. July-September (1978).

2. W. J. Choyke, J. A. Spitznagel, J. N. McGruer and J. S. Lally, J. Nucl. Mater. 74, 303 (1978).

3. W. J. Choyke, Letter to T. C. Reuther, DoE, Office of Fusion Energy, Nov. 9, 1978.

4. L. C. Northcliffe and R. F. Schilling, Nuclear Data Tables, A7:233 (1970).

5. J. F. Ziegler and W. K. Chu, Atomic and Nuclear Data Tables, 13:463 (1974).

6. J. F. Ziegler, He Stopping Powers and Ranges in All Elements, Pergamon Press, New York (1977).

VII. FUTURE WORK

Progress in this area will hinge on resolving the uncertainties in calculated range statistics for implanted helium and on evaluation of the neutron irradiation hazard resulting from deuteron bombardment.

VIII. PUBLICATIONS

None

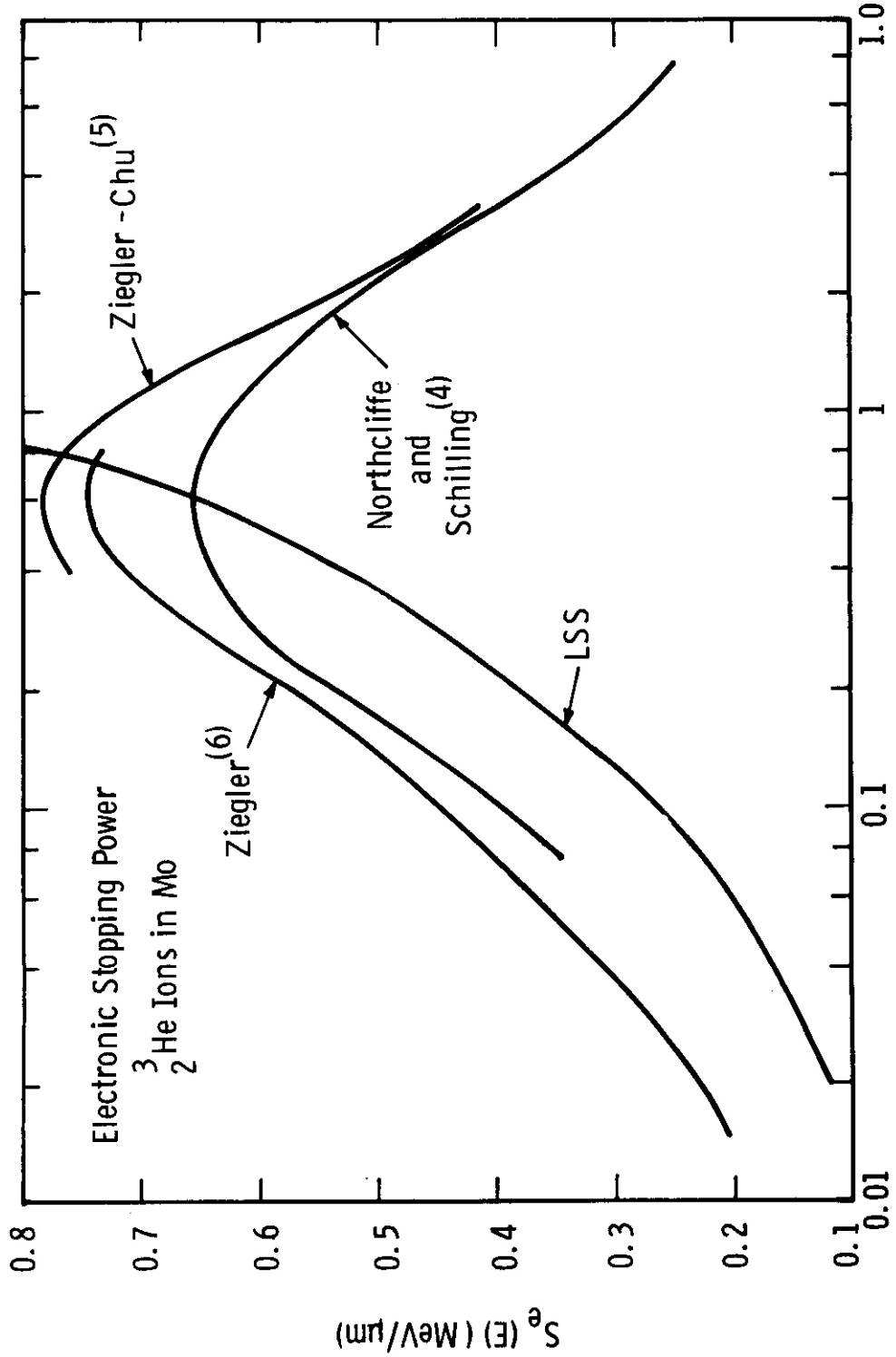

FIGURE 1. Current Electronic Stopping Power Formulations Available for Calculating Range Statistics for $^3_2$He in Molybdenum.

I. PROGRAM

Title: Synergistic Helium Production by Boron Doping of Splat Cooled Alloys

Principal Investigator: O. K. Harling

Affiliation: Nuclear Reactor Laboratory, Massachusetts Institute of Technology

II. OBJECTIVE

This work is directed toward the development of better simulation techniques for the synergistic production of helium and displacement damage in first wall structural materials.

III. RELEVANT DAFS PROGRAM PLAN TASK/SUBTASK

A number of tasks are relevant since adequate experimental simulation of fusion reactor irradiation effects is a major reason for the DAFS program. Some of the tasks/subtasks which are significantly affected are:

TASK	II.A.4	Gas Generation Rates
	II.C.2	Effects of Helium on Microstructure
	II.C.8	Effects of Helium and Displacement on Fracture
	II.C.13	Effects of Helium and Displacement on Crack Initiation and Propagation

VI. SUMMARY

Initial results of scanning auger electron spectroscopy are presented for the characterization of boron in SS.

Based on the flux measured in the so-called "Controlled Thermo-Nuclear Reactor Facility" (CTRF), preliminary estimates of the displacement and helium generation rates in a 316 stainless steel have been made.

It is found that the displacement rate peaks at approximately 9.3×10^{-8} s^{-1} at a position 25 cm from the bottom of the CTRF, and also that the helium production rate is easily manipulated by the addition of small quantities of boron to the steel.

V. ACCOMPLISHMENTS AND STATUS

A. Boron Doping of Stainless Steel by Rapid Quenching – S. West, G. Dansfield, O. Harling, and K. Russell (M. I. T.)

1. Introduction

It is generally understood that existing irradiation facilities, i.e. accelerators and fission reactors, will have to be used for the initial irradiation testing of fusion reactor (FR) structural materials. Damage rates and helium production rates should simulate the expected rates in FR's. Only fission reactors offer the required large testing volumes with fast neutron fluxes which produce damage rates which equal or exceed those expected for near term FR's. Helium production rates, with the exception of nickel alloys in mixed spectrum reactors, cannot be reproduced by direct nuclear reaction on the alloy constituents. The present studies are directed toward the development of techniques for the production of helium during fission reactor irradiations. Current efforts emphasize the doping of structural alloys with boron. To assure the uniform distribution of boron, the alloy is produced by rapid quenching from the melt. Cooling rates of 10^5 – 10^9°C/sec offer the possibility of uniform boron concentrations which are much higher than those which can be maintained without segregation during normal solidification rates. The usefulness of this approach to boron doping will also depend upon the maintenance of a uniform boron distribution during thermo-mechanical consolidation, and during the use of the consolidated material in the temperature, stress and radiation environment of the fission reactor. Furthermore, the effect of boron on the physical properties of the boron doped alloys, whether segregated to grain boundaries or uniformly distributed, must be understood.

This quarterly report deals with our efforts to characterize the boron distribution with auger electron spectroscopy, to calculate displacement damage rates and helium generation rates for MITR-II, and to produce rapidly quenched alloys doped with boron.

2. Characterizing the Boron Distribution by Auger-Electron Spectroscopy

The method of neutron autoradiography for characterization of the boron distribution in stainless steel has been previously reported. (1) The resolution of this technique is about 0.3 μm, making it useful for grain sizes below 2 Um. We are now investigating the use of high resolution auger electron spectroscopy for this purpose. Preliminary results are available for conventionally cooled materials, but not for splat cooled material.

Boron segregation in conventionally cooled stainless steel was observed using auger electron spectroscopy. The instrument used for the analysis was a Physical Electronics model 590A scanning auger spectrometer (SAM). Conventionally cooled material was chosen because of availability, and because boron segregation in the material had been previously reported.[1] The material investigated was type 316 stainless steel to which 0.5 w.% boron had been added. After sectioning, the material was mechanically polished and etched with Kalling's reagent to reveal the dendritic structure. In the analyzing chamber, approximately 125 angstroms of material was sputtered from the surface to remove oxygen and other surface contamination.

Two types of analysis have proven useful for detecting boron segregation. The first is a line scan across the sample, with the spectrometer set for boron auger electrons. The relative boron signal strength as a function of position can then be superimposed on a secondary electron picture of the surface. Figure 1 is an example of this, showing a higher boron concentration between the dendrites. This analysis was

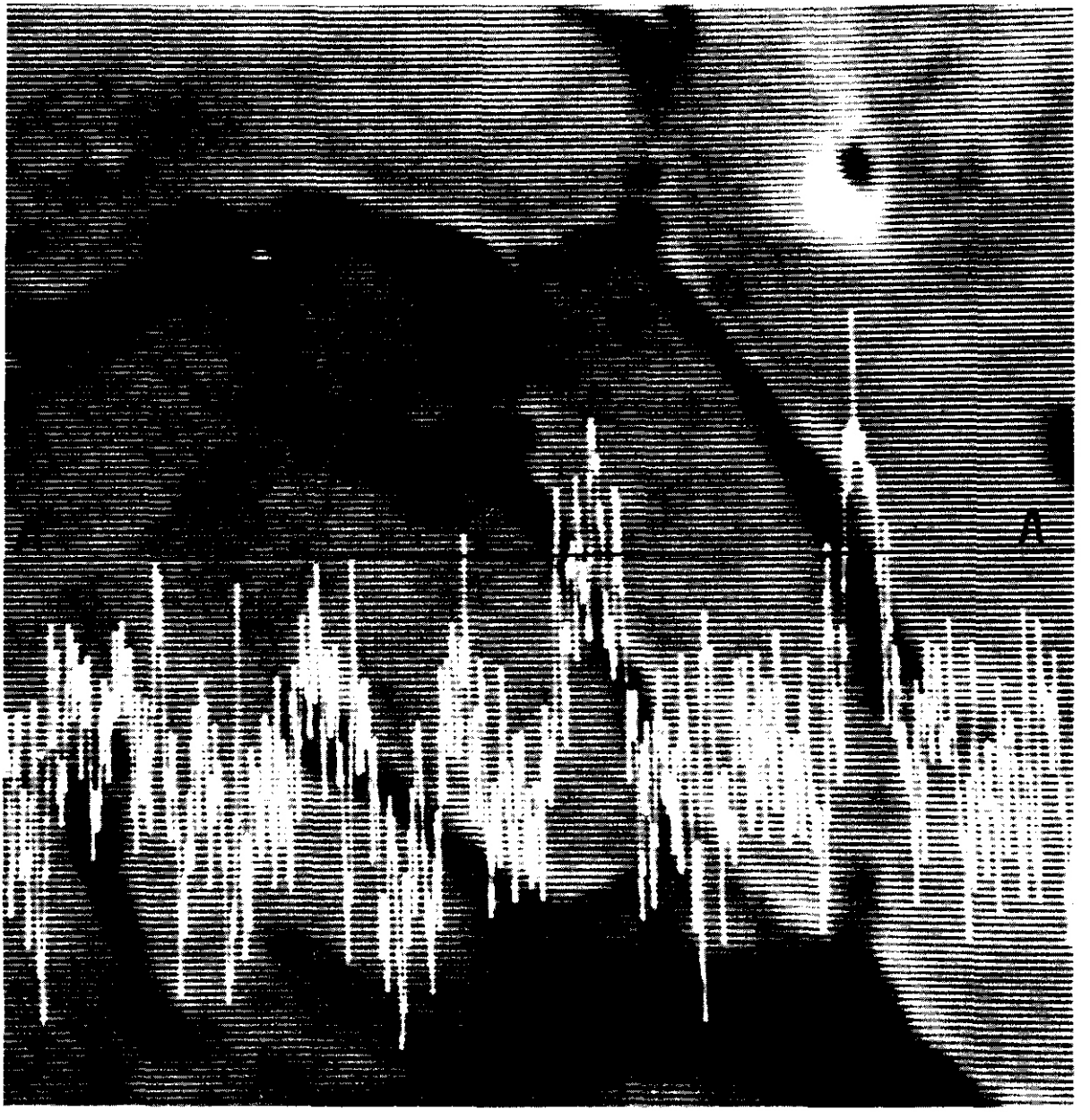

Figure 1. This figure shows the boron auger electron signal strength as a function of position along line AA. The secondary electron picture of the surface was obtained by polishing and etching the surface prior to sputtering. The material is conventionally cooled type 316 stainless steel doped with 0.5 w.% boron. 5100x.

made with a beam size of approximately 0.5 μm, which scanned along line AA in the figure. A second method of analysis is to scan in one spot for the differential auger electron signal as a function of energy, around the boron peak. These techniques give high elemental sensitivity but depend on independent knowledge concerning the likely locations for boron segregation, e.g. in grain and dendrite boundaries. Further work is planned for each method.

3. Neutron Flux Characterization and Damage and Helium Production Estimates in the MITR-II.

The redesign of the MIT Research Reactor (MITR-II) was completed in 1976.[2,3] Since that time, there has been a growing interest in the development of materials testing and radiation damage capabilities to be used in conjunction with the reactor facilities currently available. Towards this end, flux measurements and damage and helium production calculations have been made for the central in-core irradiation facilities of the MITR-II.

The results of the flux measurements made in one of the in-core sample assemblies [the so-called "Controlled Thermonuclear Reactor Facility" (CTRF)] were reported in the previous DAFS Quarterly Report (15 October, 1978). Since that time, the cross section set used has been updated to agree with the cross sections recommended by the ENDF/B IV file and the flux has been recalculated based on these values. The major effect of these changes was that the flux above 6 Mev was increased by ∿11%. (The peak flux above 6 Mev increased from 1.82×10^{16} m^{-2} s^{-1} to 2.05×10^{16} m^{-2} s^{-1} as a result of this.) In addition to these changes, and based upon an evaluation of measurements made by Kirk and Greenwood[4], we have determined that the spectrum averaged cross section used in our earlier work to calculate the flux above 1 Mev from the ^{58}Ni (n,p) ^{58}Co reaction was high by a factor of ∿30% because the neutron spectrum at 1 Mev in the CTRF is considerably softer than the fission spectrum which we assumed. Our revised spectrum averaged cross section for the

^{58}Ni (n,p) reaction was taken to be 100 mb ("45% smaller than the corresponding cross section measured in the Low-Temperature Fast-Neutron Facility in CP-5), increasing the peak value of the MITR-II flux above 1 Mev from 5×10^{17} m^{-2} s^{-1} to 6.9×10^{17} m^{-2} s^{-1}

Based on the measured flux, estimates of the displacement rate and the helium production rate in a 316 stainless steel as a function of position in the CTRF were made. The composition of the steel is given in Table 1.

Table 1. Composition of the 316 Stainless Steel

Element	Fe	Cr	Ni	Mo
w/o	Bal.	17	12	2
Element	**Mn**	**si**	**C**	**N**
w/o	2	1	0.06	0.002

Since no flux spectrum unfolding was done for these calculations, it must be emphasized that they are preliminary estimates. The damage energy cross sections used are those of Doran and Graves[5] for an 18/10 stainless steel. The displacement energy, T_d, was taken to be 40 ev. Below 1 Mev, the flux shape was taken from a 15 group CITATION calculation since no flux measurements were made for energies less than 1 Mev. (CITATION is a reactor physics code used by the Operations Staff of the MITR-II to calculate the neutron flux and power peaking factors for various operating core configurations.) Figure 2 shows a typical example of the flux shape predicted by CITATION for a central core position. The flux shape below 1 Mev was fitted by three exponential curves covering the energy range of interest. The magnitude of the flux below 1 Mev was assumed to scale linearly with the flux above 1 Mev. For example, the 15 group Citation calculation indicated that the flux above 0.1 Mev was

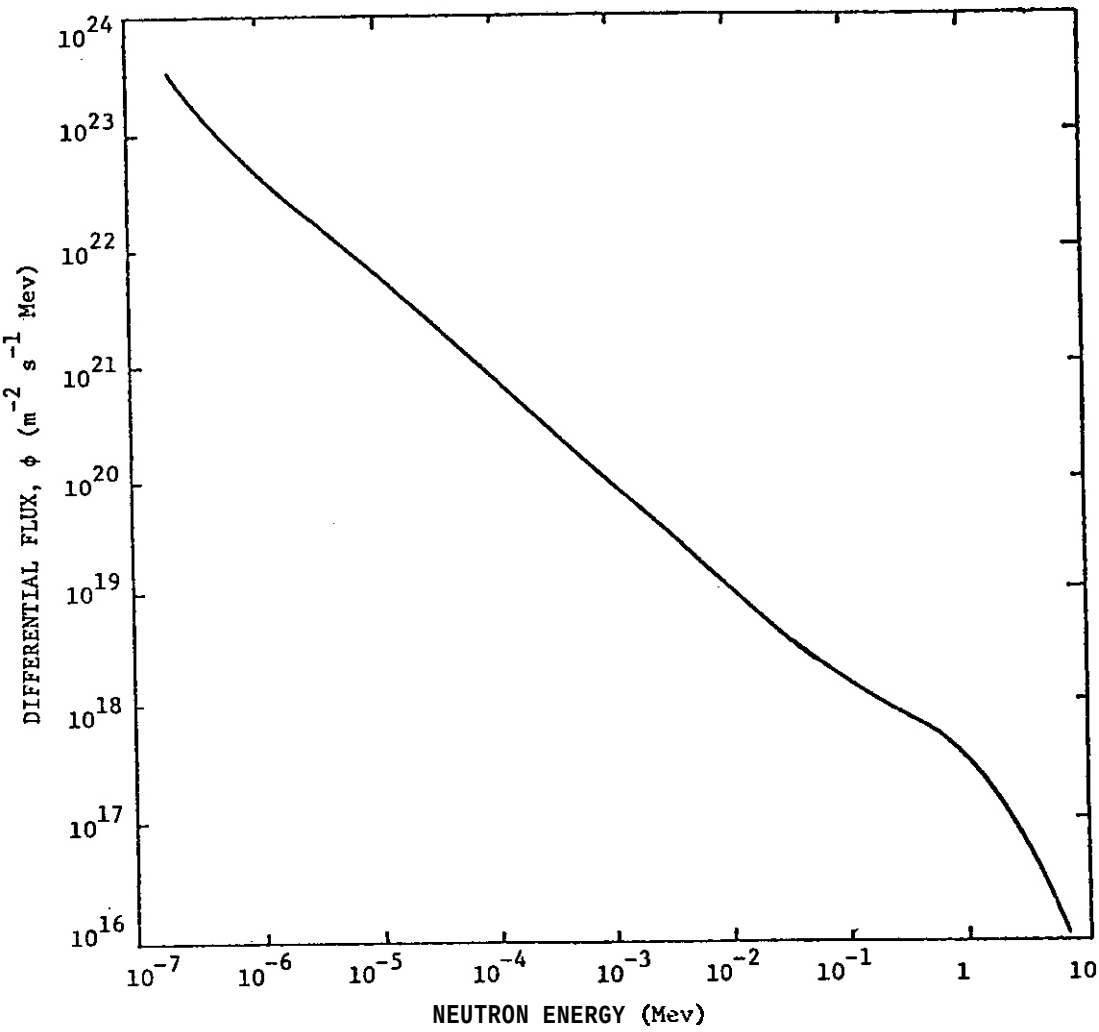

FIGURE 2: **Typical Neutron Spectrum Calculated by CITATION for a Mid-Core Position in the CTRF of the MITR-II**

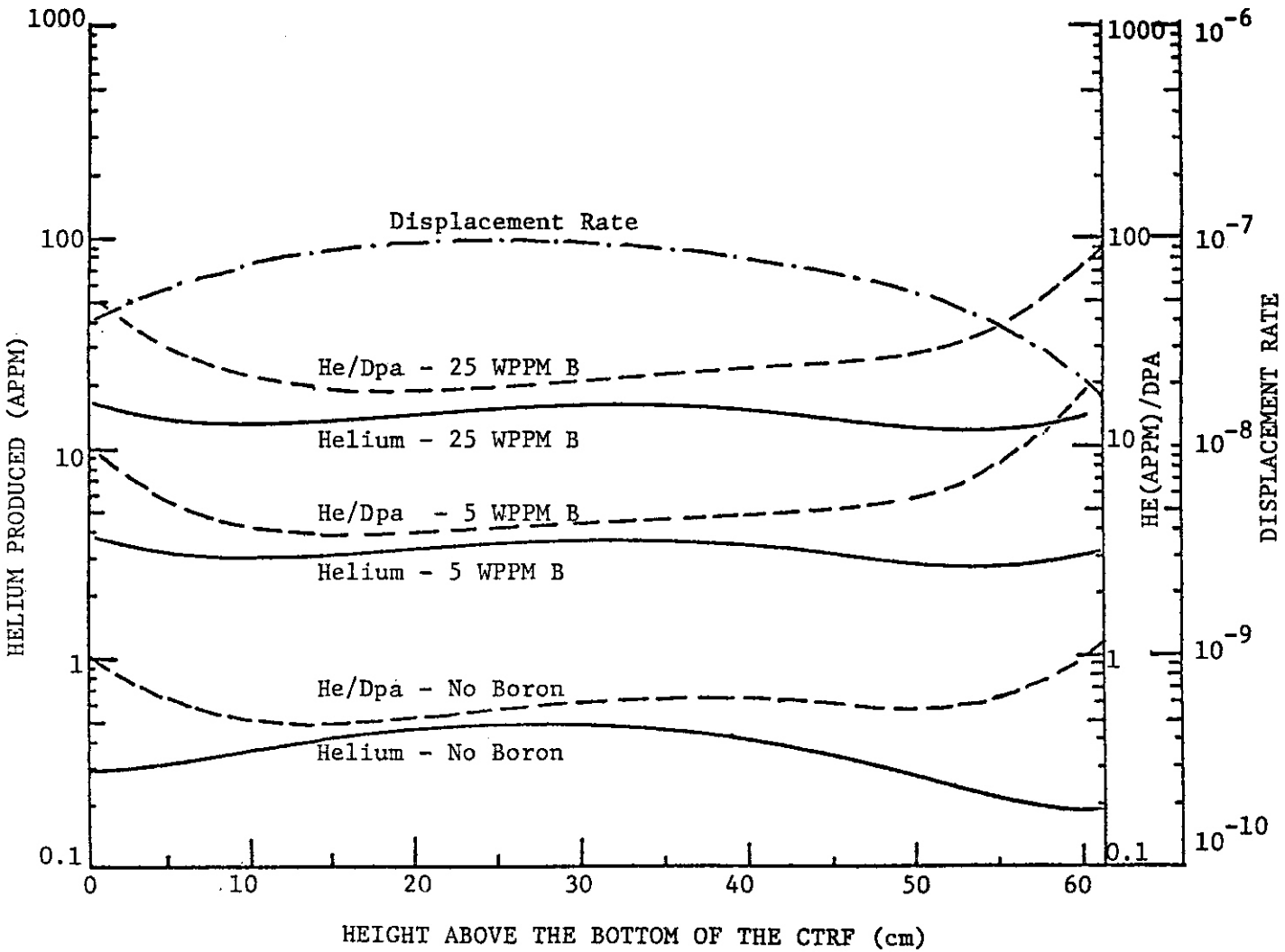

FIGURE 3 Displacement Rate, He Produced and He/Dpa Ratio in 316 SS After 100 Full Power Days in the CTRF.

$\sim$2.3 times greater than the flux above 1 Mev over most of the length of the CTRF. Above 1 Mev, the measured flux spectrum was used and a fission spectrum shape was assumed for interpolation within each experimental energy group. Use of this assumption clearly leads to an overestimation of the displacement rate. The magnitude of this error is difficult to estimate without a more detailed analysis of the flux shape. The displacement rate calculated using these assumptions is shown in Figure 3.

Figure 3 also shows the amount of helium generated and the helium to dpa ratio after 100 full power days of irradiation in 316 stainless steel containing various amounts of boron. The total amount of helium generated also includes helium from high energy (n, α) reactions and from the thermal ^{58}Ni two-step reaction. It is interesting to note that the helium generation rate in the CTRF can be effectively tailored by the addition of small amounts of boron to the steel and also that the He/dpa ratio is relatively flat over large portions of the CTRF.

4. Production of Rapidly Quenched Alloys Doped with Boron

The production of roll quenched stainless steel foils doped with boron was not possible because of an equipment failure. The molybdenum surface of the rolls broke during a run. New rolls are being manufactured.

VI. REFERENCES

1. A. Fadaai, "Determination of the 3-D Boron Distribution," A Thesis submitted in partial fulfillment of the requirements for a M. S. in Nuclear Engineering at the Massachusetts Institute of Technology June, 1978.

2. G. C. Allen, "The Reactor Engineering of the MITR-II Construction and Startup," Ph. D. Thesis, Massachusetts Institute of Technology, Department of Nuclear Engineering, MITNE-186 (1976).

3. P. C. Meagher and D. D. Lanning, "Design of Central Irradiation Facilities for the MITR-II Research Reactor," M. S. Thesis, Massachusetts Institute of Technology, Department of Nuclear Engineering, MITNE-190 (1976).

4. M. A. Kirk and L. R. Greenwood, "Determination of the Neutron Flux and Energy Spectrum in the Low-Temperature, Fast-Neutron Facility in CP-5, Calculations of Primary-Recoil and Damage-Energy Distributions, and Comparisons with Experiment," To Be Published, J. Nuclear Mat.

5. D. G. Doran and N. J. Graves, "Displacement Cross Sections and PKA Spectra: Tables and Applications," HEDL-TME 76-70 (1976).

VII. FUTURE WORK (Near Term)

Additional work is planned to improve our capability to characterize the boron distribution using auger electron spectroscopy. Following the production of boron doped material in the roll quenching apparatus, the boron distribution will be characterized with neutron autoradiography and auger electron spectroscopy.

An optimal mechanical property test will be designed to determine the effects of boron doping in the boron doped alloys.

High resolution secondary ion micropobe analysis for characterization of the boron distribution will be investigated.

In the near term no work is planned in the area of the characterization of the neutron flux in the MITR-II. Somewhat further in the future, however, more detailed flux measurements **and** flux spectrum calculations will be made in conjunction with materials irradiation projects in the MITR-II and corresponding displacement and helium generation rates will be calculated.

I. PROGRAM

Title: Irradiation Effects Analysis (WHOII/EDA)
Principal Investigator: D. G. Doran
Affiliation: Hanford Engineering Development Laboratory

II OBJECTIVE

The objective of this work is to calculate the enhanced deposition of reaction products in "halos" that occur around precipitates that contain alpha-emitting elements.

III. RELEVANT DAFS PROGRAM PLAN TASK/SUBTASK

SUBTASK II.C.2.1 Mobility, Distribution, and Bubble Nucleation
SUBTASK II.C.2.4 Modeling

IV. SUMMARY

Expressions have been developed to describe the deposition of reaction products about spherical precipitates subject to (n,α) reactions. An optimum precipitate size is shown to exist for analysis of the effects of helium on microstructural development. Analysis of several experiments shows that both lithium and helium atoms exert an influence on the development of voids during irradiation. Several methods of obtaining multiple helium/dpa ratios in a single irradiation are described.

V. ACCOMPLISHMENTS AND STATUS

A. Analysis of the Helium Halo Effect in Neutron Irradiated Alloys - F. A. Garner and D. S. Gelles (HEDL)

1. Introduction

In a previous report[**] it was noted that an experimental alloy containing small boride particles developed spherical shells or "halos" of enhanced swelling about them during irradiation in EBR-II. Such halos have been observed by other researchers[2-7] and have been found to contain enhanced densities of various microstructural components such as dislocation loops, voids, helium bubbles, precipitates or black spot damage. The identity of the components depends on the irradiation temperature, alloy, neutron fluence and spectra, and the identity of the reaction product causing the halo. When both reaction products cause observable damage, concentric halos are formed.

It has been proposed[1] that these halos could be employed to study the effects of helium on microstructural evolution. Such an experiment would involve comparative analyses of the microstructure that develops within the halo and that which develops just outside the halo. It is expected that pre-existing microchemical variations would be small in the two adjacent areas, and that these would allow measurement of the effect of a single variable. It would therefore be important to ensure that the regions studied were not influenced by both reaction products.

An experiment of this nature requires the ability to calculate the particle deposition rate and associated displacement rate both within and outside the halo. The following sections define the conditions best suited to the conduct of such an experiment.

2. Particle Deposition Rate Within the Halo

The precipitate is assumed to have radius r_p and density ρ_p and to contain a known density of atoms subject to (n,α) events. The energetic particles are born with a distribution of energies $N(E_o)$ and travel in paths assumed to be straight lines with total ranges $R_p(E_o)$ in the precipitate phase and $R_m(E_o)$ in the matrix phase. The rest distribution of

atoms about the range is assumed to be Gaussian and to be defined by the straggling parameter $\Delta R(E_o)$. Figure 1 shows that the inner and outer limits (R_i and R_o) of the halo can be defined for a given energy in terms of $R_p(E_o)$, $R_m(E_o)$ and r_P.

$$R_o = R_m(E_o) + r_p \quad [1]$$

$$R_i = R_m(E_o) + r_p(1-2m) \quad [2]$$

$$m = \rho_p/\rho_m = \frac{R_m(E_o)}{R_p(E_o)} \quad [3]$$

Equation [3] states that the range is inversely proportional to the density of the material, which is true for alpha particles and other light ions. Energetic particles which must travel through both phases as defined by equation [2] are subject to the Geiger Rule which states that particles which travel through two materials must obey the relation

$$d_p/R_p(E_o) + d_m/R_m(E_o) = 1, \quad [4]$$

where d is the distance traveled in a particular phase.

When $m = 1.0$ and $\Delta R(E_o) << R(E_o)$, the distribution of deposition rates within the halo is easy to define as shown in Figure 2. Only those particles born on the portion of the spherical surface defined by $R_m(E_o)$, centered at $dV(r)$, and which lies within the precipitate can be deposited in $dV(r)$, providing that the particle was directed at $dV(r)$. With some patience it can be shown that the volumetric deposition rate is

$$\dot{D}(E_o,r)_{m=1} = \frac{\dot{S}(E_o)}{2}\left[\frac{r^2+r_p^2-R_m(E_o)^2}{2rR_m(E_o)} - \frac{r}{R_m(E_o)} + 1\right]$$

$$= \frac{\dot{S}(E_o)}{4rR_m(E_o)}\left[r_p^2 - (r-R_m(E_o))^2\right] \qquad [5]$$

where $S(E_o)$ is the volumetric birth rate of particles. It can be noted that if $r = R_m(E_o)$ then $\dot{D} = \dot{S}(E_o)\, r_p^2/(4\, R_m(E_o)^2)$.

$$\dot{S}(E_o) = C(t)\phi\bar{\sigma}_{n,\alpha}(E_o) \qquad [6]$$

where $C(t)$ is the current concentration of reactive atoms, $\bar{\sigma}_{n,\alpha}(E_o)$ is the spectrum-averaged cross section and ϕ the total flux.

Integrating over the entire halo, expression 5 yields total conservation of particles as expected.

$$\int_{R_m(E_o) - r_p}^{R_m(E_o) + r_p} \dot{D}(E_o,r)\, 4\pi r^2 dr = \frac{4}{3}\pi\, r_p^3 \dot{S}(E_o) \qquad [7]$$

For most experimental studies, an appropriate average deposition rate over the area A should be calculated such that

$$\dot{D}_{avg} = \int_{r_1}^{r_2} \dot{D}(E_o,r)\, dA(r) \Big/ \int_{r_1}^{r_2} dA(r) \qquad [8]$$

For some combinations of neutron spectra and (n,α) reactions the particle source is not at a single monoenergetic energy. An integration

of equation [5] over the source distribution is thus required.

$$\dot{D}(r) = \int_{E_o(min)}^{E_o(max)} \dot{D}(r,E_o)\, dE \qquad [9]$$

Precipitates rich in nickel and subjected to environments with large thermal and fast neutron components will generate such a source distribution by the time-dependent build-up of the two-stage $^{58}Ni(n,\gamma)^{59}Ni(n,\alpha)^{56}Fe$ reaction.

When $m \neq 1.0$ the source surface within the precipitate is not spherical and considerable complexity is introduced. To a good first approximation however,

$$\dot{D}_{avg}(m \neq 1) = m^{-1}\, \dot{D}_{avg}(m = 1.0)\ , \qquad [10]$$

providing the area analyzed is centered in the halo and $R_m >> 2$ rp.

3. Displacement Rate Within the Halo

For typical (n,α) reactions, the displacement level generated by the particles as they slow down is small compared to the displacements generated by the usual displacive reactions. For nickel placed in a thermal neutron environment, however, the (n,α) cross section would be large and the displacement rate small, and the additional displacements in the halo would be a substantial fraction of the total. The fractional increase I in displacement rate can be approximated by

$$I = \frac{D_{avg}\, A_m\, N_d}{\rho_m\, \bar{\sigma}_d\, N_a\, \phi} \qquad [11]$$

where A_m, ρ_m and $\bar{\sigma}_d$ are the molecular weight, density and spectral-averaged cross section of the matrix, N_d is the total number of displacements per particle, N_a is Avogadros number and ϕ is the total neutron flux.

4. Optimum Particle Size

There is an optimum particle radius r_p^* which maximizes the width of the halo, thus minimizing the gradients in deposition, while also insuring that the two halos do not overlap. (As shown in a later section, the latter consideration is quite important.)

$$r_p^* = [R_m(\bar{E}_o,2) - R_m(\bar{E}_o,1)] / 2m \quad , \qquad [12]$$

where $\bar{E}_o$ is the mean birth energy of the source and the designations 1 and 2 refer to the shorter and longer range reaction products respectively.

5. Nature of Deposition Profiles

The distributions are not symmetric with respect to the center of the halo. In order to minimize the gradient of the desired element, it is best that the particle range be as large as possible. Fortunately, the alpha particle usually has the longest range of the reaction products, although this is not always the case. It is also important not to allow overlapping deposition of the reaction products. Figure 3 demonstrates these principles for a hypothetical example in which the alpha particle has a range of 2.5 μm and the other reaction product has a range of 1.0 μm. Note that for various precipitate radii the broadest nearly-uniform and nonoverlapping profile is obtained for the helium halo at the optimum particle radius r_p^* = 0.75 μm. The lower decsity of helium compared to the other reaction product is a consequence of the greater volume in which the helium atoms are deposited.

Note also that this example was chosen such that the inner

halo intersected the precipitate surface prior to intersection of the two halos. The inner halo for large precipitates is approaching the linear dependence predicted for large, flat interfacial precipitates.

Figure 3 also demonstrates that the level of helium is quite dependent on the particle size. A factor of ten or more difference in helium level can be obtained using particles ranging from a radius of r_p^* to a reasonable fraction of r_p^*. This reasonable fraction is determined by the criteria that the area analyzed be large compared to the size of the microstructural components being studied. Since the displacement level is essentially equal in all halos, a variety of helium/dpa ratios can be studied in a single irradiation of one specimen.

6. Experimental Example

The successful use of this technique requires the identification of the precipitate composition in order to determine C(t). If a variety of source precipitates exist it is thus necessary to retain the precipitate within the thin foil section employed for the microstructural analysis. If the precipitates are only of one type with well-defined stoichiometry, the latter restriction can be relaxed and r_p calculated from the ring width using expressions [1] and [2]. Stereomicroscopy is useful to determine the relative positions of the precipitate and halo with respect to the foil section. The use of non-equatorial sections of the halos requires appropriate geometrical corrections. The identity of the reactive isotope can be ascertained from measurements of the range of the two recoil products. This requires that the precipitate be retained in the foil, however. These considerations are all employed in analysis of the following experiment.

Void swelling studies have been conducted in the EBR-II reactor using an experimental precipitation-hardened austenitic stainless steel containing 30 w/o nickel, 10 w/o chromium, and lesser amounts of molybdenum, titanium, aluminum, manganese, silicon and a trace of boron (0.0007

w/o). The boron has been found to be almost totally contained in small precipitates (about 0.3 μm) formed prior to irradiation. These precipitates were identified by X-ray lattice parameter determinations as M_3B_2.[8] In a related alloy containing these same precipitates, the metal atoms have been found to be Mo, Ti, Cr, Fe, Al and Ni in rough order of decreasing concentration.[9] Energy-dispersive X-ray analysis in a scanning transmission microscope confirmed that the precipitates are indeed rich in molybdenum and contain the other elements in roughly that order. Since the nickel concentration of the precipitate is below that of the matrix, only the boron atoms function as an alpha source in the case. As shown in Figure 4, a ring of enhanced void nucleation about an M_3B_2 precipitate occurred at a range of about 1.3 μm in a specimen irradiated to 2.0 x 10^{22} n/cm^2 (E>0.1 MeV), about 8 dpa, at 400°C. This halo is caused by the ^{7}Li product of the ^{10}B(n,α) reaction; no visible enhancement occurred at about 2.5 μm, the expected range of the alpha particle. The lithium ring width is comparable to the precipitate diameter which suggests that $\rho_p/\rho_m \equiv m \approx 1.0$. Actually m = 6.88/7.92 = 0.87.

Using the following parameters, the deposition profiles can be calculated for each expected ring. The profiles pertaining to Figure 4 are shown in Figure 5.

$$m = 0.87, \quad r_p = 0.145 \ \mu m$$

$$E_o^{Li} = 0.84 \text{ MeV}, \quad E_o^{\alpha} = 1.47 \text{ MeV}$$

$$R_{Li}(0.84) = 1.3 \ \mu m, \quad R_{\alpha}(1.47) = 2.6 \ \mu m$$

$$\Delta R_{Li} = 0.09 \ \mu m, \quad \Delta R_{\alpha} = 0.17 \ \mu m$$

$\bar{\sigma}_{n,\alpha}$ = 2 x 10^{-4} barns for the matrix and 1.0 barns for the boron atoms

$\bar{\sigma}_d$ = 417 barns, ϕ = 2.0 x 10^{15} n/cm^2-sec

According to equation [12], the optimum particle radius r_P^* is 0.75 μm, considerably larger than that of the example. The example given in Figure 4 therefore exhibits considerably steeper profiles than those produced by a precipitate with radius r_P^*. As shown in Figure 6, the peak lithium and helium deposition rates are 6.0×10^{-7} and 1.5×10^{-7} appm/sec, respectively. The latter represents about 40% maximum increase over the background helium generation rate and is too small to yield an observable halo. There is clearly an effect of the small lithium concentration on void nucleation, however, which confirms the validity of thenon-overlapping halo criterion. The ion-induced displacement damage is much less than one percent of the total in both halos.

Table 1 shows data for halos and associated precipitates measured in two other specimens irradiated at a slightly higher temperature, 430°C, but at fluence levels of 2.8 and 7.0×10^{22} n/cm^2 (E>0.1 MeV). In all three specimens there was a noticeable enhancement of void nucleation in the lithium halo while an enhancement in the helium halo was only found at 7.0×10^{22} n/cm^2. Note in Figure 7 that the effect of lithium deposition is more pronounced in the early stages of irradiation but is later overtaken by the effect of the additional helium. The disagreement of measured density changes and local matrix swelling represents not only the normal inhomogeneity of swelling at low fluences but also the influence of the radiation-induced precipitation of other phases, which leads to several tenths of a percent densification at these temperatures.

7. Discussion

The technique described above can be tailored to suit a given alloy by selection of appropriate precipitates, which may occur naturally or which may be deliberately introduced. Several routes are available for the introduction of such precipitates, For alloys containing boron, the particle size distribution and density can be controlled by melting and homogenization procedures. For M_3B_2 for instance, dissolution of the boron occurs at 1200-1300°C,[9] which suggests that aging at 1150-1200°C should

promote the formation of large M_3B_2 particles. Farrel of Oak Ridge has successfully introduced preformed B_4C particles into may pure metals.[10] In some metals it may be possible to form precipitates with lithium and use the $^6Li(n,\alpha)$ reaction to form halos of helium and lithium. For systems forming nickel-enriched phases the use of appropriate neutron spectra may allow the two-step nickel reaction to provide the alpha source.

This technique is quite sensitive to neutron spectrum as indicated in Table 2.[11] This sensitivity allows the study of helium-affected microstructural development under conditions wherein the helium/dpa ratio approaches much larger values than those in Table 1. The use of thermal neutron absorber materials around some specimens will vary the helium deposition rate substantially but not the background displacement rate. This allows a number of helium/dpa ratios to be studied in one reactor spectrum. As discussed earlier, a range of helium/dpa ratios can also be obtained in one specimen by analyzing the halos about precipitates of .varying size. This is illustrated in Table 1.

The halo will experience a somewhat compressive stress state if it exhibits an enhanced swelling rate. The situation here is directly analogous to that of other constrained films studied earlier.[12] The stress state will be determined by the ratio of the local swelling rate and creep compliance. The two tend to increase together and the level of stress will not be so high as to yield substantially different swelling from unconstrained regions.

VII. REFERENCES

1. Gelles, D. S. and Garner, F. A,, "An Experimental Method to Determine the Role of Helium in Neutron-Induced Microstructural Evolution," HEDL-SA-1610A.

2. P. Vela, J. Hardy, and B. Russell, J. Nucl. Mat. 26, pp. 129-131 (1968).

3. D. A. Woodford, J. P. Smith, and J. Moteff, J. of Iron and Steel Institute, pp. 70-76 (January 1969); also J. Nucl. Mat. 29, pp. 103-110 (1969).

4. K. Farrell, J. T. Houston, A. Wolfenden, R. T. King, and A. Jostsons, in Radiation-Induced Voids in Metals, Proceedings of nal International Conference held at Albany, New York, June 9-11,1971.

5. E. E. Bloom, K. Farrell, M. H. Yoo and J. O. Stiegler, in E- ceedings of Consultant Symposium on the Physics of Irradiation-Produced Voids, AERE-R7934, p. 331.

6. R. C. Rau and R. L. Ladd, J. Nucl. Mat. 30, pp. 297-302 (1969).

7. D. E. Barry, Phil. Mag., p. 495 (19670)

8. R. Kossowsky, (Westinghouse R&D Center), and R. Bajaj, (Westing-house-Advanced Reactors Division), Pittsburgh, PA, unpublished work.

9. H. J. Beattie, Jr., Acta Cryst., 11, p. 607 (1958).

10. K. Farrell, Oak Ridge National Laboratory, private communication.

11. R. L. Simons, "Helium Production in FBR Out-of-Core Structural Components," HEDL-SA-1439, to be published in the Proceedings of the 9th International Symposium on Effects of Radiation on Struc-tural Materials (July 1978) Richland, Washington.

12. W. G. Wolfer, "A Short Review of Stress Effects on Swelling," in Proceedings of Workshop on Correlation of Neutron and Charged Particle Damage, CONF-760673, Oak Ridge, TN, June 1976, pp. 369-376.

VI. FUTURE WORK

No further work is planned at this time.

TABLE 1

ENHANCED VOID FORMATION ABOUT M_3B_2 PRECIPITATES IN VARIOUS SPECIMENS IRRADIATED IN EBR-II

Irradiation Temperature (°C)	Fluence+ (dpa)	Bulk Density Change (-%)	M_3B_2 Particle Diameter (nm)	Void Swelling (%)		Void Density (10^{14}cm^{-3})		Mean Void Size (nm)		Background Helium Level (appm)	Average Deposited Helium in Halo (appm)
				Matrix	Void Shells	Matrix	Void Shells	Matrix	Void Shells		
400	2.2 (11.2)	-0.03	350	0.17	0.23(Li)	4	16	21	16	9	13
			440		0.22*		12*	14*			14.5
					0.17**(Li)		11*	16*			14.5
430	2.8 (14.3	-0 Z3	720	0 08≤	0.21*	2	9*	21	18*	11	33
					0.22**(Li)		9**		18**		33
			730		0.30*		13*		16*		34
					0.24**(Li)		12**		16**		34
430	7.0 (35.7)	1.41	Unknown 800 est.	0.77	1.7 (Li)	3	19	35	25	Z8	87
					2.8 (He)		10		35		

+ (10^{22} n/cm^2, E>0.1 MeV)

*Inner shell region, **Outer shell region } where the shell was divided into two concentric zones

TABLE 2

CROSS SECTIONS AND FLUXES FOR FAST AND THERMAL REACTORS

Spectrum	Mean Neutron Energy $\bar{E}$ (MeV)	Spectral-Averaged Cross Sections (barns)					
		SS Displacements	SS Composite (n,α)	^{58}Ni (n,γ)	^{59}Ni (n,γ)	^{59}Ni (n,α)	^{10}B (n,α)
HFIR/PTP	0.42	192.0	1.7×10^{-4}	1.6	35.0	5.4	1.3×10^{3}
EBR-II Core	0.81	417.0	2.0×10^{-4}	3.2×10^{-3}	0.043	0.0078	1.0
EBR-II Blanket	0.22	162.0	1.2×10^{-5}	2.0×10^{-2}	2.4	0.43	8.4
FTR Gridplate	0.036	40.9	3.1×10^{-9}	9.1×10^{-2}	11.0	2.0	6.8×10^{1}
FTR Vessel	0.0022	4.31	3.2×10^{-11}	3.2×10^{-1}	18.0	3.0	2.7×10^{2}
PWR Core Barrel	0.080	80.0	1.1×10^{-8}	5.2×10^{-2}	6.5	1.2	3.3×10^{1}

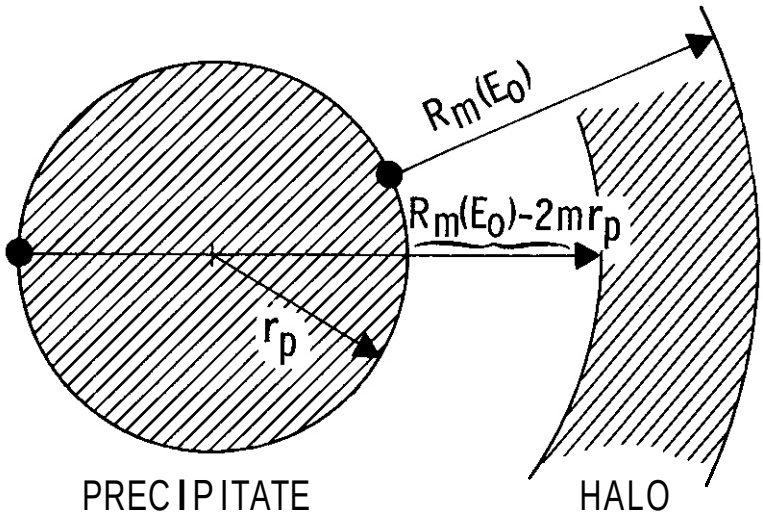

HEDL 7812-246.3

FIGURE 1. The Limits of the Halo are Determined by (n,α) Events Occurring on the Nearest and Farthest Surfaces of the Precipitate.

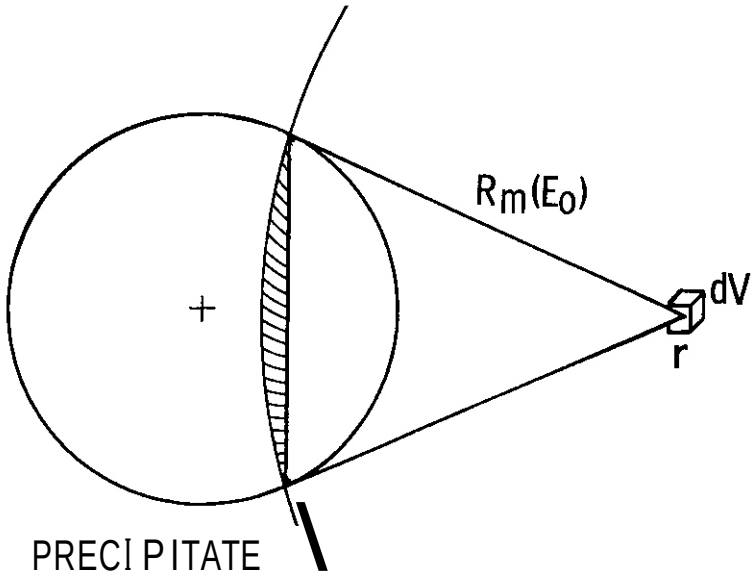

HEDL 7812-246.4

FIGURE 2. Definition of the (n,α) Source Plane Supplying Particles To a Unit Volume Located at Distance r From the Precipitate Center.

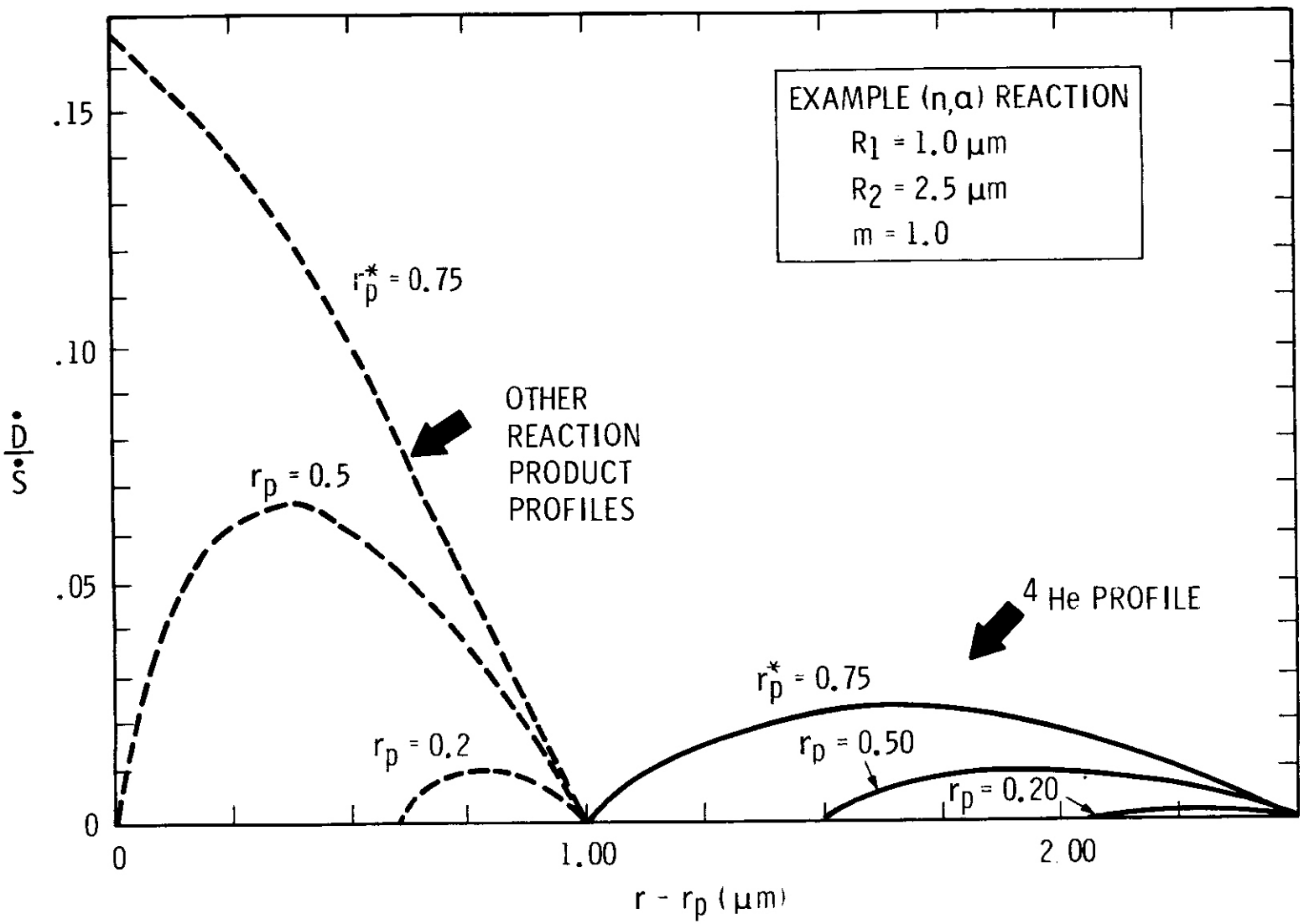

FIGURE 3. Example of Implantation Profiles for (n,α) Reaction Products

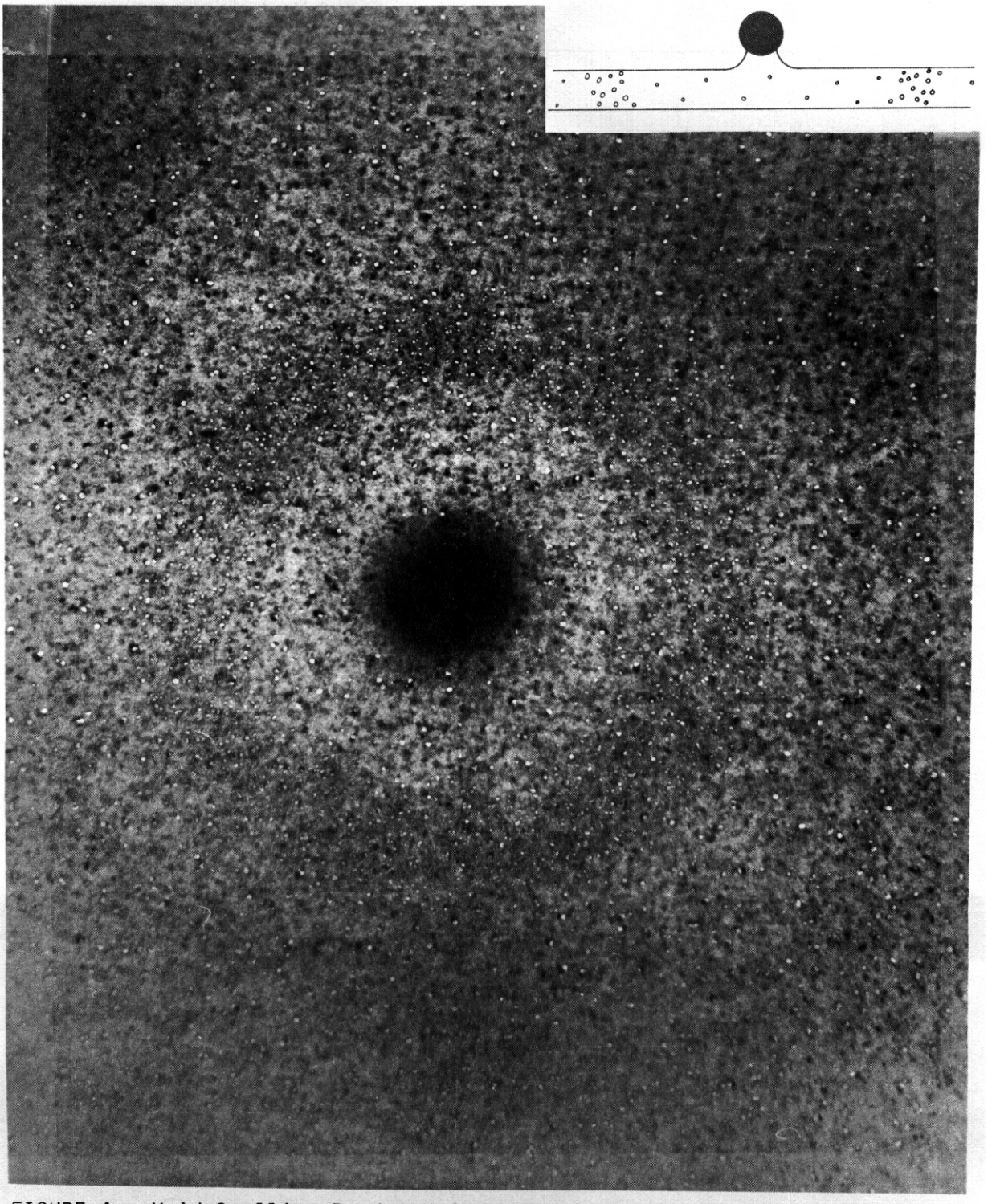

FIGURE 4. Void Swelling Produced in an Experimental Alloy With 2.0 x 10^{22} n/cm^2(E>0.1 MeV) and 400°C, Showing an Enhancement of Void Density in the Lithium Halo Produced by the M_3B_2 Precipitate. Stereomicroscopy Showed That the Precipitate Lies **Above** the Foil Section as Shown in the Inset.

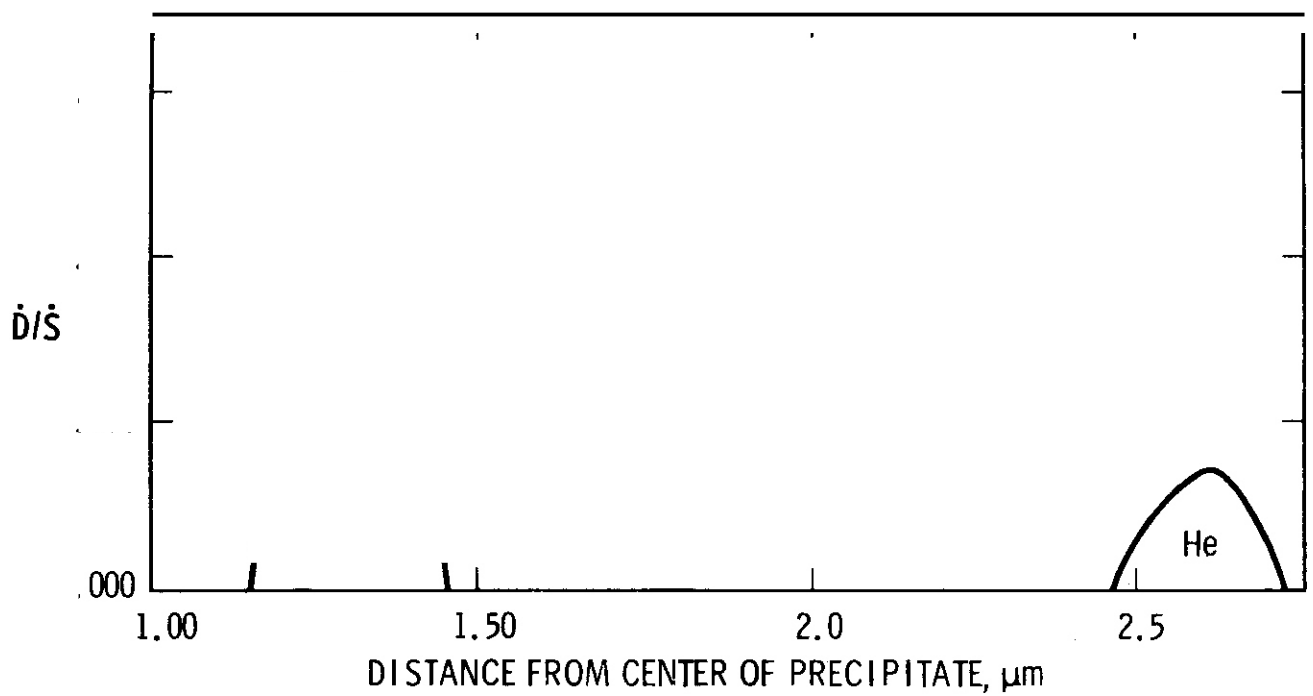

FIGURE 5. Normalized Deposition Rate of ^{7}Li and ^{4}He Atoms Formed About the M_3B_2 Precipitate Shown in Figure 4.

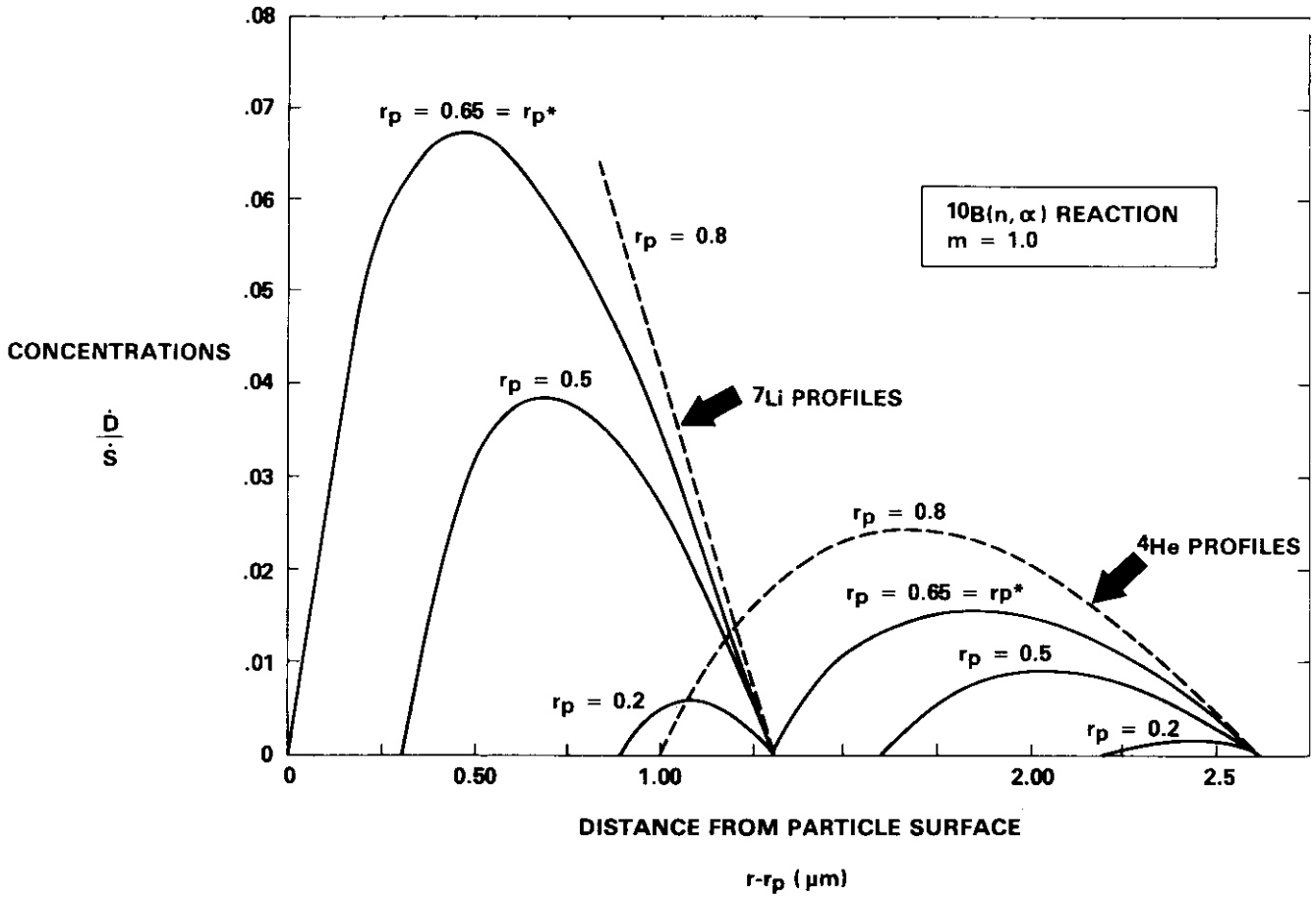

FIGURE 5 Reaction Product Profiles Deposited by the $^{10}B(n,\alpha)$ Reaction by Precipitates of Varying Radius.

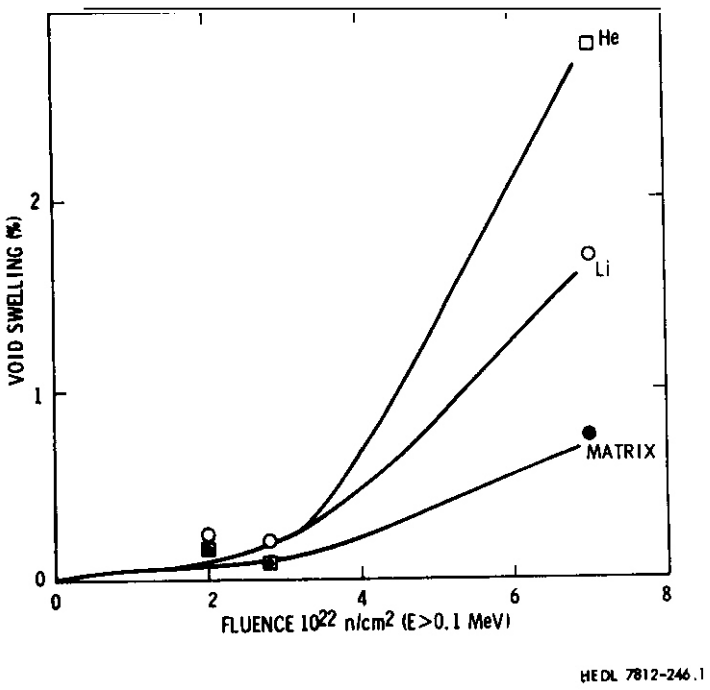

FIGURE 7. The Enhancement of Swelling at 400–430°C by Lithium and Helium Atoms Deposited in Halo's Surrounding M_3B_2 Precipitates.

I. PROGRAM

Title: Mechanical Properties
Principal Investigator: R. H. Jones
Affiliation: Battelle-Pacific Northwest Laboratory

II. OBJECTIVE

The displacement damage induced in Materials Research Corporation Marz grade nickel and niobium and reactor grade 316 SS by T(d,n) and Be(d,n) neutrons and 16 MeV protons is being correlated on the basis of cluster size and density and yield strength. The relationship between the radiation induced microstructure and flow properties is also being studied. Irradiation damage studies of path B and C alloys are planned.

III. RELEVANT DAFS PROGRAM PLAN TASK/SUBTASK

SUBTASK II.C.5 Effects of Cycling on Microstructure
SUBTASK II.C.11 Effects of Cascades and Flux on Flow
SUBTASK II.C.12 Effects of Cycling on Flow and Fracture

IV. SUMMARY

The cluster diameters and density and yield stress increase of T(d,n) and Be(d,n) neutron irradiated nickel and niobium have been measured. The cluster density and yield stress increase for T(d,n) and Be(d,n) neutron irradiated nickel were very comparable on a damage energy basis while the yield stress increase of niobium was not. The Be(d,n) neutron irradiated material had a plateau in the hardening response in the range of 0.002 to approximately 0.006 eV/atom. The T(d,n) neutron data was insufficient to show the plateau; however, at 0.006 eV/atom the yield stress increase of T(d,n) neutron irradiated niobium was 1.5 times that of Be(d,n) neutron irradiated niobium.

V. ACCOMPLISHMENTS AND STATUS

Radial activity and flux maps are compared to the radial yield stress increase for Be(d,n) neutron irradiated niobium in Fig. 1. As can be seen, the ^{58}Ni (n,p) activity rates are cylindrically symmetric about the beam axis and the gradient is quite steep, the activity dropping a factor of two in about 3.5 mm. The yield stress map was determined from the properties of individual wire specimens which were located relative to the beam axis by a densitometer profile of an autoradiograph. Because of the specimen to specimen scatter radial yield stress maps are shown for two irradiations which were positioned similarly relative to the target.

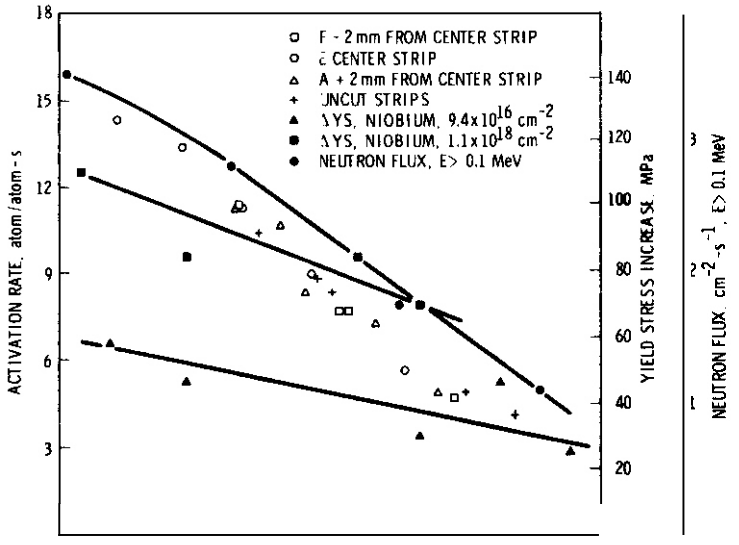

FIGURE 1. Radial activity, flux and yield stress maps for Be(d,n), E_d = 40 MeV.

The activity and flux gradients are very similar while the yield stress gradient is considerably less. This smaller slope is a result of the damage being averaged over the 5 mm gauge length of the wire specimen.

The microstructural changes and yield stress increase induced by T(d,n) and Be(d,n) neutron irradiations of nickel and niobium are compared in Figures 2 and 3.

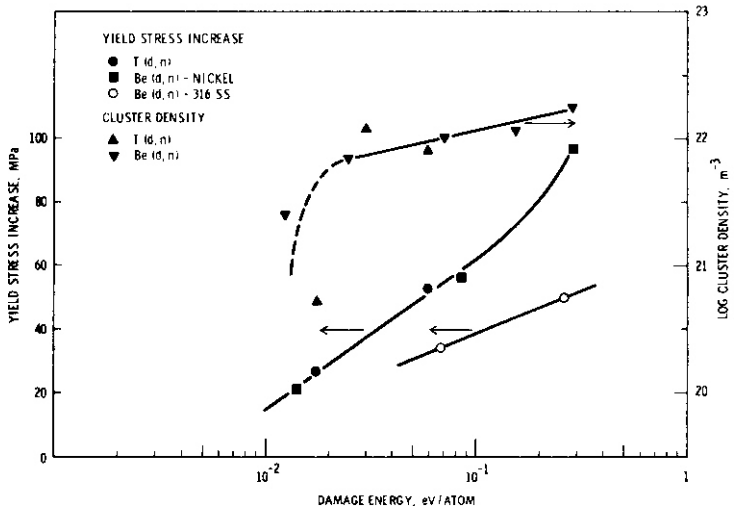

FIGURE 2. Yield stress increase and cluster density versus damage energy for T(d,n) and Be(d,n) neutron irradiated nickel and 316 SS.

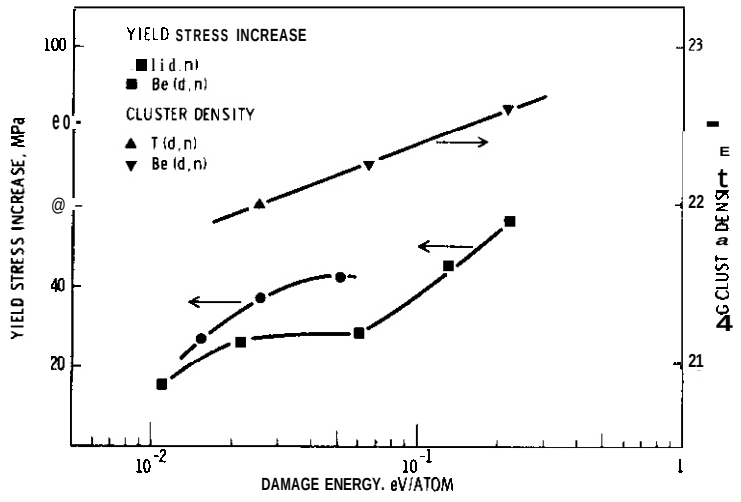

FIGURE 3. Yield stress increase and cluster density versus damage energy for T(d,n) and Be(d,n) neutron irradiated niobium.

The defect density in the irradiated nickel specimens increases with increasing fluence for both neutron sources. For fluence levels above 6×10^{16} cm^{-2} (0.02 eV/atom), there are no significant differences in the total defect densities between specimens irradiated with T(d,n) or Be(d,n) neutrons, while the yield stress increase was similar over the entire fluence range evaluated.

The cluster density in T(d,n) and Be(d,n) neutron irradiated niobium was also similar; however, there is less data on which to base this conclusion.

The yield stress increase of niobium was sensitive to the neutron spectrum as shown in Fig. 3. The hardening response of Be(d,n) neutron irradiated niobium has a plateau over the fluence range of 1-3 x 10^{17} cm^{-2} (.022 - 0.066 eV/atom) while the T(d,n) neutron data was insufficient to clearly show a plateau. The difference in the T(d,n) and Be(d,n) neutron yield stress increase curves appears to be related to a plateau in the hardening response with increasing damage energy/atom while the damage energy thresholds for hardening are equal. Plateau's in the hardening response of niobium have been observed for Be(d,n) neutron irradiated niobium by Mitchell et al. [1] and in fission neutron irradiated niobium single crystals by Loomis and Gerber [2].

The yield stress increase results for Be(d,n) neutron irradiated niobium could be described by stage I, III and IV of Loomis and Gerber [2] while that of T(d,n) neutron irradiated niobium as stage I and early stage 111. The significant difference therefore between the T(d,n) and Be(d,n) results is primarily the greater hardening induced in stage I by T(d,n) neutrons. There is insufficient data to compare the transitions from stage I to III and III to IV. Based on Loomis and Gerbers conclusion that stage I hardening is due primarily to impurity atom - point defect complexes, the T(d,n) neutrons induce a greater concentration of defect complexes than the Be(d,n) neutrons at equal damage energies.

The effect of T(d,n) and Be(d,n) neutrons on the ultimate tensile strength and total elongation of nickel are quite similar as shown in Table 1. The ultimate tensile strength was independent of irradiation type and fluence while the total elongation decreased with increasing fluence.

TABLE 1

SUMMARY OF THE TENSILE PROPERTIES OF T(d,n) AND Be(d,n) NEUTRON IRRADIATED NICKEL, NIOBIUM AND 316 STAINLESS STEEL

		NICKEL				316 STAINLESS STEEL				NIOBIUM			
												ELONGATION, %	
IRRADIATION	FLUENCE cm^{-2}	0.2 YS MPa	Ideal 1% MPa	UTS MPa	EL %	0.2 YS MPa	Ideal 1% MPa	UTS MPa	EL %	LYP MPa	UTS MPa	NON-UNIFORM	TOTAL
AS ANNEALED	0	65	2400	305	26	307	4020	525	27	131	161	2.7	10
T(d,n)	6×10^{16}	105	2200	339	33	-	-	-	-	158	160	4.9	13
	1×10^{17}	-	2600	335	20		-	-	-	168	174		12
	2×10^{17}	118	2400	308	16		-	-	-	173	-	-	3.8
Be(d,n)	5×10^{16}	86	2600	318	24					146	155	1.6	11
	1×10^{17}									157	166	2.4	13
	3×10^{17}	121	2500	308	23	341	3310	570	23	159	160	1.4	10
	6×10^{17}									176	175		8
	1×10^{18}	162	2500	305	13	357	2020	503	20	187	-	-	3.6

Serrated yielding was observed in specimens irradiated to 0.3 and 1×10^{18} cm^{-2} with Be(d,n) neutrons. The average load drop and plastic strain range over which the serrated yielding occurred increased with increasing fluence. At a fluence of 10^{18} cm^{-2} the average load drop corresponded to a stress change of 14 MPa while it persisted to a strain of 0.008 while at a fluence of 3x1017 cm^{-2} these parameters were 8 MPa and 0.005, respectively.

Type 316 stainless steel showed less response to Be(d,n) neutron irradiation than the high purity nickel as shown in Fig. 2. This data suggests that the onset of irradiation induced hardening occurs at about the same fluence in both materials but that the response with fluence is less in 316 SS. At a fluence of 10^{18} cm^{-2} (.26 eV/atom), the 316 SS has 1/2 the yield strength increase of the high purity nickel.

The effect of irradiation on the work hardening rate of nickel and 316 SS differed in that the work hardening rate in nickel was unaffected by neutron irradiation while that of 316 SS was reduced by a factor of 2. Both the ultimate tensile strength and total elongation of 316 SS responded to neutron irradiation in a similar manner as the nickel.

The ultimate tensile strength of niobium was not altered by irradiation; however, the total elongation was. At a fluence of 2×10^{17} cm^{-2} T(d,n) neutrons and 1×10^{18} cm^{-2} Be(d,n) neutrons the total elongation was approximately equal to that of discontinuous flow in the unirradiated specimens. When this occurred, the work hardening rate was equal to or less than zero and the yield strength equaled the ultimate tensile strength.

VI. REFERENCES

1. J. B. Mitchell, "Exploratory Experiments Comparing Damage Effects of High-Energy Neutrons and Fission-Reactor Neutrons in Metals," Lawrence Livermore Laboratory Report, UCRL-52388.

2. B. A. Loomis and S. B. Gerber, Acta Met., 21 (1973), 165.

VII. FUTURE WORK

Two specimen packets containing nickel 316 SS and niobium wire tensile specimens (14 of each) and nickel, 316 SS, niobium and vanadium foils were delivered to LLL for 14 MeV neutron irradiations with RTNS II. The goal fluences are 2 and 6×10^{17} cm^{-2} at 25°C. These irradiations will be completed and the packets disassembled during the next quarter.

VIII. PUBLICATIONS

A paper entitled "Experimental Radiation Damage Studies in 16 MeV Proton Irradiated Nickel and Niobium" by D.L. Styris, R.H. Jones and E.R. Bradley was submitted for publication in the proceedings of the Fifth Conference on Application of Small Accelerators which was held on Nov. 6-8, 1978 at North Texas State University.

I. PROGRAM

Title: Effects of Near Surface Damage and Helium on the Performance of the First Wall

Principal Investigator: O. K. Harling

Affiliation: Nuclear Reactor Laboratory, Massachusetts Institute of Technology

11. OBJECTIVE

The objective of this study is to understand and quantify the effects of near surface damage and implanted gas on the performance of the fusion reactor first wall.

III. RELEVANT DAFS PROGRAM TASK/SUBTASK

TASK	II.C.5	Effects of Cycling on Microstructure
	II.C.8	Effects of Helium and Displacement on Fracture
	II.C.12	Effects of Cycling on Flow and Fracture
	II.C.13	Effects of Helium and Displacement on Crack Initiation and Propagation
	II.C.15	Effects of Near Surface Damage on Fatigue

IV. SUMMARY

Installation, testing and compliance with the safety requirements of MITR-II of the in reactor fatigue cracking experiment has been completed. The methods for machining welding and polishing the samples have been developed and the sample design is completed. An apparatus for the production of pressurized capsules with Helium-Argon mixtures has been completed. A fully prepared sample, gas filled and sealed under pressure should begin irradiation testing in the MITR-II reactor early in the next quarter.

V. ACCOMPLISHMENTS AND STATUS -- H. Andresen (MIT/Hahn-Meitner Inst.) and O. Harling (MIT)

A. In-Reactor Fatigue-Creep Experiment

The aim of the experiment is to determine the influence of a heavily damaged and helium implanted surface layer on the fatigue life of stainless steel bulk material which is simultaneously irradiation hardened and subject to cyclic stresses. The conditions will be chosen to fit as closely as possible those expected in later fusion reactors.

In order to achieve this goal, thin-walled sample capsules pressurized with up to 100 atm of a helium/argon mixture will be irradiated in the reactor core. The thin part of the capsules will be bombarded with fast α-particles which originate in the reaction of thermal neutrons with a B-10-coated foil positioned around the pressurized capsule.

By means of sample temperature cycling (approximately every 5 minutes) in the region 350 - 550^{O}C and the resulting pressure cycling in the capsules, the samples will be cycled through their fatigue life. The sample failure will he detected by the radioactive isotope A-41.

Fig. 1 shows schematically the experimental setup for temperature cycling of the samples in the core. Essentially the temperature is cycled by changing the heat transport of the helium gas in the thimble while the y-heat generation in the reactor core is constant for the sample unit. The heat transport by the helium is cycled by drastically increasing or decreasing the helium pressure.

The sample temperature can be controlled at the upper cycle temperature ($\sim$540^{O}C) by pulsed insertions of small amounts of helium via the thermocouple-activated control solenoid in the line from

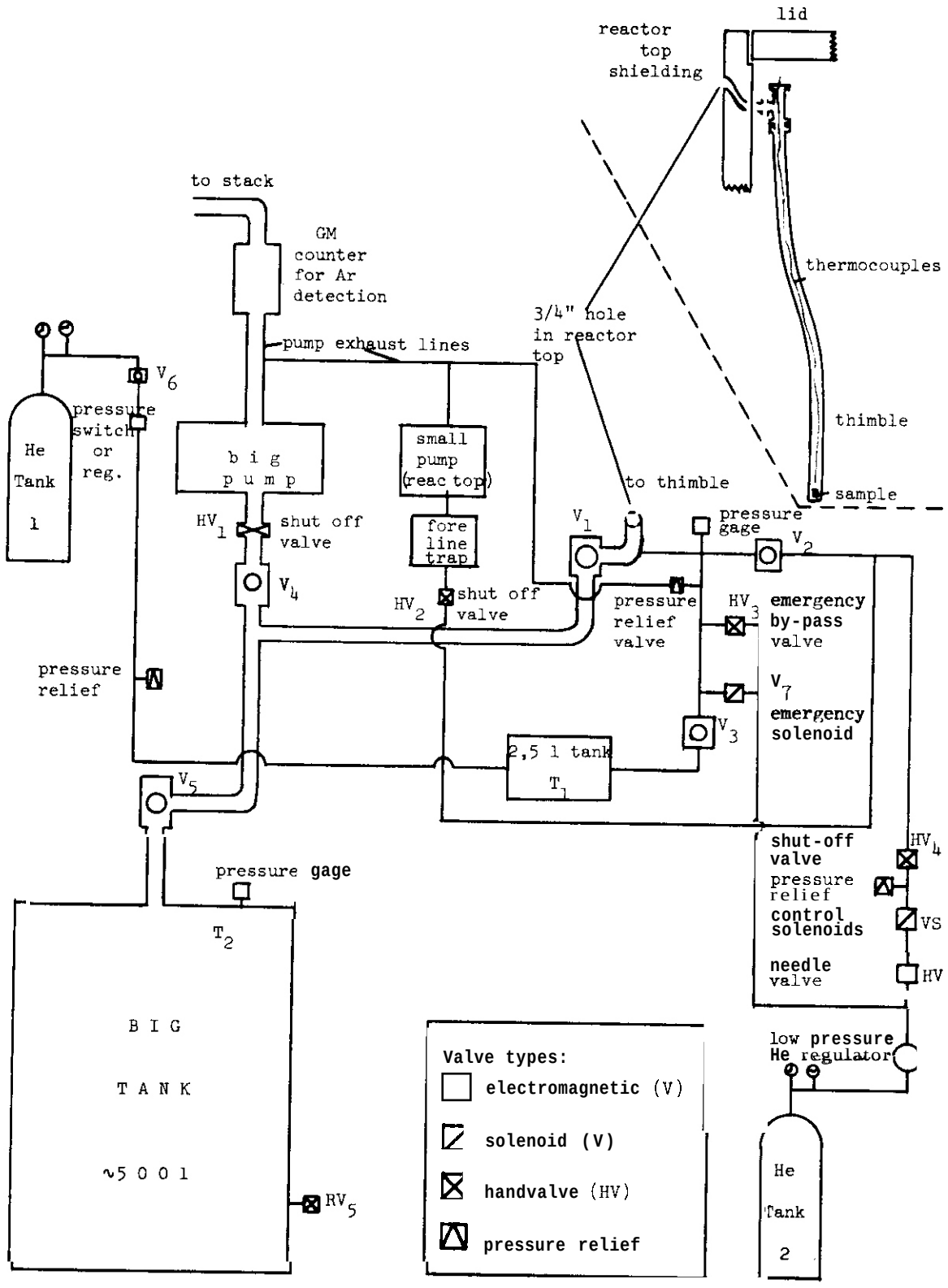

FIGURE 1. Schematic of In-Reactor Fatigue Cracking Experiment.

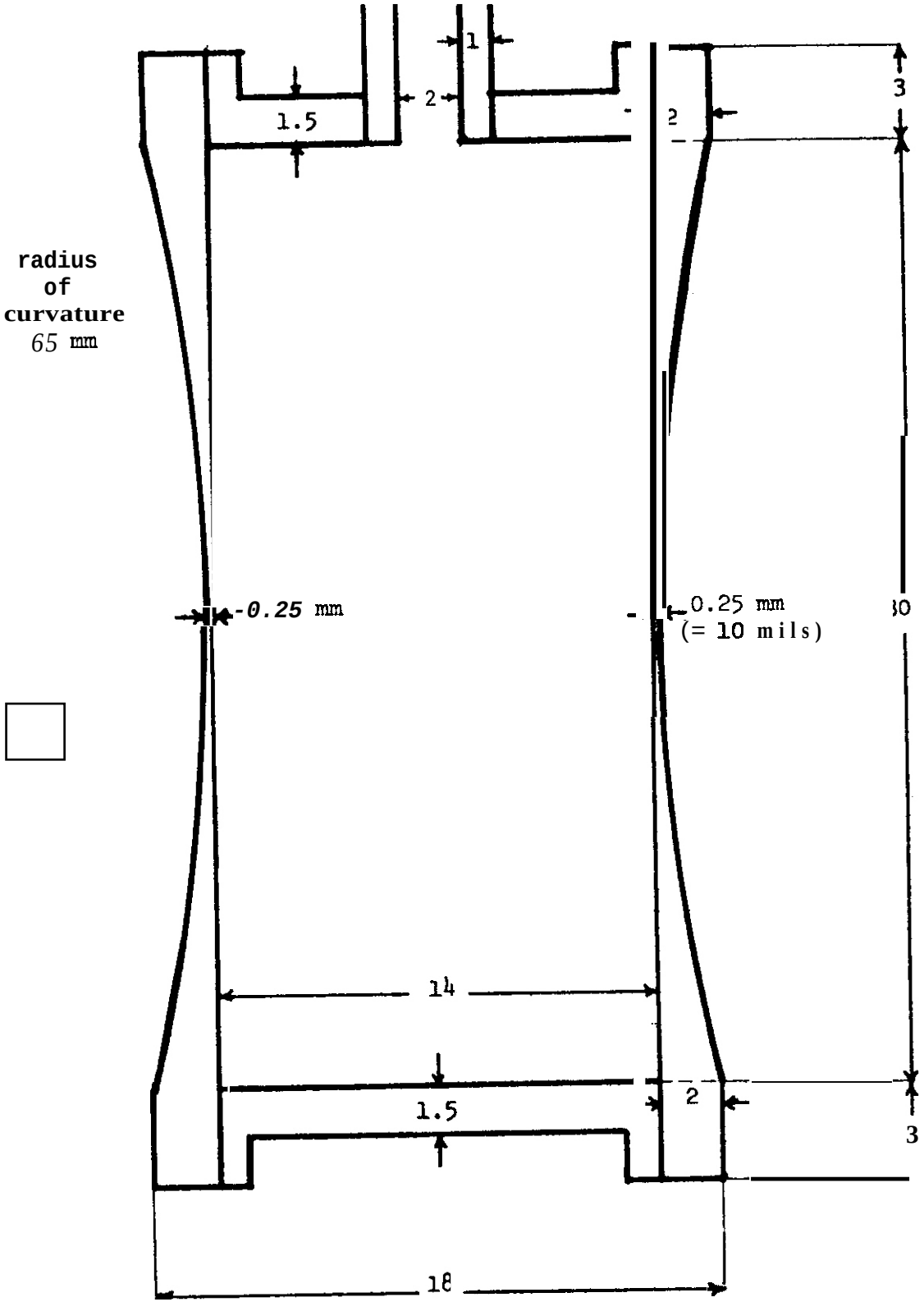

FIGURE 2. **Sample Capsule.**

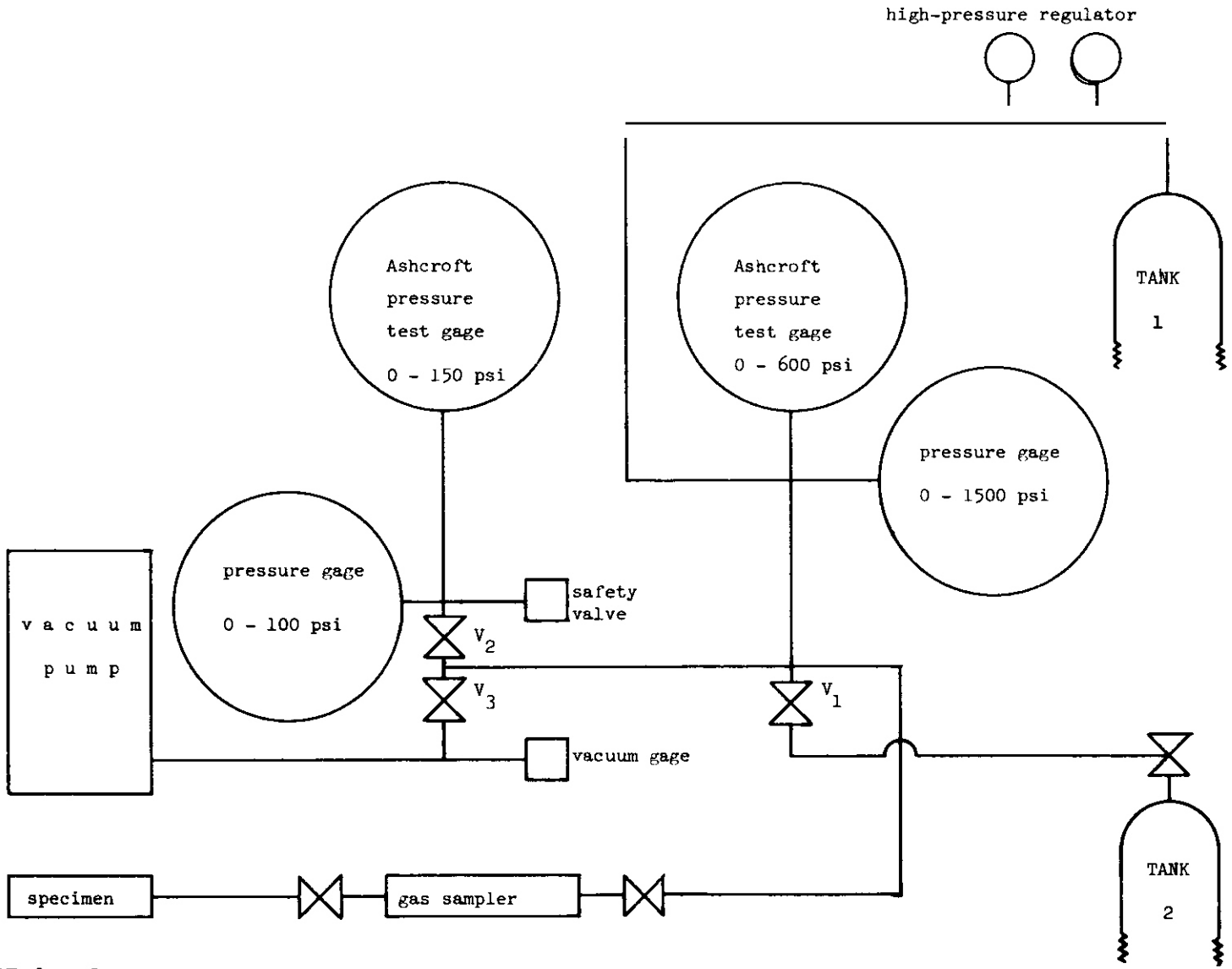

FIGURE 3. System for Preparation of Helium-Argon Mixtures and for Filling the Specimen Capsules.

helium tank 2 (look at right hand side of Fig. 1), while a small pump is continuously pumping on the irradiation thimble. Cycling can be initiated by closing V_2 and opening V_3 which leads to fast flooding of the irradiation thimble with helium of about 1 atm pressure. As a result, the sample temperature drops rapidly to the lower sample temperature ($\sim 350^{\circ}C$) due to the drastically increased helium pressure. At the lower cycle temparature V_3 is closed, V_1 and V_5 opened. This results in rapid expansion of the helium from the thimble into the big tank T_2 and the subsequent opening of V_4 reduces the pressure in the thimble into the low micron range. In turn the sample temperature rises to the upper control temperature where after opening V_2 the initially mentioned pulsed helium insertions keep the temperature constant for the desired time, while the big pump operates on the big tank $T_{2'}$ The cycle can be repeated approximately every 5 minutes.

The samples, which will be used in the experiments are shown in Fig. 2. They are machined, welded and polished with special care. Details on the thermomechanical design will be given in a future quarterly report. Pressurization of the capsules is done in the apparatus shown in Fig. 3. After pressurization the thin filling tube is squeezed in a press in order to achieve a cold weld and is finally hot welded.

VI. REFERENCES

None

VII. FUTURE WORK

In reactor testing is expected to begin in the next quarter.

I. PROGRAM

Title: Irradiation Effects Analysis (WH011/EDA)
Principle Investigator: D. G. Doran
Affiliation: Hanford Engineering Development Laboratory

II. OBJECTIVE

The objective of this work is to assess the effects of cyclic variations in irradiation, stress and temperature on the evolution of the damage microstructure to enable the projection of steady-state irradiation data to cyclic conditions.

III. RELEVANT DAFS PROGRAM TASK/SUBTASK

II.C.5 Effects of Cycling on Microstructure

IV. SUMMARY

The effect of pulsed electron irradiation on microstructure evolution was studied in a simple Fe-Ni-Cr alloy and the results compared with a theoretical model. Pulse periods of 2.5 to 60 seconds (duty factor near 50%) at 600°C significantly reduced the maximum swelling rate compared to continuous irradiation. The short period end of the critical pulsing regime is believed to be determined by the time required to achieve sufficient decay of the vacancy concentration during beam-off; the long period end of the regime is attributed to the relaxation times for void embryo decay and build-up. The void concentration was observed to increase and void size to decrease for the pulsed cases compared to the steady irradiation. Projection to a displacement rate and temperature typical of expected tokamak operation indicates that these machines may operate in the critical pulsing regime.

V. ACCOMPLISHMENTS AND STATUS

A. The Effect of Pulsed HVEM Irradiation on Microstructure Evolution in a Simple Fe-Ni-Cr Alloy - R. W. Powell (HEDL) and G. R. Odette (UC-SB)

1. Introduction

Unlike fission reactors, fusion reactors are likely to operate in a pulsed mode,[1] leading to cyclic variations in temperature, stress and radiation damage rates at the first wall. Such effects are not easily simulated in fission reactors, where most first wall materials studies will be conducted. Nonetheless, the extent and impact of these effects on materials behavior must be understood in order to project the large body of fission reactor data to fusion reactor conditions. The importance of the developing microstructure in determining key mechanical properties of reactor components indicates that an understanding of the effect of pulsed operation on microstructure evolution is basic. The initial phase of this study was directed at the effect of pulsed radiation damage rates on microstructure evolution.

Cyclic variation of the displacement rate can be categorized into three basic regions relative to the lifetimes of the point defects: (1) the pulse duration is short compared to the lifetimes of both vacancies and interstitials, (2) the pulse duration is short relative to the lifetime of vacancies but long relative to the lifetimes of interstitials, and (3) the pulse duration is long relative to the lifetimes of both defect types. Previous experimental studies[2,3] have been performed in region (2) while theoretical treatments have addressed various aspects of all three regions.[4-6]

The current study is being conducted primarily in region (3), where tokamaks and mirrors would be expected to operate.[1] The effects on void formation of a range of pulse periods and duty factors is studied with electron irradiations and compared with theoretical calculations.

2. Results

Analysis of the experimental results on microstructure evolution during pulsed irradiation requires the application of a comprehensive computer model. The interrelationship between dislocation loops, network dislocations and voids was treated previously for steady-state irradiation conditions.[7] This model calculated the nucleation of defect aggregates as well as the growth of the aggregates, allowing the nucleation rates to decline as dictated by the ever increasing point defect sink strengths. Thus, nucleation rates were transformed into observable defect agglomerate concentrations by accounting for the time period of significant nucleation. A typical plot of the calculated fluence dependence of the various microstructural entities is shown in Figure 1 for steady-state conditions.

Also treated previously was the effect of pulsed irradiation on the nucleation of voids.[6] This detailed treatment calculated the decrease in the void nucleation rate for pulsed conditions compared to the steady-state void nucleation rate. One of the primary results of that study was the development of a quasi-empirical relationship between the throttling (reduction) of the nucleation rate and the pulse-on and pulse-off times. This correlation was found when the pulsing conditions were normalized to the relaxation times for void nuclei build-up and decay. By using this relationship, it was possible to predict the throttling of the void nucleation rate for given pulsing parameters (relative to the appropriate relaxation times) without going through the full multi-state kinetic phenomena calculation

For the present study, the microstructure evolution model was modified to accept pulsed irradiation conditions, and the correlation for the nucleation rate throttling was incorporated into the void nucleation calculation routine. Additionally, the model treated void and dislocation loop growth effects by also calculating growth rates during beam-off conditions. In this manner the effect of pulsed radiation on the void nucleation and growth rates was accounted for in the overall model for

microstructure evolution and its effect on the observable microstructure was calculated.

Figure 2 illustrates the calculated microstructural evolution for pulsed irradiation conditions. Comparison with the calculated evolution for steady-state irradiation conditions shown in Figure 1 illustrates the significant effect pulsed irradiation is expected to have on the damage microstructure. The initial void nucleation rate is depressed many orders of magnitude by the pulsed radiation conditions chosen for Figure 2. However, as the microstructure evolves, the throttling of the nucleation rate declines and then increases resulting in less than an order of magnitude reduction in the eventual void concentration. The approach to steady-state swelling conditions (constant swelling rate typified by a constant void concentration and indicative of the time of significant nucleation) is more abrupt for the pulsed irradiation due to this minimum in the nucleation rate throttling and corresponding "burst" of void nucleation. The development of the dislocation structure is also retarded, illustrating the strong interaction between the voids and dislocations. The system bias for dislocations is reduced by the large reduction in neutral sinks (voids), thereby leading to lower interstitial loop nucleation and growth rates (overall growth rate is best measured by the total dislocation line length.

The range of application of the combined model is determined by the simplifying assumptions made in its development. Point defect concentrations were assumed to react instantaneously to changes in the displacement rate. This means that the pulse times must be long compared to the time to achieve steady-state point defect concentrations. For pulse times significantly shorter than this, the vacancy concentration will oscillate about some average value and the equations describing void nucleation rates and embryo decay times will not be valid (the actual time variation of the defect concentrations can be used in the development but were not used in the present study). However, under such conditions the effect of pulsed irradiation is expected to be quite different since little embryo

decay will occur during beam-off due to the decreased net vacancy emission rate. This fact can be used as an additional calibration of the model parameters since the change in microstructural response should be experimentally observable.

This theoretical model is being used to guide the experimental work of this study and to aid the interpretation of the experimental results. Conversely, the experiments are used to test the validity of the model and as a tool to calibrate the model parameters.

3. Experimental Procedures

A simple Fe-Ni-Cr alloy, designed E20, of nominal composition 15 wt.% Cr and 25 wt.% Ni, was used throughout this portion of the study. This simple alloy was chosen to eliminate as many variables as possible and still maintain a strong tie to technological materials of direct interest to the U. S. Fusion Materials Program.

Electron irradiations were performed at 1 MeV in a JEOL JEM-1000 using a double tilting goniometer heating state. Pulsing of the electron beam was accomplished by deflection with two pairs of electrostatic deflector plates alternately charged and discharged with square wave voltage pulse generators. Rise and fall times of the voltage pulse were less than 1 msec and stability of the electron beam positioning was excellent.

An irradiation temperature of 600°C (including heating due to the electron beam) was used for all irradiations. Peak displacement rate for all pulsed and steady-state irradiations was 1.3 x 10^{-3} dpa/sec (40 barn cross section). Thus, assuming that the time during the beam-on condition was sufficient to achieve quasi-steady-state defect concentrations, there was no effective temperature shift due to differences in displacement rates[9] among any of the irradiations. A typical total dose of 4 dpa was employed which correspond to 1 hour of steady irradiation or approximately 2 hours of pulsed irradiation.

The temperature rise due to the electron beam for the conditions employed was less than 10°C as measured by the order-disorder transition in Fe_3Al. This small temperature rise was the result of employing a relatively small displacement rate in order to minimize the influence of temperature pulses on the results.

Various pulsing parameters were studied to determine the pulsing conditions employed ranged from 2.5 seconds to 60 seconds pulse periods with 0.40 to 0.60 duty factors, as will be described in Section 3, they span the region of interest for the irradiation temperature of 600°C.

4. Results

As anticipated, microstructure evolution was not significantly affected by the shortest pulse period but significant effects were observed for all the longer pulse period irradiations. This is best illustrated in Figure 3 where the dose dependence of swelling is plotted for the continuous irradiation (E637), the shortest period pulsed irradiation (E638) and the irradiation (E640) for which the effect was largest. It is clear from the figure that pulsing the radiation has a significant effect on both the magnitude and the approach to the maximum swelling rate. Even the irradiation with the shortest period achieved a steady-state swelling condition more rapidly than the steady irradiation.

Pulsing had a signficant effect on both the void concentration and the average void size. Table 1 illustrates that these effects were opposite in sign; all pulsing conditions produced roughly a factor of three higher void concentration but a significantly smaller void size compared to the steady irradiation. The variation in void size was dependent on the pulse period.

The major variable in the work to date was the pulse period; the effect of this parameter an the maximum swelling rate is shown in Figure 4. (The "steady" irradiation is shown as pulsed because the irradiation

was stopped at 1000 second intervals to obtain micrographs.) The swelling rate decreases as the pulse period is increased from 2.5 seconds to 60 seconds. It increases again to reach the essentially steady irradiation value. Although only small variations in the duty factor were employed in this investigation, its effect on the swelling rate is evident in Figure 4. Irradiation E639B had a duty factor of 0.4 compared with 0.60 for irradiation E639A; both had the same pulse period.

The transition from ineffective to effective pulse periods is also illustrated in Figure 4. At the one extreme, a reduction in the pulse period to 2.5 seconds with a 60% duty factor resulted in an increase in the maximum swelling rate at a peak flox 1.3×10^{-3} dpa/sec at 600°C. At the other extreme, pulse periods significantly longer than 60 seconds are expected to be necessary to eliminate the effect for the conditions employed. The extreme pulse periods correspond to fluences during a single pulse of 0.002 dpa and 0.04 dpa, respectively.

5. Discussion

The major experimental result is that pulsing the HVEM irradiations produced a significant decrease in maximum swelling rate. The maximum void concentration was measurably increased and the void size at a given fluence was measurably reduced in the pulsed environment compared to the continuous, control irradiation. The effective pulsing regime is bounded at one end by short pulse periods in the neighborhood of 2.5 seconds and on the other end by pulse periods significantly longer than 60 seconds. Within this region, quantitative details of the pulsing effect depend on the pulsing parameters. Each of these observations will be considered in this section in light of the model developed in Section 2 and for projection *to* other irradiation conditions.

The decreased effectiveness as the irradiation pulse period is reduced toward 2.5 seconds is not predicted directly from the model of Section 2 because of the simplifying assumption of square wave defect

concentrations. It is possible to estimate the approximate region where this simplifying assumption no longer holds and the vacancy concentration remains significantly above the thermal equilibrium value throughout the pulse period. The time dependence of the vacancy concentration can be described by(9)

$$\frac{dc_v}{dt} = K' - \alpha c_i c_v - D_v c_v k_v^2 \qquad [1]$$

where c_v and c_i are the respective point defect concentration, α is the recombination parameter, K' is the vacancy generate rate (including vacancy emission from sinks), D_v is the vacancy diffusivity and k_v^2 is the vacancy sink term. Considering the decay in the vacancy concentration when the radiation is off and neglecting recombination and thermal emission of vacancies, equation [1] can be integrated to

$$t = \frac{1}{D^v k^{v2}} \ln \frac{c_v}{c_v^{th}} \qquad [2]$$

Here, t is the beam-off time to reach the thermal equilibrium vacancy concentration, c_v^{th}, from the initial concentration of c_v.* The term k_v^2 depends on dislocation density, void concentration and size, grain size and free surface proximity. For no voids, a grain size of 0.6 μm (approximating the foil thickness) and dislocation density increasing from 1×10^9 to 1×10^{10} cm^{-2}, the decay time varies from 3 to 0.3 seconds for a vacancy migration energy of 1.5 eV. This value of the vacancy migration energy yields the observed short period cut-off (2.5 second pulse period with 1.0 seconds of beam-off) in the pulsing effect.

* If thermal emission were not neglected, mathematically t would be infinite. Practically speaking, we want the time required to reach a condition of net vacancy emission from voids, which this equation approximates.

The previous theoretical treatment of pulsing[6] established that pulsing should produce a significant reduction in the void nucleation rate. The experimental observation of an increased void concentration appears to contradict that condition. However, void nucleation rates cannot be directly transformed into concentrations since the time period of nucleation is not known. In addition, the significantly smaller void size observed for the pulsed case is not directly predictable from a decreased void nucleation rate. The microstructure evolution model was used to address these points.

It was noted in Section 2 that the microstructure evolution model predicts that void nucleation throttling caused by pulsing would result in essentially a burst of void nucleation. This is because the relaxation time for void embryo buildup decreases as the dislocation structure evolves and then increases again as the voids become a prominant sink and the vacancy concentration declines. Under such conditions the average void size is reduced as well. This is an important point and demonstrates the strong interrelationship among all the features of the microstructure. Whether the peak nucleation rate and subsequent void concentration are significantly reduced compared to the steady irradiation case depends on the pulsing parameters employed. Thus, a measurable reduction in average void size and an essentially unchanged void concentration would be consistent with the microstructure evolution model modified for a pulsing effect on void nucleation and growth.

The discrepancy between the magnitude of the observed effect on both the void concentration and the void size and that calculated by the model is believed to be due to the square wave approximation assumed for the point defect concentrations. When the irradiation is turned off, the interstitial concentration decays very rapidly, leaving only vacancies which can then nucleate voids. This would result in a significant increase in the void nucleation rate immediately following each irradiation pulse. On the other hand, at the beginning of each irradiation pulse (before steady state defect concentrations are achieved) the interstitial

concentration will approximately equal the vacancy concentration thereby enhancing the ratio of interstitial-to-vacancy arrival rates at sinks (voids and dislocations). However, this latter effect will not completely balance the enhanced void nucleation following each pulse because of the greater partitioning of the interstitials to dislocations rather than to voids. The overall effect is expected to be a slight increase in the void concentration and a corresponding reduction in the average void size.

Considering the length of transient in the defect concentrations and the magnitude of the void embryo buildup time, the sensitive pulsing regimes at other temperatures and fluxes can be predicted. Again, the short pulse period cut-off, t_s^c, is not currently treated by the model but this parameter should be dominated by the temperature dependence of $1/D_v$ (see equation [2]). Thus, t_s^c should decrease significantly with increasing temperature. On the other hand, model calculations indicate that, within certain limits, the relaxation time for buildup of void embryos is not strongly temperature dependent. The net result is an overall increase in the pulse period range to produce observable microstructural effects as the irradiation temperature is increased.

A reduction in flux to 5×10^{-7} dpa/sec and the temperature to 460°C (both are within anticipated ranges for tokamaks[**]) produces both an increase in t_s^c and in the long pulse period cut-off, t_ℓ^c. Under these conditions the increase in t_s^c is one to two orders of magnitude while t_ℓ^c is predicted to increase by two to three orders of magnitude. The corresponding sensitive pulsing regime at 450°C would then be pulse periods greater than 200 seconds and less than 10 sec (3 hours) with duty factors near 0.50. This is well within the anticipated range for tokamaks[**]) and has significan impact on developing a methodology to project steady-state fission reactor data to pulsed fusion reactor conditions.

6. Conclusions

This investigation has so far demonstrated the following major

points concerning pulsed HVEM irradiation of a simple Fe-Ni-Cr alloy at 600°C.

1. Within a critical pulsing regime, pulsed HVEM irradiation produced a significant decrease in swelling rate compared to continuous irradiation results.

2. The observed decrease in swelling rate was accompanied by an increase in void concentration and a decrease in void size.

3. The critical pulsing regime was between pulse periods of 2.5 seconds and approximately 60 seconds when the duty factor was 50%.

4. Analysis with a theoretical model of microstructure evolution indicated that the pulsing conditions employed affected the time of significant void nucleation. It also demonstrated that transients in the defect concentrations are important.

5. Projection to a displacement rate and temperature typical of fusion reactors indicates that tokamaks may operate in the critical pulsing regime.

VII. REFERENCES

1. G. L. Kulcinski, "Radiation Effects and Tritium Technology for Fusion Reactors," eds., J. S. Watson and F. W. Wiffen, DOE Report CONF-780989 (Oak Ridge, TN, 1976), p. 1-17.

2. A. Taylor, D. L. Potter, H. Wiedersich, J. R. Wallace, H. A. Hoff and D. G. Ryding, Argonne National Laboratory CTR Quarterly Report, p. 18, January - March 1975.

3. J. A. Sprague and F. A. Smidt, Jr., Naval Research Laboratory Semi-Annual Progress Report, p. 27, November 1972 - April 1973, NRL Memorandum Report 2629.

4. N. Ghoniem and G. L. Kulcinski, University of Wisconsin Report UWFDM-180, November 1976.

5. J. O. Schiffgens, N. J. Graves and D. G. Doran, "Radiation Effects and Tritium Technology for Fusion Reactors," eds., J. S. Watson and F. W. Wiffen, DOE Report CONF-750989 (Oak Ridge, TN, 1976), p. 1-532.

6. G. R. Odette and R. Myers, CTR Quarterly Report, Aprii - June 1975, HEDL-TME-75-90, p. 2.

7. R. W. Powell, Proceedings of International Conference: "Radiation Effects in Breeder Reactor Structural Materials," eds., M. L. Bleiberg and J. W. Bennett, (Scottsdale, AZ, 19771, p. 757.

8. K. C. Russell, Acta Met. 19, (1971) p. 753.

9. A. D. Brailsford and R. Bullough, J. Nucl. Mat. 44, (1972), p. 121.

VI. FUTURE WORK

Additional pulse periods and duty factors will be employed for the 600°C HVEM irradiations to more completely map out the effect of pulsing at this temperature. Approximations for the transients in the defect concentrations will be incorporated into the model to aid the analysis of the experimental results.

VIII. PUBLICATIONS

This information is to be presented at the First Topical Meeting on Fusion Reactor Materials, January 29-31, 1979, Miami Beach, Florida.

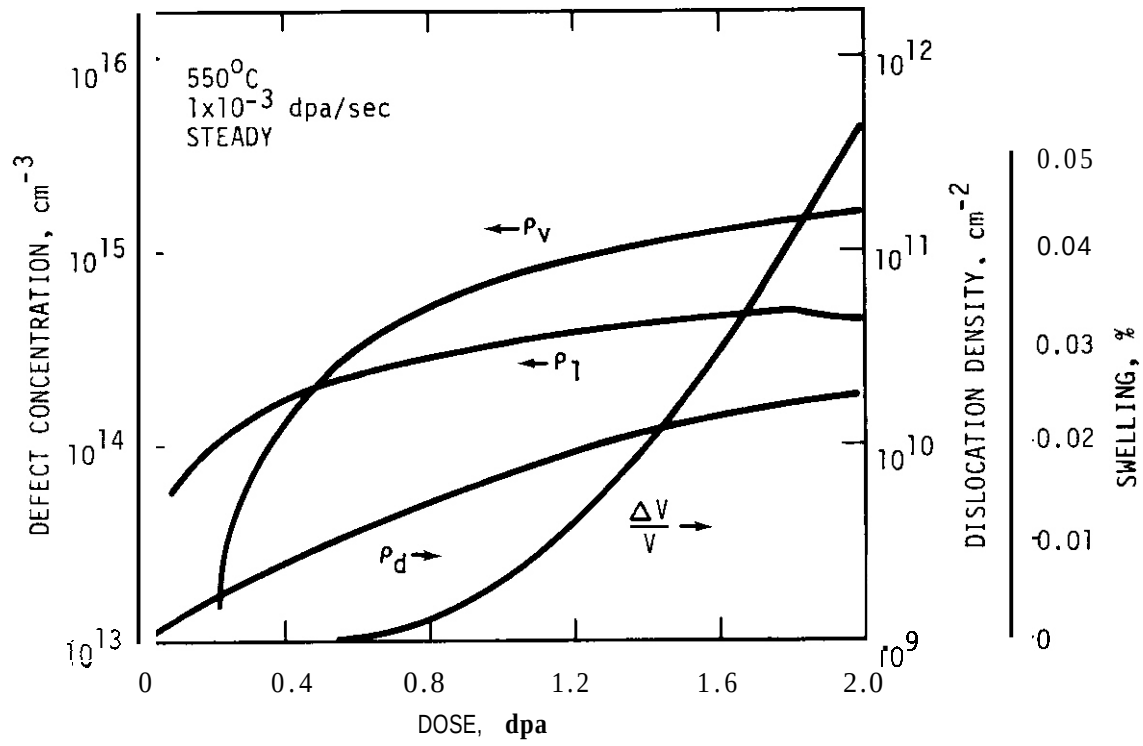
550°C
1x10-3 dpa/sec
STEADY
ρ_v
ρ_l
ρ_d
$\frac{\Delta V}{V}$
DEFECT CONCENTRATION, cm-3
DISLOCATION DENSITY, cm-2
SWELLING, %
DOSE, dpa

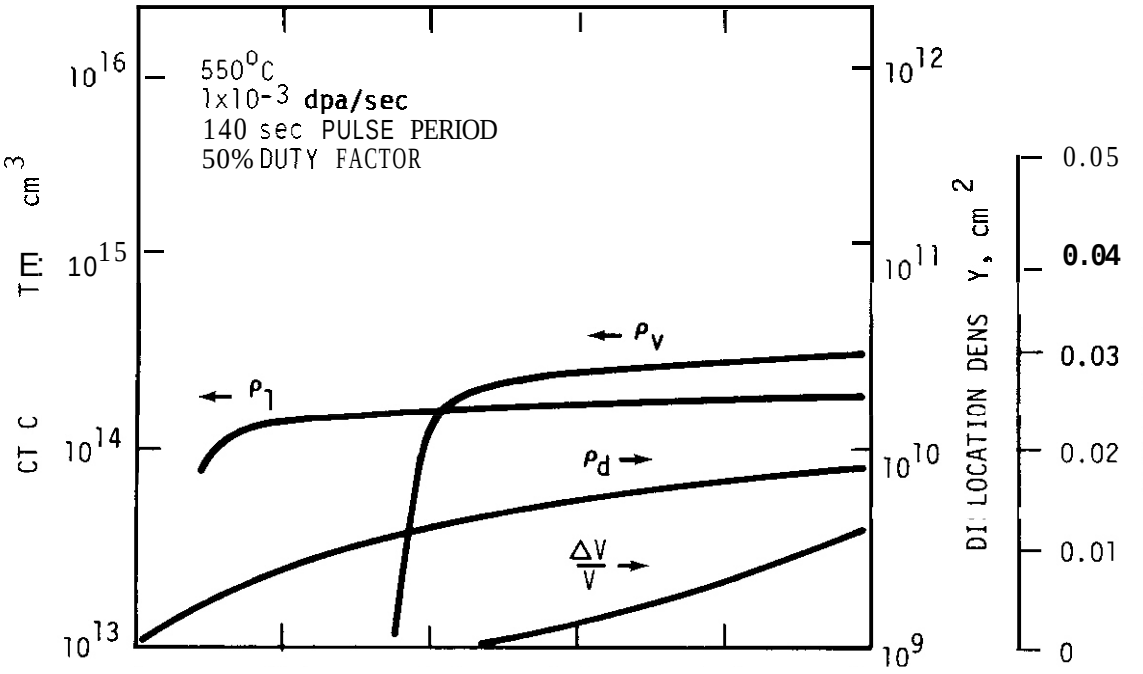
550°C
1x10-3 dpa/sec
140 sec PULSE PERIOD
50% DUTY FACTOR
ρ_v
ρ_l
ρ_d
$\frac{\Delta V}{V}$
SWELLING, %

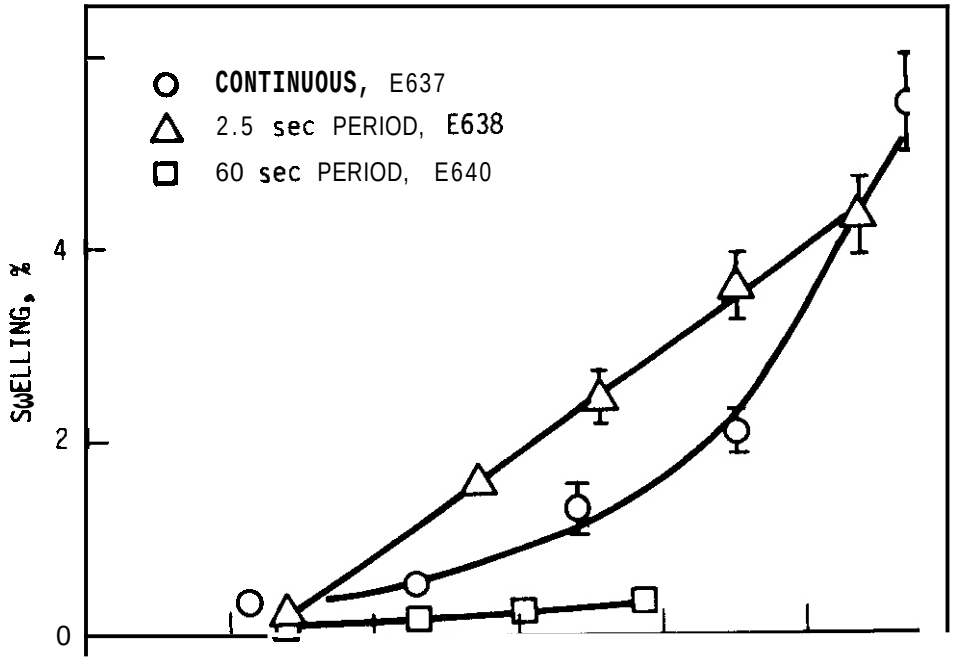

FIGURE 3. Fluence Dependence of Swelling for Continuous Irradiation, E637; Short Pulse Period Irradiation, E638; Effective Pulse Period Irradiation, E640.

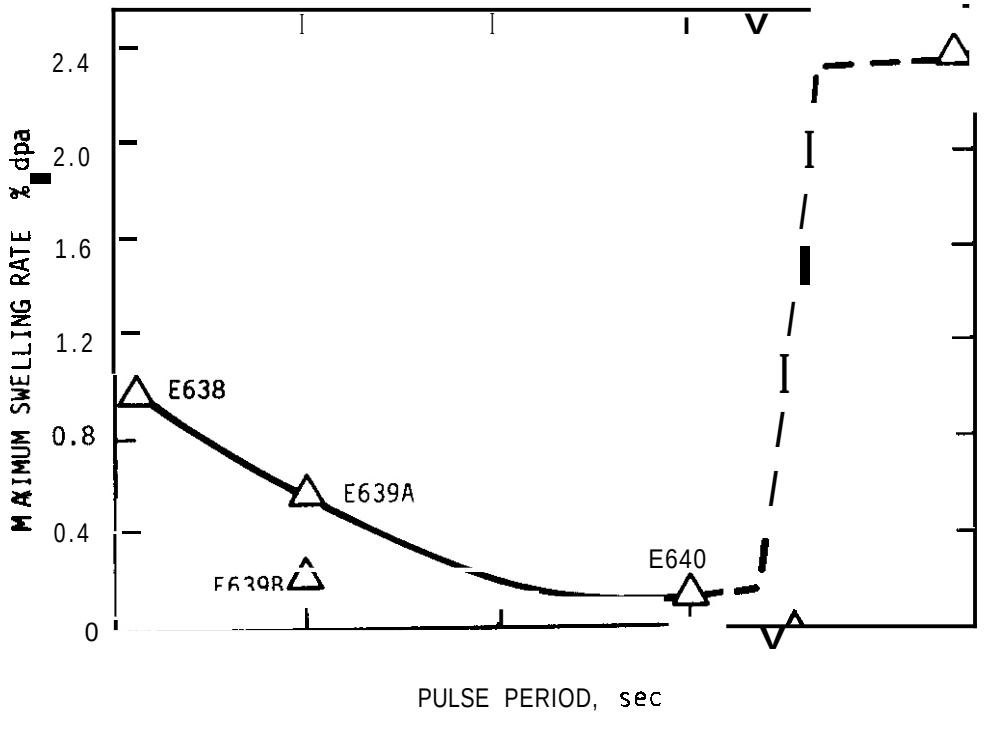

FIGURE 4. The Effect of Pulse Period on the Maximum Swelling Rate at **600°C.**

I. PROGRAM

Title: Radiation Effects to Reactor Materials

Principal Investigator: G. L. Kulcinski and P. Wilkes

Affiliation: University of Wisconsin

II. OBJECTIVE

To develop a fundamental understanding of the formation of voids, loops and precipitates in heavy ion and electron irradiation metals and alloys.

III. RELEVANT DAFS PROGRAM TASK/SUBTASK

II.C.6. Effects of Damage Rate and Cascade Structure on Microstructure.

IV. SUMMARY

Specimens of high purity nickel were irradiated with high energy heavy ions and the resultant microstructure examined along the ion path using a cross sectioning sample preparation technique. Void nucleation was found to be very sensitive to hydrogen introduced into the samples by electropolishing prior to irradiation. Samples containing hydrogen bad void densities of about two orders of magnitude greater than outgassed samoles. A series of hydrogen doped samples were irradiated with 14 MeV nickel ions to fluences from 2 x 10^{15} ions/cm^2 to 1.4 x 10^{17} ions/cm^2 (peak damaqe from 2 to 150 dpa). The increase in the collision cross section as the incident ions slows down causes an increase in displacement rate with depth. The variation in the observed void density, void size and void swelling rates with depth indicate the importance of displacement rate on void simulation studies.

V. ACCOMPLISHMENTS AND STATUS

A. Depth Dependent Void Swelling Rates in Self-Ion Irradiated Nickel -

J. B. Whitley, (Sandia Laboratories, Albuquerque, New Mexico)
G. L. Kulcinski, P. Wilkes, and J. Billen, (University of Wisconsin, Madison, Wisconsin).

1. Introduction

The first walls of Controlled Thermonuclear Reactors (CTR) will be subject to displacement damage and high generation rates of helium from (n,α) type reactions and hydrogen from (n,p) reactions. Hydrogen isotopes will also be introduced into the first wall by interactions with both the plasma and residual hydrogen in the system. Since helium is well-known to aid void nucleation,[1] the present study was performed to investigate the sensitivity of void formation to hydrogen concentration. In the first part of this study, specimens of high purity nickel were injected with hydrogen by electropolishing prior to irradiation. The specimens were subsequently irradiated at 525°C with 14 MeV nickel or copper ions. The resultant microstructure was then compared to that of a thoroughly outgassed specimen.

The post-irradiation analysis of the specimens was performed using a technique which allows the depth dependence of the microstructure to be examined directly.[2,3,4] Under self-ion irradiation, both the damage rate and the total damage level varies by approximately a factor of ten along the ion range. To study this displacement rate effect, a series of nickel specimens were irradiated at 525°C with nickel ions at fluences ranging from 2×10^{15} to 1.4×10^{17} ions/cm^2 (peak dose from 2 to 150 dpa) and the void swelling rates were measured as a function of depth. By examining the structure in cross section, the effects of variation in displacement rate, along with the variation in other features such as PKA spectrum could be studied or observed.

2. Experimental

High purity (>99.995%) nickel samples were irradiated with high energy heavy ions accelerated in a Tandem Van de Graaf accelerator. The depth dependent displacement rates were calculated using the code of Brice[5] with the results for 14 MeV nickel was incident on nickel shown in Figure 1. The details of the accelerator facilities and of the high temperature ultrahigh vacuum target chamber are described elsewhere.[6] The nickel specimens in the form of 1 x 1.2 x 0.2 cm strips were annealed in either an inert gas atmosphere or an ultrahigh vacuum ($<10^{-6}$ Pa) furnace for 1 hr. at 850°C. To introduce hydrogen into the specimens and to clean the surfaces prior to irradiation, the samples were electropolished in a solution of 60% H_2SO_4 and 40% water at room temperature. In some samples, the electropolishing was followed by an anneal at 900°C. for one hour in an ultrahigh vacuum high temperature furnace to provide gas free samples for comparison to those doped with hydrogen. The post-irradiation examination technique, which is described in detail in references 2 and 3, involved electroplating ~1.5 mm of nickel onto each side of the irradiated foil and then slicing the specimen in cross-section using a low speed diamond saw.

3. Results and Discussion

a. Outgassing Studies

In this study, the introduction of hydrogen by electropolishing was found to dramatically enhance the void nucleation rate.

Electropolished foils were irradiated with copper, nickel, aluminum, and carbon ions.[2,4] In all cases, the void microstructures consisted of high ($\sim 10^{15}/cm^3$) void densities with few dislocation loops observed. In the outgassed foils, however, the structure consisted mainly of small unfaulted loops with a few very large voids present near the ion end-of-range. The loop density increased with depth reaching a peak density of

approximately $10^{15}/cm^3$ with loop diameters of about 40 nm. Typical depth dependent microstructures from an electropolished and an outgassed specimen are shown in Figure 2. The foil surface is visible on the left-hand-side of the micrograph with the incident ions having traveled from left to right and come to rest near the right-hand-side of the micrographs.

The void densities measured for an electropolished and an outgassed foil are shown in Figure 3 (note the change of scale of the outgassed curve). While the outgassed foils had void densities over two orders of magnitude smaller than electropolished foils, the void diameter had increased from 20 nm in the electropolished foils to about 100 nm in the outgassed foils. This increase in void size led to similar swelling values in both cases, indicating that the hydrogen introduced by electropolishing was only aiding nucleation and not drastically altering the void swelling rate.

In this study, electropolishing was definitely identified as a sample preparation procedure that was introducing an agent into the samples capable of aiding void nucleation.

Electropolishing has been previously observed to enhance void formation[7] presumably by the introduction of hydrogen. Hydrogen induced deformation of thin foils has been observed after electropolishing at room temperature.[8] Other studies on thoroughly outgassed copper and nickel[9,10] have shown soluble gases to aid void nucleation. Electropolishing apparently charges samples with hydrogen[7] when the polishing is carried out in anything except very low temperature baths (i.e., <-50°C). At higher temperatures, the hydrogen diffuses into the sample faster than material is being removed and hence saturates the sample. Hydrogen would most probably enhance void nucleation by adsorbing onto the void surface and lowering the surface energy.

To aid void nucleation the hydrogen introduced into the samples during the electropolish must not diffuse out of the specimen at irradiation temperatures. However, calculations of hydrogen behavior in metals[10] have revealed hydrogen-vacancy binding energies of only about 0.2 eV. It was also found that molecular hydrogen would not form in the metal lattice. One way hydrogen could be kept in the samples during the heating to irradiation temperatures would be by trapping at other impurities. Carbon and oxygen are both present in small amounts and could form hydrogen compounds that would effectively trap the hydrogen. During irradiation, either the hydrogen would be freed from these traps and migrate to the void nuclei or the hydrogen compound would migrate to the void nuclei. At high temperatures (>900°C), the hydrogen would be freed from the traps and diffuse from the samples. If this mechanism is valid, then the amount of hydrogen available to aid nucleation will depend only on the impurity concentration and on the introduction of sufficient hydrogen to saturate the available trapping sites. The exact sample handlinq procedure and the details of how the hydrogen was introduced (such as the polishing time) will not be important. In this study, electropolishing was found to give reproducible void densities and was used in lieu of the more usual helium injection.

b. Results of 14 MeV nickel ion irradiation

To aid in interpreting the depth dependent void growth rates, a series of seven samples were irradiated at 525°C with 14 MeV nickel ions to fluences ranqing from 2×10^{15} to 1.4×10^{17} ions/cm^2. The samples were prepared for irradiation by annealina for one hour at 850°C in an inert atmosphere and then electropolishing. The development of the void structure as a function of ion fluence is shown in the micrographs of Figure 4. The original foil surface is visible near the left-hand-side of each micrograph with the incident ions having traveled from left to right.

Voids were observed throughout the damage region at all fluence levels (down to 0.4 dpa). There was a denuded region at the front surface of 100 to 150 nm, with the voids adjacent to this denuded region being unusually large at the lower fluences but of normal dimensions at the higher fluences. Voids were observed up to depths of about 3.2 μm. At the highest fluence level (150 dpa at the peak), the voids show signs of partial ordering. This ordering is the early stages of a void lattice formation which has been previously observed in nickel.[11] The void shapes were truncated octahedra except at the highest ion fluence, where the shapes were nearly cubic.

Void data was collected from these samples using 0.25 μm depth intervals and a set of curves such as the one shown in Figure 5 was obtained for each of the seven fluence levels. To assist in interpreting this data, they are plotted in Figures 6-7 by taking data from three depth intervals in each sample and plotting the data against the dpa value of each point as determined from Figure 1 using the appropriate ion fluence. Hence, the set of data points from a given depth will represent data where the main irradiation variable is the total ion fluence (that is, data that are comparable with that taken by conventional sample preparation procedures). A comparison of data sets from different depths of the same sample will involve changes in dose rate, PKA spectrum, etc. From the void density curves of Figure 6, the void density is seen to saturate very early (<0.5 dpa). At a given dpa value, the void density increases with increasing depth, a result expected from the higher dose rate in these regions. The void size curve of Figure 7 also shows the expected behavior of increasing void size with increasing dose, and decreasing void size with increasing dose rate (i.e., depth). Void sizes are either constant or drop slightly above 20 to 50 dpa.

The swelling values from these specimens at the three depths are shown in Figure 8. In general, the swelling curves for each depth increase approximately linearly with dose up to about 20 to 50 dpa, at

I. PROGRAM

Title: Synergistic Helium Production by Boron Doping of Splat Cooled Alloys

Principal Investigator: O. K. Harling

Affiliation: Nuclear Reactor Laboratory, Massachusetts Institute of Technology

II. OBJECTIVE

This work is directed toward the development of better simulation techniques for the synergistic production of helium and displacement damage in first wall structural materials.

III. RELEVANT DAFS PROGRAM PLAN TASK/SUBTASK

4. The damage level necessary for swelling to saturate increased with depth (most probably displacement rate).

5. The swelling value at saturation did not depend on depth (displacement rate).

6. One must be extremely careful when comparing data from many specimens, to always use that information obtained under identical damage conditions (i.e., displacement rate, PKA spectra, etc.). These conditions can change drastically over short distances in ion bombarded solids.

VI. References

1. E.E. Bloom, K. Farrell, M.H. Yoo, and J.O. Stiegler, Consultant Symposium of The Physics of Irradiation Produced Voids, Ed. Nelson, Harwell, U.K. 1974, AERE-R7934, p. 330, (1975).

2. J.B. Whitley, PhD Thesis, Univ. of Wis., (1978).

3. J.B. Whitley, G.L. Kulcinski, P. Wilkes, and H.V. Smith, Jr., "Void Swelling Profiles in Nickel Irradiated with Copper or Nickel Ions," to be published in J. Nucl. Mat. (1979).

4. J.B. Whitley, G.L. Kulcinski, H.V. Smith, Jr., and P. Wilkes, Presented at Ninth Int. Symp. on the Effects of Radiation on Structural Materials, Richland, WA, (1978) (ASTM).

5. O.K. Brice, SAND7500622, Sandia Laboratory, Albuquerque, NM, (July 1977).

6. H.V. Smith, Jr., and R.G. Lott, Nuc. Inst. and Methods, 143, p. 125 (1977).

7. J.R. Buswell, S.B. Fisher, J.E. Harbottle, and D.J.R. Norris, Physical Metallurgy of Reactor Fuel Elements, Ed. by J.E. Harris and E.C. Sykes, Berkeley, (Sept. 1973) p. 170.

8. R.W. Carpenter and G.S. Bauer, "Electron Optical Investigation of Hydrogen-Induced Deformation in Nickel Single-Crystal Foils,'' to be published in Met. Trans. A, (1978).

9. J.M. Lanore, L. Glowinski, A. Rishet, P. Regnier, J.L. Flament, V. Levy, and Y. Adda, Conf. on Fund Aspects of Rad. Damage in Metals, Gatlinburg, TN, p. 1169 (1975). CONF751006.

10. W.D. Wilson, Sandia Laboratory, Livermore, Personal Communication.

11. G.L. Kulcinski, J. Brimhall, and H. Kissinger, Int. Conf. of Radiation-Induced Voids in Metals, Ed. Corbett and Iannielllo, Albany, NY, (1971), CONF710601, p. 449 (1972).

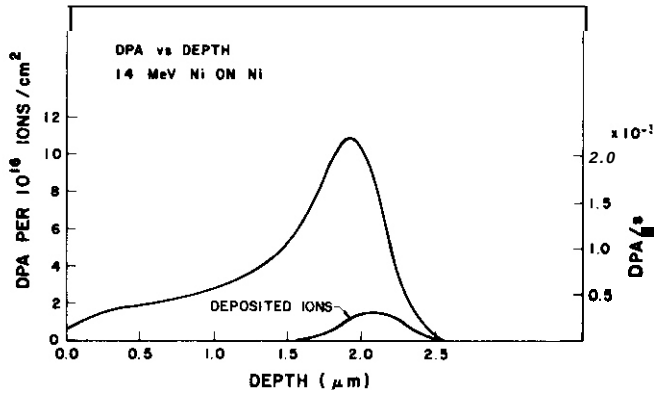

FIGURE 1. Damage Profile as Calculated from Brice Code. (5)

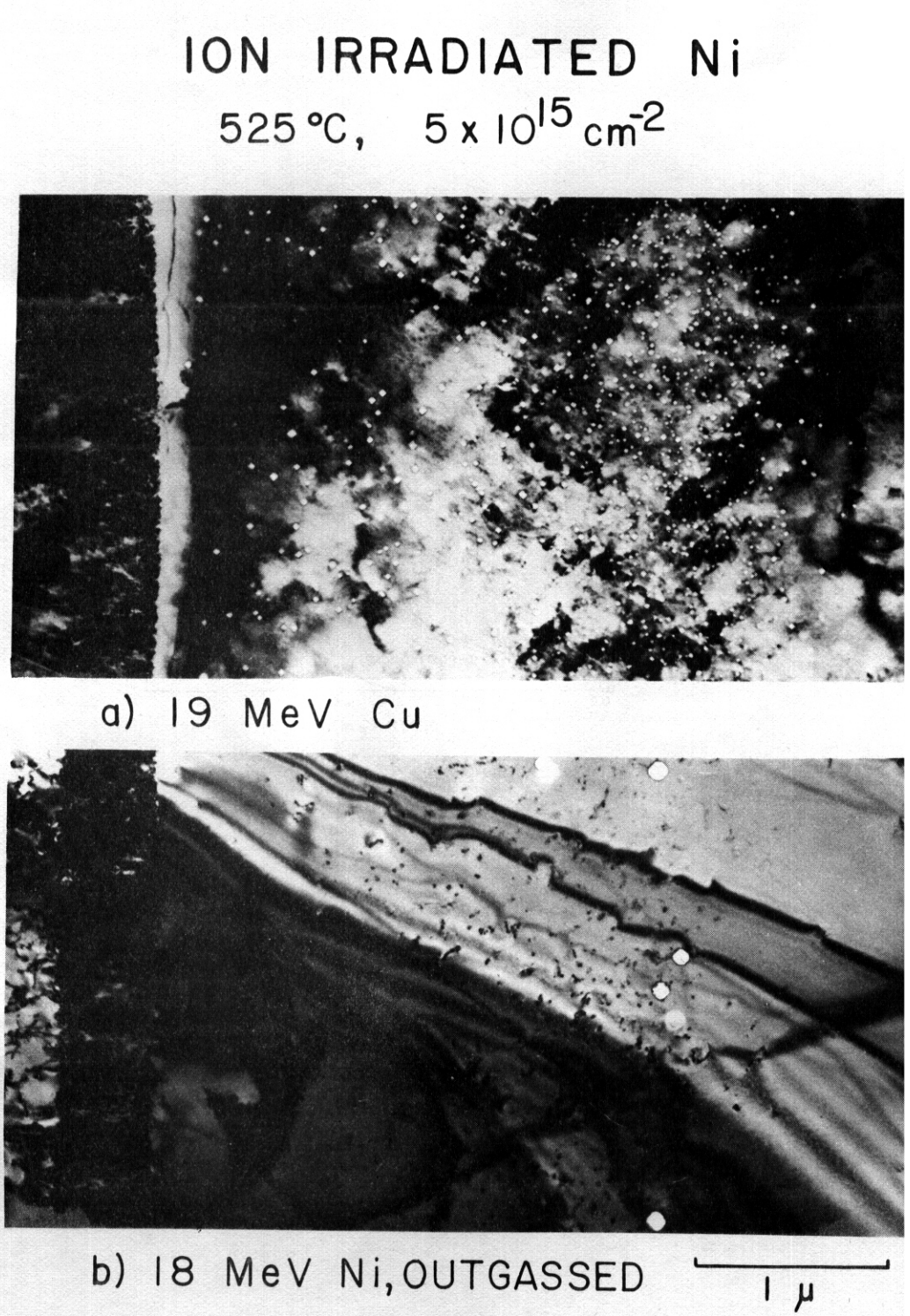

FIGURE 2. Microstructure of Ni Bombarded with 5 x 10^{15} Ions cm^{-2} at with (a) and without (b) Hydrogen in the Matrix.

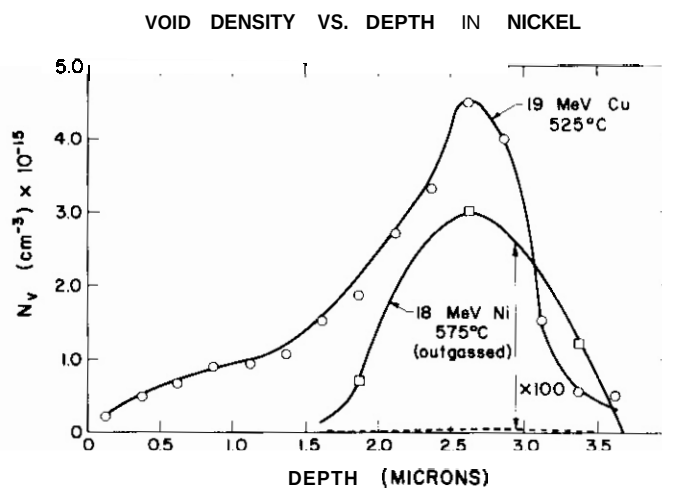

FIGURE 3. Number Density of Voids From Samples in Figure 2. Note Change Outgassed Specimen.

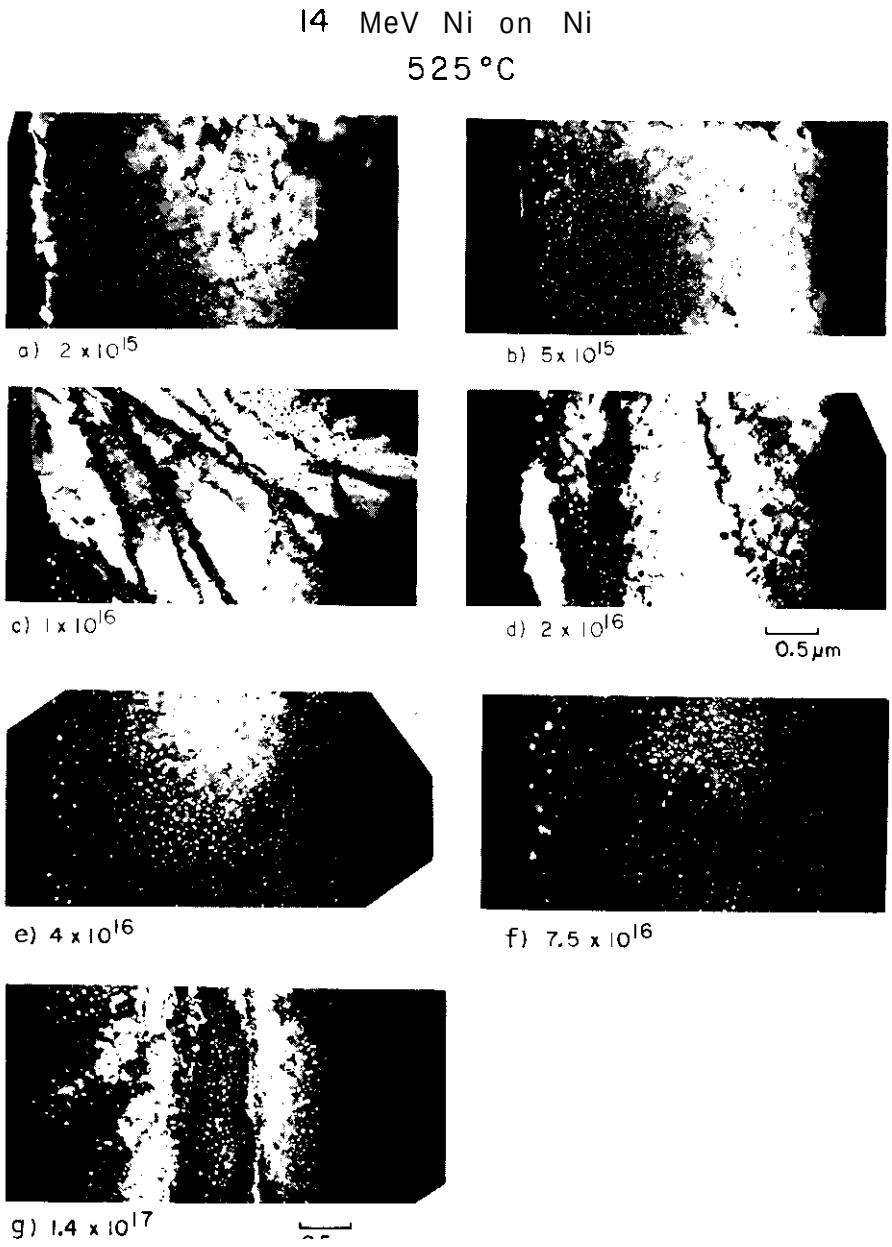

FIGURE 4. Microstructure of Ni Bombarded at 525°C With 14 MeV Ni Ions

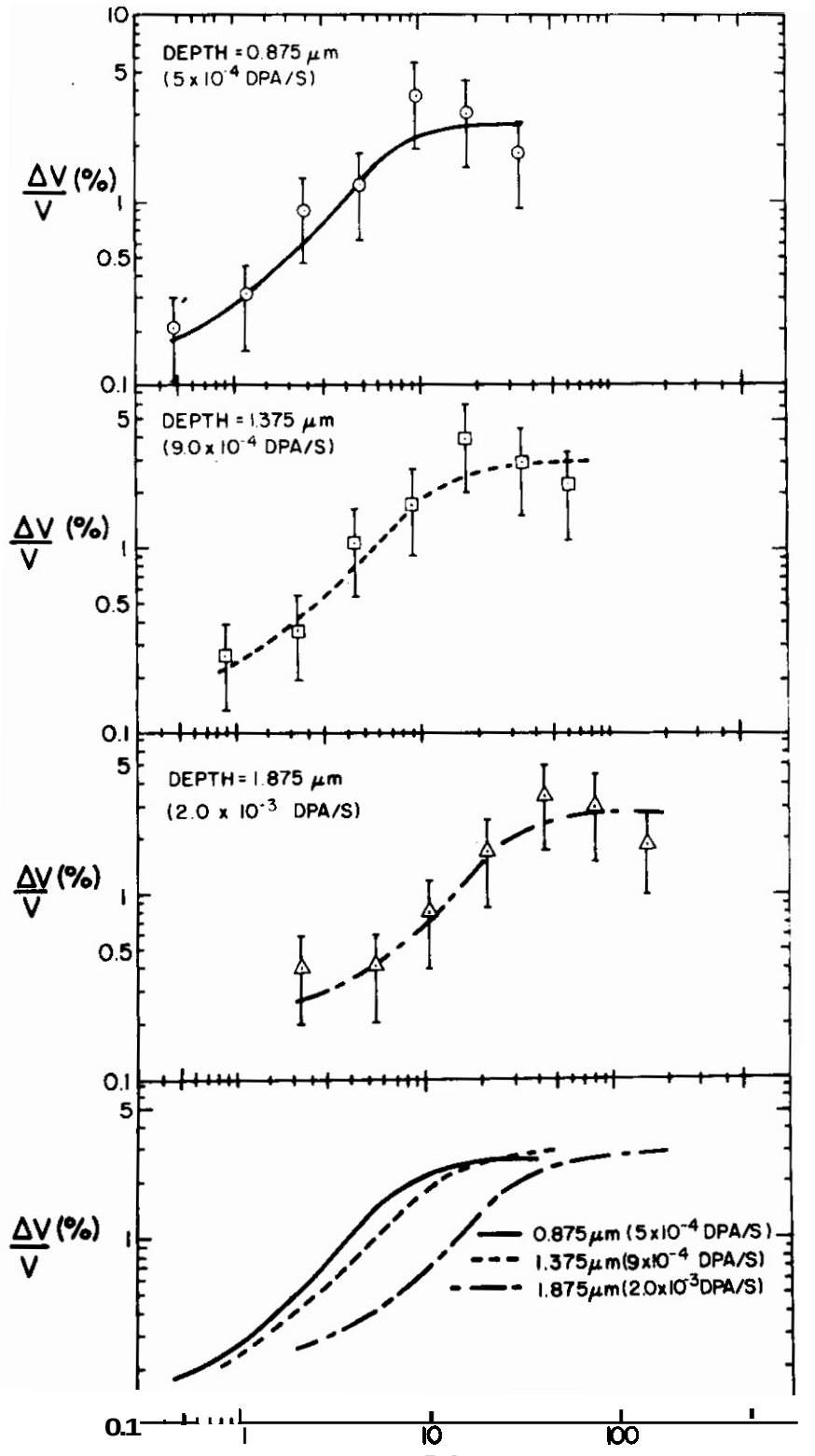

FIGURE 5. Swelling Data at Different Depths in Ni Bombarded at 525°C With 14 MeV Ni Ions. (See Figure 4 for Microstructures.)

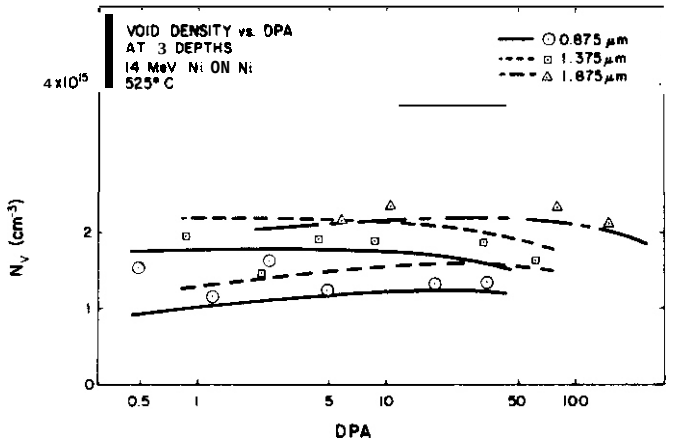

FIGURE 6. Void Density in Ni Bombarded at 525°C With 14 MeV Ni Ions. Note Early Saturation Level.

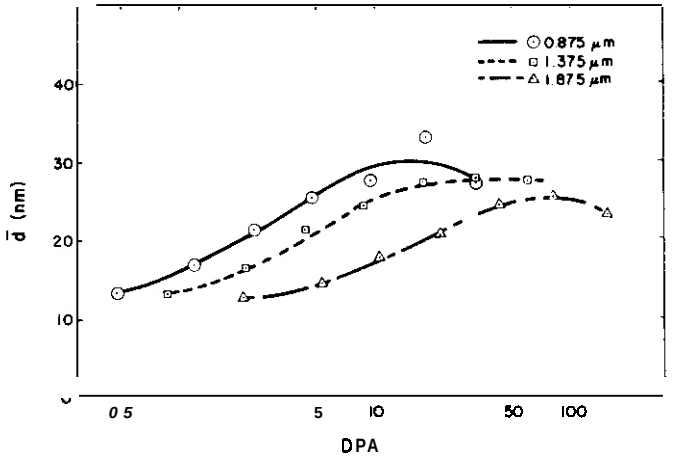

FIGURE 7. Effect of Damage on Void Size in Ni Bombarded at 525°C With 14 MeV Ni Ions.

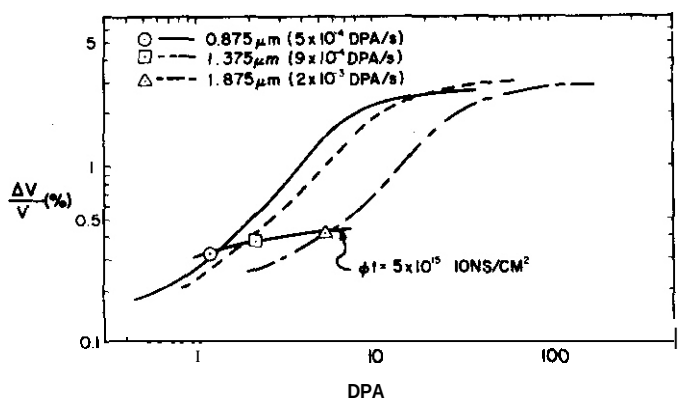

FIGURE 8. Illustration of Damage Rate Effect in Ni Bombarded at 525°C With 14 MeV Ni Ions. The data Points come from the same sample but at slightly different depths (damage rates).

I. PROGRAM

Title: Simulating the CTR Environment in the HVEM

Principal Investigators: W. A. Jesser, R. A. Johnson

Affiliation: University of Virginia

II. OBJECTIVE

The objective of this work is to investigate the role of helium in the fracture of 304 and 316 stainless steel.

III. RELEVANT OAFS PROGRAM TASWSUBTASK

Subtask II.C.8.1 Helium Injection Experiments

II.C.2.1 Helium Mobility, Distribution and Bubble Nucleation

IV. SUMMARY

HVEM tensile samples of 316 stainless steel were irradiated by 80 keV helium ions to produce a population of gas containing cavities referred to here as bubbles. In-situ HVEM fracture studies of these samples showed that crack propagation through the bubbles is associated with bubble enlargement. The greater the plastic deformation, the greater the bubble size increase. Samples irradiated at 600°C and tensile tested at room temperature failed by ductile fracture. Samples irradiated at 600°C and tensile tested at 600°C during irradiation exhibited brittle fracture up to depths of 10 μm below the irradiated surface and ductile fracture at greater sample depths than 10 μm. In these latter tests, it was observed that bands of plastic deformation which formed during the irradiation

acted as preferred sites for bubble growth especially at positions of sharp direction change or intersections of the bands. Crack propagation followed these bubble decorated slip bands and hole formation ahead of the crack tip occurred preferentially at the largest bubbles on the slip band.

V. ACCOMPLISHMENTS AND STATUS

In-situ HVEM Tensile Tests of Helium irradiated 316 Stainless Steel

J. A. Horton, J. J. Bennetch and W. A. Jesser

1. Introduction

HVEM tensile samples of unirradiated 316 stainless steel of the same shape as employed for HVEM tensile samples of neutron irradiated 304 stainless steel were mounted in the tensile stage and bombarded with 80 keV helium ions at 600°C to fluences between 4×10^{16} and 3×10^{18} cm^{-2}. The development of the microstructural features in the samples are described elsewhere;[1] however gas containing cavities were observed in all cases presented here. Tensile tests of these samples were performed at ambient temperature and at 600°C, the same temperatures employed in tensile tests of the neutron irradiated samples.[3,4] The types of fracture studied in these tests of helium irradiated stainless steel were found to resemble those observed in neutron irradiated stainless steel. Crack propagation mechanisms were also investigated.

2. Experimental Data

The equipment, irradiation procedures and sample preparation tech-

niques have been described earlier.[3-5] Table I below summarizes the helium irradiation tensile tests conducted since the last report period.

TABLE I

HVEM Tensile Experiments

Exp#	Test Temp(°C)	Flux/Fluence $cm^{-2}sec^{-1}/cm^{-2}$	Type Fracture*	Microstructure
13	25	$3x10^{14}/7x10^{17}$	T	Faceted bubbles <100nm diameter Other bubbles 200nm diameter
14	25	$3x10^{14}/4x10^{16}$		Few bubbles 60nm diameter
17	25	$2x10^{15}/2x10^{18}$	T	Bubbles 300nm diameter Blisters
19	600	$7x10^{14}/3x10^{18}$	I+T	Bubbles 300nm diameter Blisters

*T = transgranular, I = intergranular

The samples were mounted in the tensile stage of the HVEM and irradiated with 80 keV helium ions at 600°C. When a sufficient population of visible bubbles was achieved some samples were pulled at 600°C during irradiation; other samples were cooled to room temperature and pulled without continued helium bombardment. After the tensile tests to fracture were completed, samples were removed from the HVEM to be analyzed by high resolution TEM as well as by SEM and EDS.

3. Results and Discussion

The role of helium and microstructure in crack propagation mechanisms is being revealed through dynamic video recording of tensile tests in the HVEM. Previous micrographs of wide cracks in neutron irradiated 304 stain-

less steel samples showed that the voids present in the sample enlarged by a factor of 2 in diameter, without a noticeable shape change, when the crack propagated within 200nm of the void during ductile fracture at 600°C.[5] A similar feature has been observed in helium irradiated 316 stainless steel samples pulled at 600°C as well as in samples tested at 25°C. While a small shape change was observed in some of the enlarged cavities, nevertheless an enlargement of bubbles occurred in the immediate vicinity of a narrow propagating crack. In Fig. 1 it can be seen that as the width of the crack increases the diameter of the bubble increases. The width of the crack is a measure of the amount of plastic strain and hence also a measure of the amount of dislocation motion. The increase of bubble diameter by crack propagation does not have an obvious temperature dependence and therefore is likely a plastic deformation induced process rather than a thermally activated process. In cases of ductile fracture in helium irradiated samples tested at room temperature, the characteristic dimples found on the fracture surface are much larger than the enlarged helium bubbles and also occur with a much smaller areal density.

It was possible through frame by frame analysis of video recordings of the HVEM images obtained during tensile testing to investigate the interaction between helium bubble generation and crack progagation. In an experiment for which the tensile deformation and helium irradiation of an unirradiated sample were started at the same time, the following sequence of events occurred. Dislocation motion, confined to a number of slip bands, comnenced and provided preferred sites for bubble growth. At dislocations where a slip band underwent a sharp direction change, or at interesections

between slip bands, especially large bubbles were observed to rapidly grow. These bubble-decorated slip bands served as tracks along which crack propagation occurred. The oversized bubbles at sharp angled regions of the slip bands acted as sites for hole formation ahead of the crack tip. The crack propagated through the bubbles and completed the failure process. The above described sequence of events is not dissimilar from the proposed stress assisted growth and coalescence of bubbles on grain boundaries.[6,7] While crack progagation provides localized stress assisted cavity growth in a stable manner in the proposed model for creep mechanisms,[8] here the process of plastic deformation acting to enlarge the bubbles provides a rapid analog to the creep model and permits rapid crack propagation to occur by the interactive mechanism described from the dynamic video observations. It is possible that this mechanism plays a role in channel fracture which is observed when swelling and hence stress is large.[8,9]

Tensile samples helium irradiated at 600°C to a large dose, 2×10^{18} cm^{-2}, in regions of less than 10μm thickness exhibited ductile fracture when tested at 25°C. Similar samples tested at 600°C exhibited brittle intergranular fracture over depths up to about 10μm below the irradiated surface and ductile knife edge fracture at greater depths. This composite fracture behavior is shown in Figure 2. Even though the sample undoubtedly contained large amounts of helium, still brittle fracture occurred only at the high test temperature.

The calculated projected range of 80 keV helium ions in stainless steel is 282nm, which represents the depth for large localized helium concentrations, however diffusion at 600°C would significantly extend the re-

gion of influence of the helium. The 10μm depth of intergranular fracture provides some estimate of the depth of helium influence on fracture. The heavily damaged upper surface layer of one to two microns in thickness lost its ductility and separated from the more ductile underlayer. In Figure 3 one can see the broken upper layer exposing the rather rough region along which separation took place. The surface roughness in this SEM micrograph is comparable to the bubble sizes measured from HVEM micrographs. The folded appearance of the surface strips along their length suggests additional stress relaxation occurred after separation. Such relaxation would be affected by the helium irradiation during fracture.

The fracture surface was investigated by x-ray microanalysis which revealed a significant chromium depletion in the upper brittle surface layer, a slight chromium depletion on the brittle intergranular fracture surface, and a nominal 316 stainless steel composition on a transgranular fracture surface. Clausing and Bloom[10] have reported a chromium depletion on an intergranular fracture surface of neutron irradiated 304 stainless steel as compared to a transgranular fracture surface.

Grain boundaries typically exhibit oversized bubbles at high temperature. During plastic deformation, helium irradiation has produced grain boundaries which exhibit zones denuded of small bubbles. Figure 4 is an example of this behavior, but it represents a minority of the grain boundaries in this sample because most of the boundaries were not associated with denuded zones. As mentioned earlier boundaries served as sites for crack propagation.

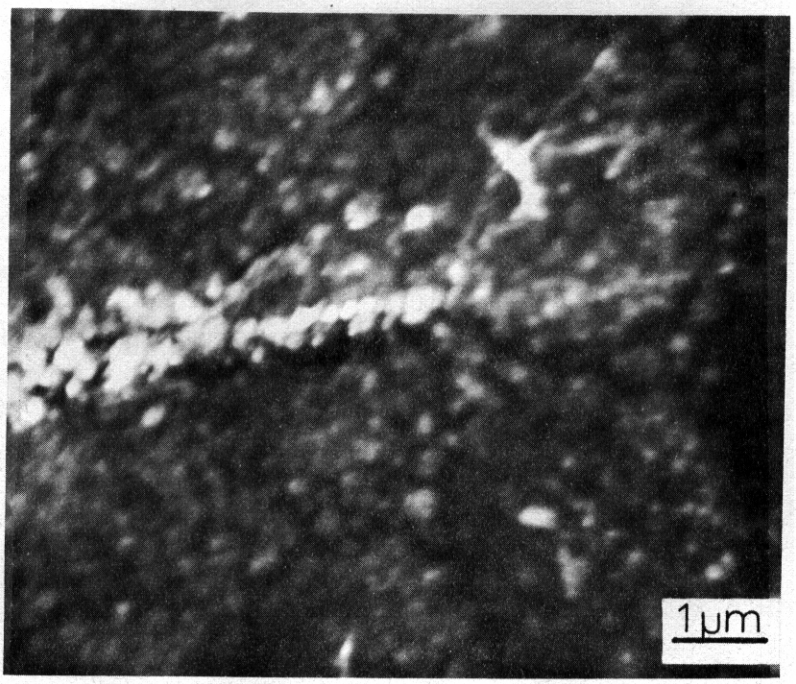

Fig. 1 HVEM micrograph showing crack induced bubble enlargement with tensile deformation at 600°C during 80 keV helium irradiation of 316 stainless steel.

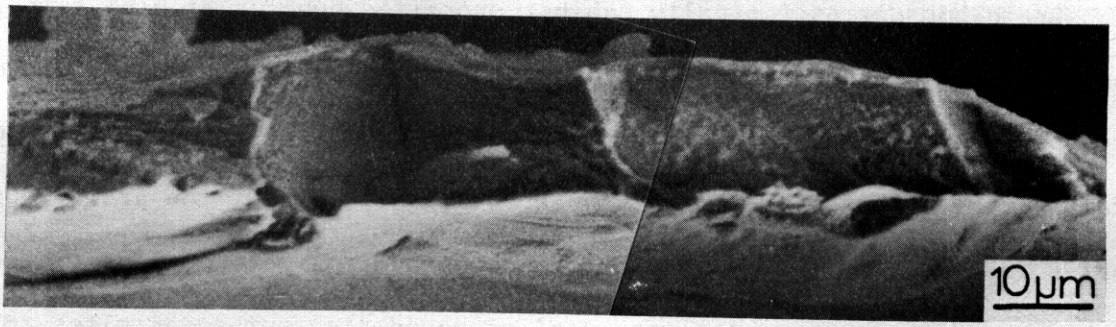

Fig. 2 SEM micrograph of fracture surface of sample shown in Fig. 1. Note intergranular fracture and ductile fracture regions.

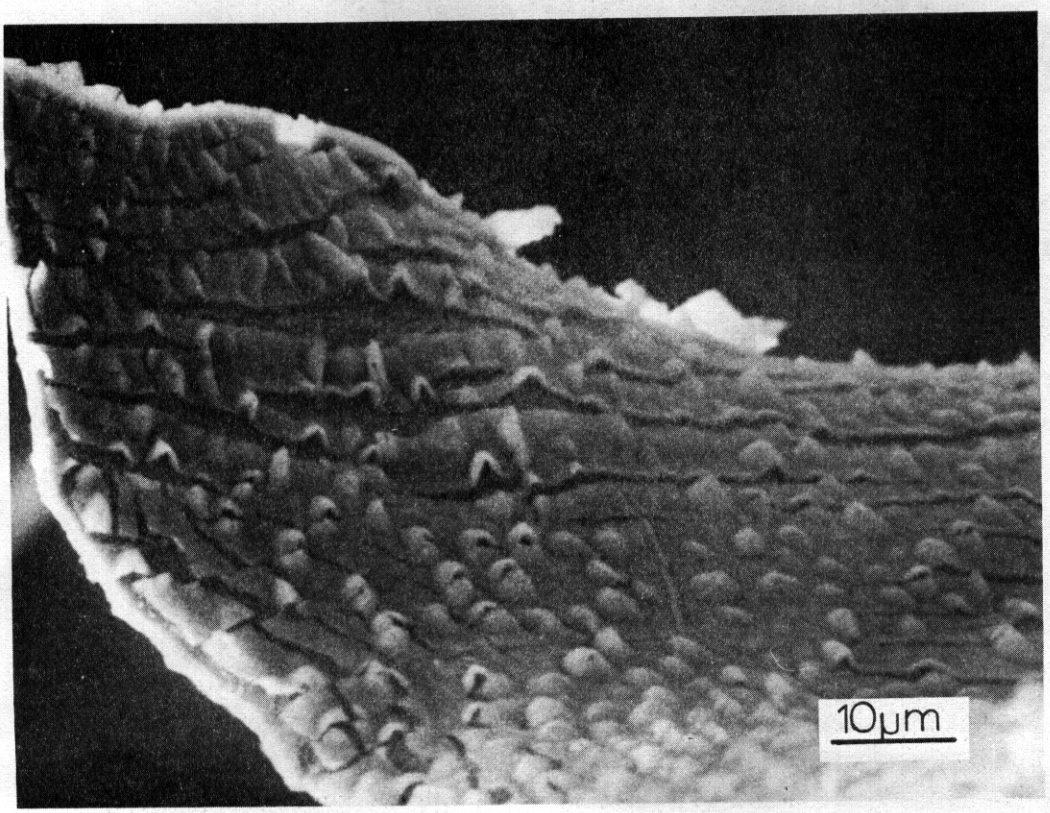

Fig. 3 SEM micrograph of sample shown in Figs. 1 and 2. Blistered upper layer is brittle from helium irradiation, underlayer is comparatively ductile. Note folds and points of adherence between the underlayer and overlayer. Sample edge is fracture edge.

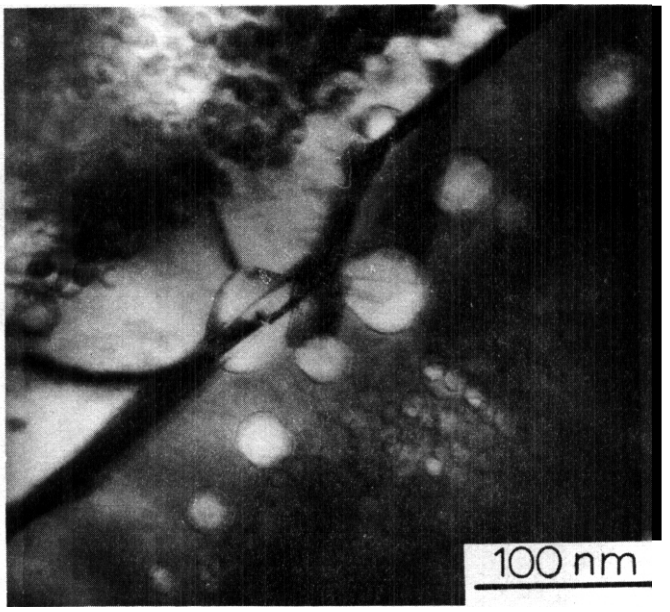

Fig. 4 TEM micrograph of helium irradiated 316 stainless steel tensile tested at 25°C. Note zones denuded of small cavities.

VI. REFERENCES

1. J. I. Bennetch, L. S. Horton and W. A. Jesser, "In-Situ Studies of Helium Irradiated Stainless Steel," Damage Analysis and Fundamental Studies Quarterly Progress Report, July-September 1978, D. Doran, ed., DOE/ET-0065/3 (1979).

2. J. I. Bennetch, M. L. Sattler, L. S. Horton, J. A. Horton and W. A. Jesser, "HVEM Observations of in-situ He-ion Bombardments," Proceedings of the First Topical Meeting on Fusion Reactor Materials, to be pub. in J. Nucl. Materials.

3. J. I. Bennetch, J. A. Horton, W. A. Jesser, D. Kuhlmann-Wilsdorf, R. A. Johnson and H. G. F. Wilsdorf, "In-Situ HVEM Tensile Tests of Irradiated and Unirradiated Stainless Steel," Damage Analysis and Fundamental Studies Quarterly Progress Report, April-June 1978, D. Doran, ed., DOE/ET-0065/2 (1979).

4. J. A. Horton, J. I. Bennetch and W. A. Jesser, "In-Situ HVEM Fracture Studies of Neutron and Helium Ion Irradiated Stainless Steel," Proceedings of the First Topical Meeting on Fusion Reactor Materials, to be published in J. Nucl. Materials.

5. W. A. Jesser, J. A. Horton and J. I. Bennetch, "In-Situ HVEM Tensile Tests of Irradiated and Unirradiated Stainless Steel," Damage Analysis and Fundamental Studies Quarterly Progress Report, Jan-March 1978, D. Doran, ed., DOE/ET-0065/1 (1978) 203.

6. D. Hull and D. E. Rimmer, Phil. Mag., 4 (1959) 673.

7. M. V. Speight and J. E. Harris, Met. Sci. Journal, 1 (1967) 83.

8. E. E. Bloom, Radiation Damage in Metals, N. L. Peterson and S. D. Harkness, eds., ASM (1975) 295.

9. R. L. Fish, J. L. Straalsund, C. W. Hunter and J. J. Holmes, Effects of Radiation on Substructure and Mechanical Properties of Metals and Alloys, ASTM Spec. Tech. Pub. 529, (1973) 149.

10. R. E. Clausing and E. E. Bloom, Grainboundaries in Engineering Materials, J. L. Walter, J. H. Westbrook and D. H. Woodford, eds., Claitors Publ. Div. (1975) 491.

VII. FUTURE WORK

The complex nature of the fracture mechanisms in neutron irradiated and helium irradiated stainless steel suggest a continued investigation into the role of helium in the fracture and crack propagation processes. In particular strain rate effects should be considered.

I. PROGRAM

Title: Irradiation Response of Materials
Principal Investigators: J. A. Spitznagel, W. J. Choyke
Affiliation: Westinghouse Research and Development Center

II. OBJECTIVE

The objective of this work is to assess the phenomenology and mechanisms of microstructural evolution in materials exposed to simultaneous helium injection and creation of atomic displacement damage by a second ion beam; and their effects on mechanical behavior.

III. RELEVANT DAFS PROGRAM PLAN TASK/SUBTASK

SUBTASK II.C.II		Effects of Cascades and Flux on Flow
	II.C.7	Effect of Helium and Displacements on Flow
	II.C.8	Effect of Helium and Displacements on Fracture

IV. SUMMARY

Tensile tests were performed on Type 316 stainless steel foils several microns thick for comparison with tests on specimens of conventional size.

V. ACCOMPLISHMENTS AND STATUS

A. Miniaturized Tensile Specimens*

The mechanical behavior of miniature specimens is of interest in studies of radiation effects on mechanical properties. In the case of

*Funded by non-DoE sources

neutron irradiation, the large penetration range of neutrons has made it possible to evaluate bulk material using standard laboratory size test specimens. For light particle and ion irradiations, by contrast, the range of penetration is very small -- microns, versus hundreds of centimeters for neutrons. This limited range of penetration by light particles and ions has led to emphasis on microstructural effects with little attention to direct mechanical property measurements. Current interest in fusion reactors and the present need to use ion irradiations and small specimen irradiations in low flux 14 MeV neutron sources such as RTNS II to simulate the damage expected from fusion reactions gives renewed incentive to make mechanical property tests on ultrathin foils. A question which immediately arises is whether the properties of such thin foils are representative of bulk material? To answer the question tensile tests were performed on Type 316 stainless steel foils having a thickness of a few microns.

Experimental Procedure

Type 316 SS was cold rolled to foil strips 7.6 m long by 10 cm wide. Following an intermediate anneal at a thickness of 12.5 μm, the material was cold rolled to thicknesses of 5 μm and 2.5 μm.

Tensile specimens were stamped from the foil with the specimen axis parallel to the rolling direction. The female die contained a rubber padding and a thin foil of copper was placed between the padding and 316 SS foil. Since the as-stamped specimens had sharp edges, they were not given any subsequent surface preparation treatments. The specimens were held between alumina plates and vacuum (1.3 x 10^{-3} Pa) annealed by holding for several minutes at temperatures from 973°K to 1273°K. Excessive evaporation occurred at higher annealing temperatures. No effort was made to determine compositional changes (loss or contamination), if any, during heat treatment. The specimen gage section had parallel sides 9.4 mm long by 2.54 mm wide. For mounting, the specimen grip end or head was laid in a female die and then held in place with a male die. Thus, the specimen was friction gripped; no slippage occurred during testing. The slots in

the female dies were only slightly wider than the width of the specimen head and were pre-aligned with the axis of the pullrod.

All tests were run at room temperature at a constant crosshead rate. Except for a few tests the rate was 9×10^{-5} sec^{-1} nominal strain rate. Load and crosshead displacement were recorded on the Instron strip chart recorder and stresses and strains (based on crosshead motion) were calculated using the original cross-sectional area and gage length.

Results

The as-rolled foils were strong but quite brittle. Strength decreased and ductility increased on annealing as shown in Fig. 1. Small yield points, undulations and low initial rate of work hardening were features frequently observed.

Over 100 tests were run and reproducibility was fairly good. Results for five identical tests are shown in Fig. 2. No unusual effect of strain rate was observed as indicated in Fig. 3.

Tensile properties as a function of annealing temperature and foil thickness are shown in Fig. 4. In the as-cold rolled condition, the thinnest foils failed prior to reaching the 0.2% offset yield strength. After annealing, there was little effect of foil thickness on strength properties but ductility was somewhat higher for the thicker foils. It is evident in Figures 2 and 4 that the spread in ductility is quite large even for given conditions of foil thickness and annealing temperature. The reason for this spread is not known, but undoubtedly it could be reduced somewhat by refinement of test procedures.

Plastic deformation was uniform throughout the gage section right up to failure. In most cases, fracture occurred by a small crack forming at the specimen edge and slowly propagating across the width perpendicular to the tensile axis. In a few cases, particularly in the thinnest foils, a small hole suddenly appeared toward the center, perhaps at an inclusion (though none were observed) and then cracks emanating from the hole

propagated in both directions toward the edges.

There was little, if any, width strain but a large thru-thickness strain at the point of fracture. The recrystallized grain size is larger than the specimen thickness. As the transgranular crack traversed the specimen, each grain necked down, one after the other, in a mode similar to a chisel point failure in a ductile single crystal. As fracture progressed, the specimen buckled laterally for a short distance on each side of the plane of the crack.

Several stress-strain curves for 5 μm thick foils and a curve typical of bulk, annealed material are shown in Fig. 5. Based on this comparison, the curve for 1273°K annealed foil is judged to be representative of the behavior of bulk material except that the particular mode of failure in the foils leads to early termination of the stress-strain curve.

Discussion

It is generally well known that thin foils or thin films produced by processes such as vapor deposition or electrodeposition have unusual mechanical properties[1,2]. These materials oftentimes have a highly defected microstructure (perhaps 10^{12} cm^{-2} dislocation density) and contain high residual stresses. They are usually much stronger than bulk material. They are also quite brittle even if the bulk material is extremely ductile. Thus, they behave like single crystal whiskers or heavily cold worked material. By contrast, Lawley and Schuster[3] showed that thin copper foils prepared from bulk material had properties typical of bulk material. The present results show that 316 SS foils prepared from the bulk also exhibit behavior representative of bulk material.

Though microstructural effects, surface effects and specimen geometry all could cause thin foils to behave differently from bulk material, none were sufficient in the present tests to rule out the use of micron-thickness foils for assessing the effect of irradiation damage on mechanical properties. Progressive increase in irradiation damage should change the stress-

strain response in a manner similar to that shown in Fig. 1 in going from the annealed to the cold rolled condition, and this change can be readily measured. Moreover, since the foils fail transgranularly, a shift to intergranular fracture due to irradiation would be easily detected.

VI. REFERENCES

1. R. W. Hoffman, "Mechanical Properties of Non-Metallic Thin Films," Physics of Nonmetallic Thin Films, C. H. S. Dupay and A. Cachard, editors, Plenum Press, N. Y., 1976.

2. T. D. Dudderar and F. B. Koch, "Mechanical Property Measurements on Electrodeposited Metal Foils," Properties of Electrodeposits - Their Measurements and Significance, R. Sard et al, editors, Electrochemical Society, 187, 1974.

3. A. Lawley and S. Schuster, Trans. AIME, 230, 27, 1964.

VII. FUTURE WORK

The results of the scaling experiments will be used to design specimens suitable for studying the effects of dual ion (HEIBS Facility at the University of Pittsburgh) or 14 MeV (RTNS II) irradiation on flow and fracture behavior.

VIII. PUBLICATIONS

D. L. Harrod and D. A. Kaminski, "Stress-Strain Behavior of Micron Thickness 316 SS Foils," Accepted for publication in Mechanics Research Communications (1978).

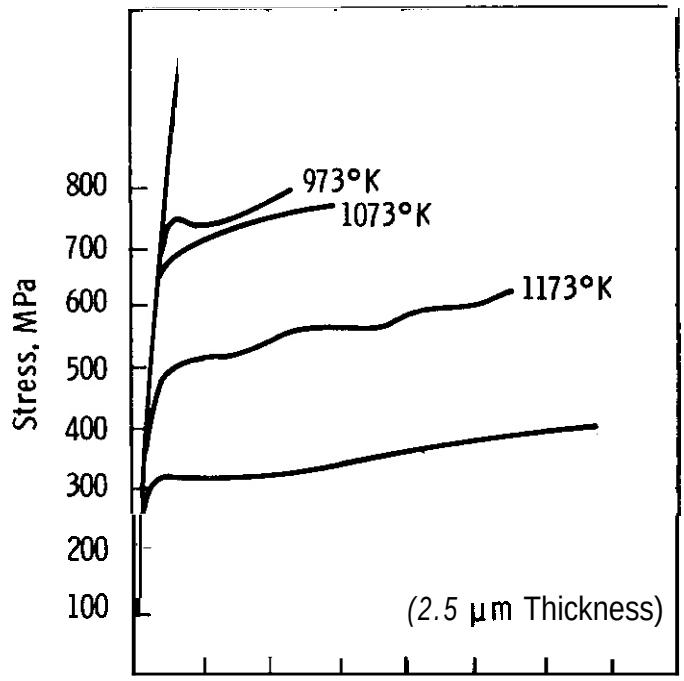
Stress, MPa
800
700
600
500
400
300
200
100
973°K
1073°K
1173°K
(2.5 μm Thickness)

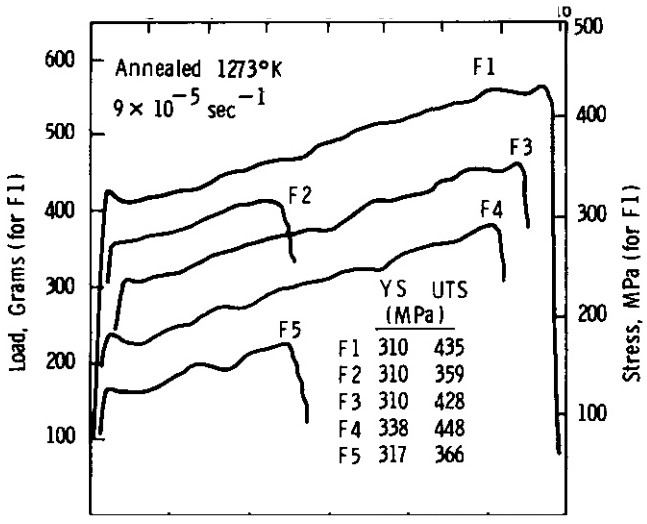
Annealed 1273°K
9 × 10⁻⁵ sec⁻¹
F1
F2
F3
F4
F5
YS UTS
(MPa)
F1 310 435
F2 310 359
F3 310 428
F4 338 448
F5 317 366
Load, Grams (for F1)
Stress, MPa (for F1)
600
500
400
300
200
100

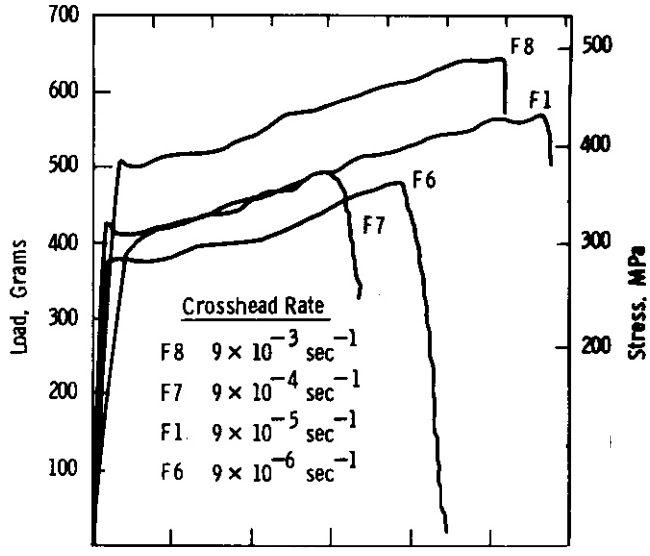
F8
F1
F6
F7
Crosshead Rate
F8 9 × 10⁻³ sec⁻¹
F7 9 × 10⁻⁴ sec⁻¹
F1 9 × 10⁻⁵ sec⁻¹
F6 9 × 10⁻⁶ sec⁻¹
Load, Grams
Stress, MPa
700
600
500
400
300
200
100

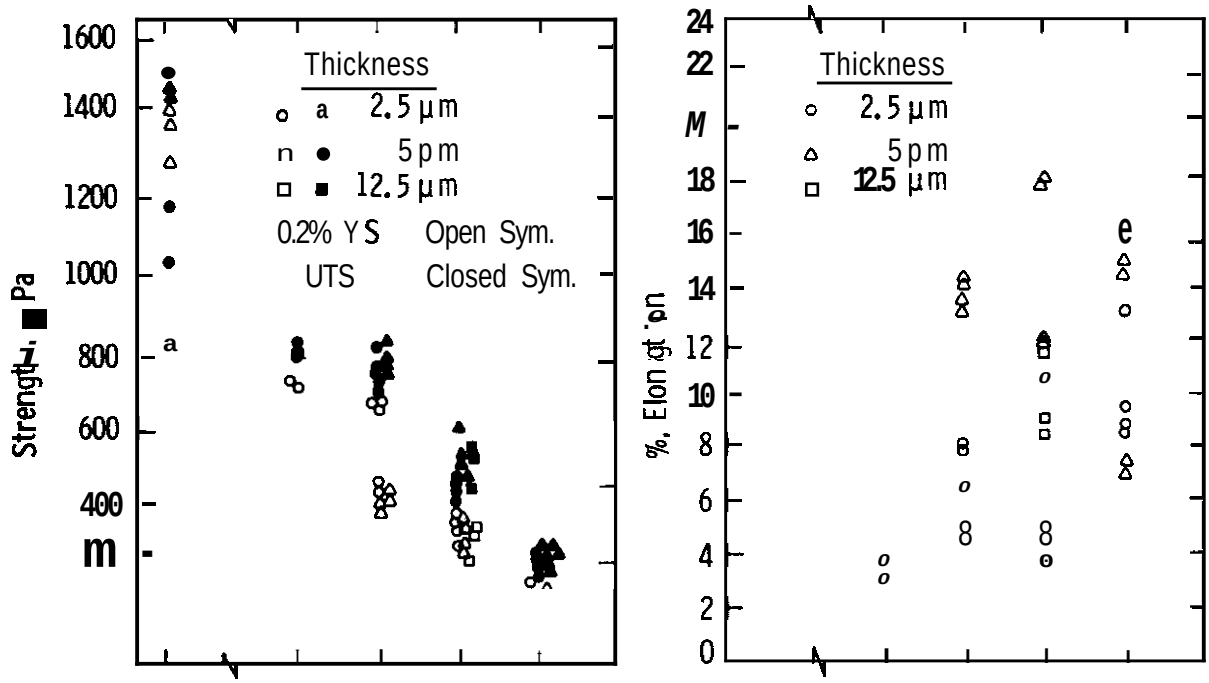
Thickness
2.5 µm
5 µm
12.5 µm
0.2% YS Open Sym.
UTS Closed Sym.
Strength, MPa
1600
1400
1200
1000
800
600
400
Thickness
2.5 µm
5 µm
12.5 µm
% Elongation
24
22
18
16
14
12
10
8
6
4
2
0

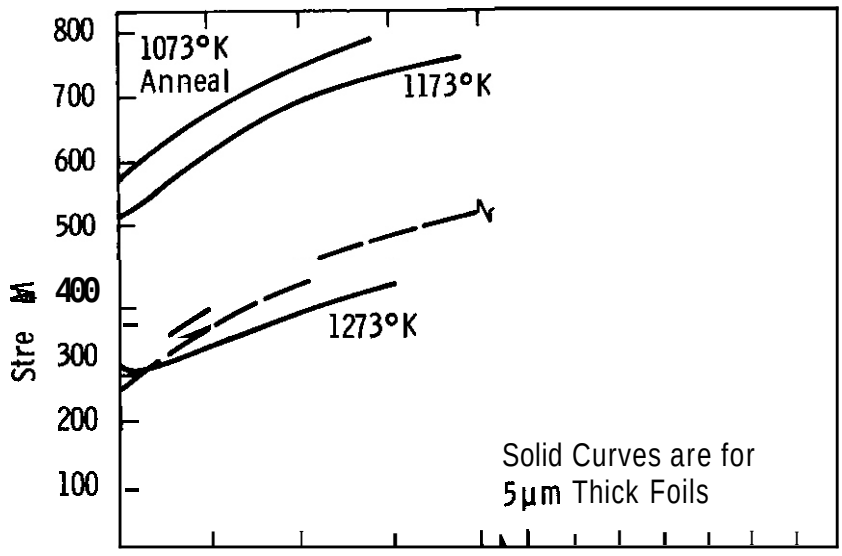
1073°K
Anneal
1173°K
1273°K
Solid Curves are for
5 µm Thick Foils
800
700
600
500
400
300
200
100

I. PROGRAM

Title: Effects of Irradiation on Fusion Reactor Materials
Principal Investigator: F. V. Nolfi, Jr.
Affiliation: Argonne National Laboratory

II. OBJECTIVE

The objective of the work is to establish the effects of flux, stress and alloying elements on the creep-deformation behavior of various classes of candidate MFR materials during light-ion irradiation.

III. RELEVANT DAFS PROGRAM PLAN TASK/SUBTASK

SUBTASK II.C.III.1 Light Particle Irradiations

IV. SUMMARY

Torsional creep-rate measurements were made on wire specimens of solution annealed and aged Type 316 stainless steel (MFE Ht. #15893) at 400°C during 21 MeV deuteron irradiations. A "negative creep-rate" of $5.6 \times 10^{-10}\ s^{-1}$ was observed at a maximum shear stress of 80 MPa for a dose rate of -2.2×10^{-6} dpa $\cdot\ s^{-1}$.

V. ACCOMPLISHMENTS AND STATUS

A. Creep-Deformation Behavior of Type 316 Stainless Steel — V. K. Sethi

During FY 1978, a programme was initiated to perform light-ion based irradiation creep experiments on solution annealed and aged Type 316 stainless steel. Some unexpected results were obtained during the course of this investigation, and are described below.

In the torsional creep apparatus a wire specimen is stressed in torsion by an electromagnetic loading technique. Rotation or strain is measured by an optically coupled photocell tracking system. Temperature control of the specimen is obtained by resistance heating and by varying the temperature of flowing helium that passes perpendicularly across the specimen. Coupling between the control and measuring functions is through an infra-red pyrometer, feed-back system. The apparatus is installed at the ANL Cyclotron where the ion beam from the Cyclotron is defined by an aperture and a set of collimators located, respectively, 25 cm and 2 cm in front of the specimen. The ion beam is monitored by two chromel-alumel thermocouples located in the plane of the specimen on either side. Fluence is determined from the integrated faraday cup current located 5 cm behind the specimen. The faraday cup is isolated from the rest of the apparatus by a thin aluminum window and is in vacuum.

Type 316 stainless steel (Ht. #15893) was obtained from the MFE stockpile and processed into 10 cm long, 0.075 cm diameter wire pieces. These were solution annealed at $950^{o}C$ for 10 minutes in an inert atmosphere, and then aged for 6 h at $800^{o}C$. The creep specimens were fabricated from the wires by electropolishing a reduced section (-0.0130 cm diameter and -0.65 cm long). A typical specimen prepared in this fashion contains at least ten grains across the diameter.

Specimen 316 SA 15893-03, with a minimum diameter -0.0128 cm and gauge length -0.54 cm, was mounted in the torsional creep apparatus. The specimen was heated to $400^{o}C$ and a torque of 3.1×10^{-5} N·m applied (maximum shear stress at minimum diameter -80 MPa). The specimen crept for 150 h at which time the creep-rate ($\dot{\gamma}$) was $2.8 \times 10^{-11}\ s^{-1}$. At constant torque, the temperature was increased to $500^{o}C$ for 48 h and then lowered back to $400^{o}C$; the creep-rate at $400^{o}C$ remained unaltered. The specimen was cycled between these two temperatures several times to ascertain that the creep-rates remained constant, indicating that the microstructure was stable at these temperatures.

The specimen was then irradiated with 21 MeV deuterons at an average dose-rate of ~2.0 x 10^{-6} dpa • s^{-1} to a total dose of 0.1 dpa. The strain-time behavior during irradiation is shown in Figure 1. Figure 1 illustrates that as-soon-as the irradiation is started the sense of deformation reverses, i.e., rotation or strain occurs in a direction opposite to that of the applied stress and continues to do so for the duration of the test. The average strain-rate during irradiation is ~6 x 10^{-10} s^{-1} and seems to be dose-rate dependant as indicated by the first three hours of irradiation during which time the beam current was being adjusted. As illustrated in the figure, the deformation behavior reverts to normal when the beam is turned off. The effect has since been reproduced on the same specimen and on, similarly prepared, different specimens. In every case, it was observed that the deformation during irradiation occurs against the applied stress.

Negative strains can be rationalized in terms of an irradiation induced increase in either or both of the shear modulus via redistribution of solute, or the diameter of the specimen via void swelling and/or precipitation. The net effect of both is to cause a reduction in the elastic component of the strain at constant torque. If the rate of change of the elastic strain is larger than the creep strain rate, an apparent "negative creep-rate" will result. The exact nature of any irradiation induced microstructural change is being investigated.

VI. REFERENCES

None

VII. FUTURE WORK

In order to ascertain the origin of the anamolous irradiation creep-deformation behavior of solution annealed and aged Type 316 stainless steel, transmission and scanning electron microscopy will be performed on sections of specimen 316 SA 15893-03.

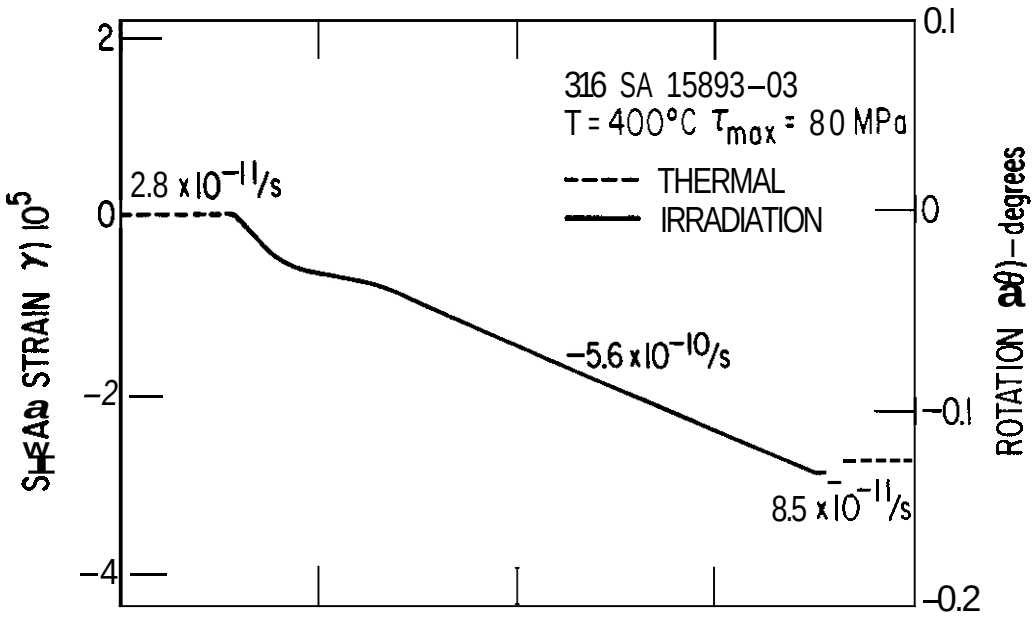

FIGURE 1. Strain-time behavior of a wire specimen of solution annealed (950°C; 10 min.) and aged (800°C; 6h) Type 316 stainless steel (MFE Ht. #15893) during irradiation with 21 MeV deuterons (2.0 x 10^{-6} dpa • s^{-1}). Note that during irradiation deformation occurs against the applied stress.

I. PROGRAM

Title: Irradiation Response of Materials

Principal Investigators: J. A. Spitznagel, W. J. Choyke

Affiliation: Westinghouse Research and Development Center

II. OBJECTIVE

The objective of this work is to assess the phenomenology and mechanisms of microstructural evolution in materials exposed to simultaneous helium injection and creation of atomic displacement damage by a second ion beam.

III. RELEVANT OAFS PROGRAM PLAN TASK/SUBTASK

SUBTASK II.C. 18.1 Nucleation Experiments

IV. SUMMARY

Cavity size distributions were compared for 316 SS targets in solution treated (1050°C) and 20% cold worked condition following dual-ion or sequential bombardment with He + Si ions at elevated temperatures. The results appear to be consistent with recent predictions of theory which suggest that rapid cavity growth can occur once a critical bubble size is reached. Cold work was very effective in suppressing cavity nucleation and growth at low temperatures, but swelling in the cold-worked specimens exceeded that in solution annealed material at temperatures above 700°C.

V. ACCOMPLISHMENTS AND STATUS

A. The Effects of Cold Work and Mode of Helium Implantation on Cavity Size Distributions and Swelling in 316 SS

The problems of designing mixed spectrum reactor experiments requiring spectral tailoring to achieve constant appm helium/dpa ratios and pre-implanting helium into materials which will not experience sufficient helium generation by transmutation reactions are substantial. Charged particle irradiation experiments will hopefully be able to provide some insight into the effects of helium on microstructural evolution and on the need for spectral tailoring.

At present, two ion accelerators are being used to either sequentially or simultaneously implant helium ions and produce atomic displacement damage with 28 MeV Si^{+6} ions in 316 stainless steel from the MFE heat. Targets are currently 3 mm diameter discs prepared from solution annealed (1050°C - 1 h) or cold-worked material (1050°C - 1 h + 20% C.R.). In the sequentially bombarded targets, helium has been pre-implanted at temperatures in the range 550°C to 750°C. The helium was distributed over a depth of several microns in the target by "chopping" a beam of 2 MeV helium ions with Al degrader foils of varying thickness. The helium concentration profile was also "tailored" to closely match the damage energy profile from the 28 MeV silicon ions. This resulted in a damage region extending from a depth of ~0.5 μm to 3 μm in the target over which the helium/dpa ratio was nearly constant. Bombardment with silicon ions has been conducted at the same temperature as the helium pre-injection. Simultaneous bombardment of companion targets with helium and silicon ions has been performed at temperatures identical to those used for the sequentially bombarded targets. Samples were bombarded to peak damage levels of ~30-40 dpa at each temperature. Calculated atomic displacement rates varied from $\sim 6.4 \times 10^{-5}$ dpa.sec^{-1} at the surface to $\sim 1.2 \times 10^{-3}$ dpa.sec^{-1} at the peak damage region. The appm helium/dpa ratio was maintained constant through-

out these experiments at a value of ~11. Following bombardment the targets are being sectioned to various depths corresponding to different damage rates and fluences along the damage energy profile for the silicon ions. To avoid surface proximity and excess silicon effects, data are being taken from a 1.0 to 3.0 μm deep region.

TEM observations reported previously[1] have revealed marked differences in microstructure depending on the helium implantation mode and ion bombardment temperature. In particular, precipitation of second phases, cavity formation and dislocation loop formation are all sensitive to the mode of helium injection at low fluences (~2-10 dpa). In this report we will briefly summarize numerical analyses of cavity size distributions, number densities and swelling. The results will subsequently be compared with data on MFE-I irradiated specimens to determine the extent to which cavity formation at low fluences (in terms of sensitivity to temperature, appm He/dpa, He concentration and pre-irradiation microstructure) depends on damage rate and primary recoil spectra. The data presented must be considered preliminary in nature. Duplicate experiments have been conducted but analysis is not yet complete. In addition, experiments have been conducted at higher appm He/dpa ratios (50:1 and 100:1), higher fluences and intermediate temperatures; and TEM work is in progress.

Figure 1 shows the cavity size distributions for solution-treated 316 SS resulting from simultaneous or sequential (helium preinjected) bombardment at 550°C. The distributions, which were obtained by means of a Zeiss Particle Size Analyzer, appear similar. However, in the case of the helium preinjected specimens, the range of cavity sizes and the maximum cavity size are much larger. This results in an average cavity diameter which is nearly twice that of the simultaneously bombarded specimens. The results are consistent with a recent suggestion by Hayns et al[2] that if stable helium bubbles can be produced with a radius above some critical size, r_c, (as might be expected if all the helium is preinjected at elevated temperature) then rapid growth of these bubbles can occur by bias driven "excess" vacancy absorption. The similar

distribution of cavity sizes for the two different helium injection modes suggests that r_c may be very small for the combination of parameters (gas injection rate, damage rate, sink density and temperature) used in these experiments. Alternatively, the simultaneously implanted helium may drive both continuous nucleation (see Fig. 6) and, by absorption at existing cavities, "subcritical" bubble growth.

At 650°C, Figure 2, the maximum and average cavity sizes increased for both simultaneously and helium preinjected specimens relative to the 550°C irradiation. However, in the simultaneously implanted targets, there was a bimodal distribution of $\sim 10^{15}$ cm^{-2} barely resolvable bubbles and $\sim 10^{13}$ cm^{-2} large cavities. Stereo observations revealed that the large cavities were indeed contained within the foil and were not simply surface artifacts. The maximum cavity size observed exceeded 100 nm, and the appearance of these large cavities increased the measured swelling by a factor of 10 relative to the 550°C irradiation. This explosive growth of a few cavities is not understood at present. If the effect is real, it clearly depends on more than the temperature at which the gas is implanted because the maximum cavity sizes observed in helium pre-injected targets were much smaller. The results point out that "average" sizes can be misleading in interpreting the role of helium in driving bubble/void nucleation and growth. Additional experiments are in progress to determine whether, in fact, the swelling does increase markedly near 650°C.

With the exception of the large cavities observed at 650°C, there was very little difference in maximum cavity size in solution annealed 316 SS specimens under dual-ion irradiation as the irradiation temperature was raised from 550°C to 750°C, Figure 3. The average cavity size appears to saturate at ~650°C. More recent data suggest that the zero order moment of these size distributions resulting from simultaneous helium injection is strongly dose (dpa) dependent.

The appearance of a large number of very small bubbles in the dual-ion irradiated specimens at 550°C and 750°C, Figures 1 and 3 respectively, may indicate the existence of a threshold visibility problem. If slight

differences in magnification, and imaging conditions determine whether or not bubbles will be visible on the electron image plates, the determination of bubble/void nucleation kinetics from cavity size distributions may be difficult. TEM foils from the solution annealed 316 SS which did not show the very fine bubbles are being re-examined using higher magnifications and a variety of imaging conditions.

Prior cold work was very effective in suppressing cavity nucleation and/or growth under dual-ion irradiation conditions but not under sequential ion bombardment, Figure 4. At 600°C no cavities were visible in the simultaneously implanted specimen. At 750°C, Figure 5, cavities were visible in both simultaneously implanted and helium preinjected targets. Here the maximum cavity size and average cavity diameter were much greater in the preinjected specimen in regions where recovery and recrystallization had occurred.

Preliminary results on the temperature dependence of the cavity number density in 316 SS are shown in Figure 6. The effects of thermomechanical processing and time/temperature history of the helium implantation are pronounced at temperature below ~750°C. At lower temperatures (550-650°C), cold work increases the cavity density. This may reflect the increased number of heterogeneous nucleation sites (dislocations and/or helium atoms trapped on dislocations) in the cold-worked specimens. However, it is more likely that the effect is indirect, e.g., a decrease in the effective rate with which dislocations can absorb vacancies because of dislocation pinning by the helium atoms. This is suggested by the previously reported observation[11] that cavities form in cell interiors and not in association with the dislocations comprising the cell walls.

The previously mentioned visibility limitations may have an effect on the low temperature cavity densities. For example, no cavities were visible in the 20% cold worked specimen simultaneously bombarded at 600°C even though the helium atom concentration was $\sim 8 \times 10^{18}$ atoms/cm^3. The increase in cavity concentration over the temperature range 550°C-650°C

for the solution treated material under dual-ion irradiation may reflect continuous nucleation. Alternatively it may simply reflect a failure to observe very small bubbles. This is an important point and strongly suggests the need to make use of some additional "small-defect" techniques which can supplement the information obtainable with conventional TEM.

Figure 7 shows the effects of thermomechanical processing and helium injection mode on the temperature dependence of swelling. In the case of simultaneous implantation, cold work appears to shift the swelling to a higher temperature. Although the swelling data for elevated-temperature pre-implantation of helium are rather inconclusive at this point, it appears that sequential helium implantation generally results in different swelling behavior than simultaneous implantation. Experiments are in progress to obtain additional data and to assess the validity of the simultaneous swelling "peak" at 650°C.

These preliminary results offer little encouragement that pre-implantation of helium in low nickel alloys followed by mixed spectrum or fast reactor irradiation will produce "equivalent" microstructures and mechanical properties compared to specimens in which helium is continuously produced during irradiation. However, higher fluence data over a range of damage rates and appm He/dpa ratios are required.

VI. REFERENCES

1. J. A. Spitznagel and W. J. Choyke, DAFS Quarterly Progress Report No. 3, p. 197, July-September (1978).

2. M. R. Hayns, M. H. Wood and R. Bullough, J. Nucl. Mater. 75, 241 (1978).

VII. FUTURE WORK

Additional experiments at higher doses, different appm He/dpa ratios, and intermediate temperatures will be analyzed to further delineate the effects of initial microstructure and time/temperature history of helium

implantation on cavity, dislocation loop and precipitate nucleation and growth. Initial experiments to determine the effects of the vacuum ambient on cavity nucleation using the high resolution residual gas analyzer system will be conducted.

VIII. PUBLICATIONS

None

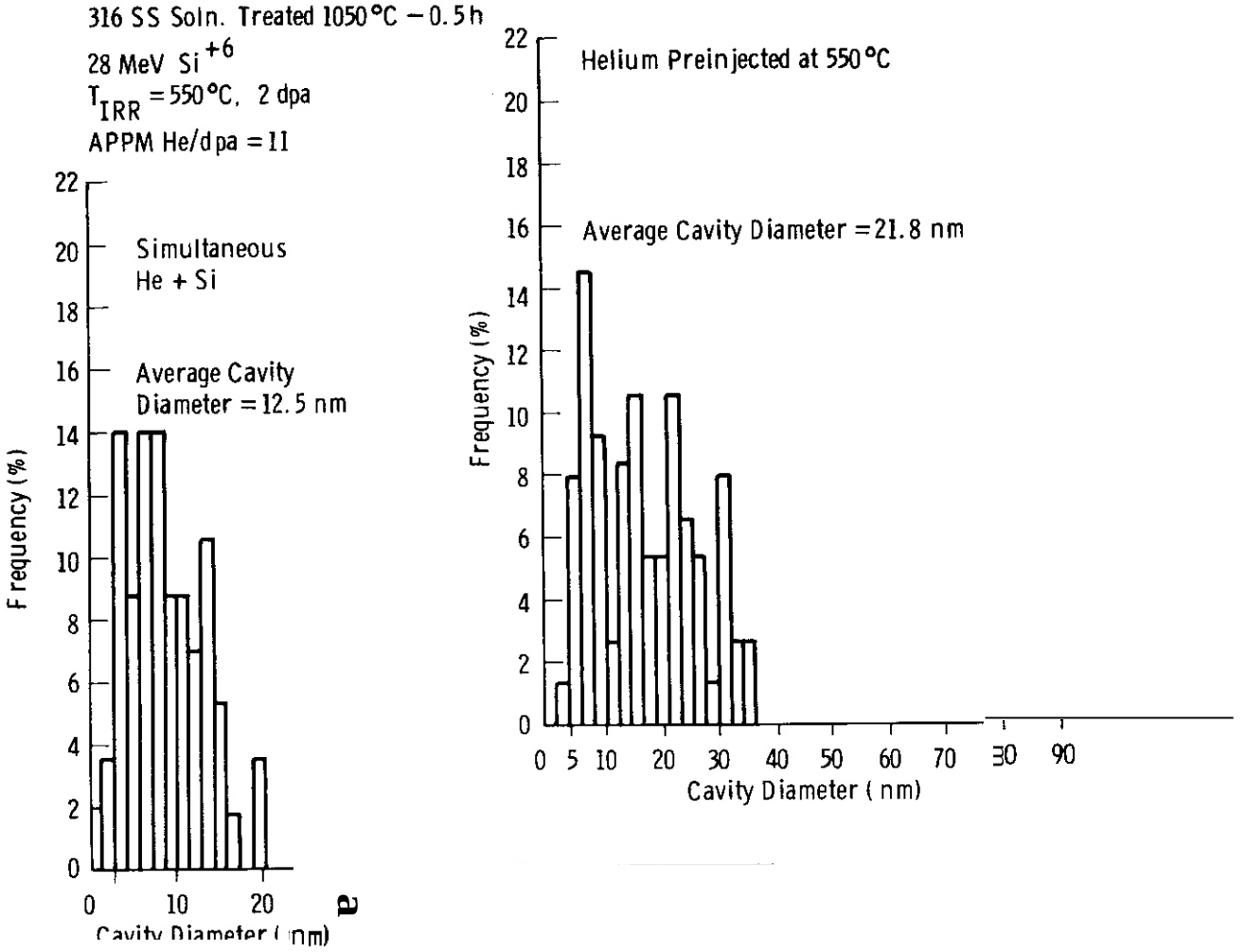

FIGURE 1. Effect of Simultaneous injection or Elevated Temperature Pre-Implantation of Helium on Cavity Size Distribution in Solution Treated 316 SS.

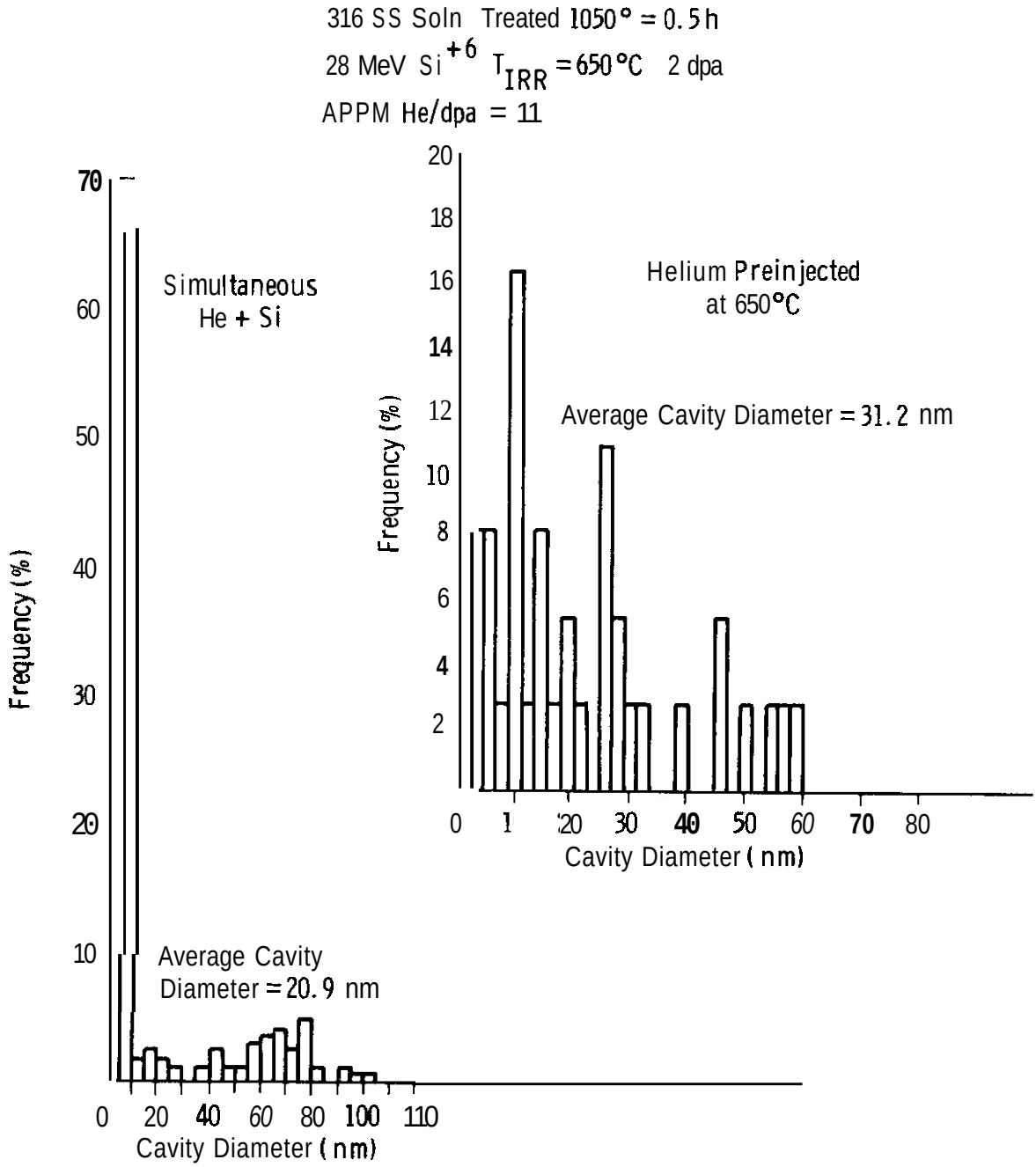

FIGURE 2. Effect of Simultaneous Injection or Elevated Temperature Pre-Implantation of Helium on Cavity Size Distribution in Solution Treated 316 SS.

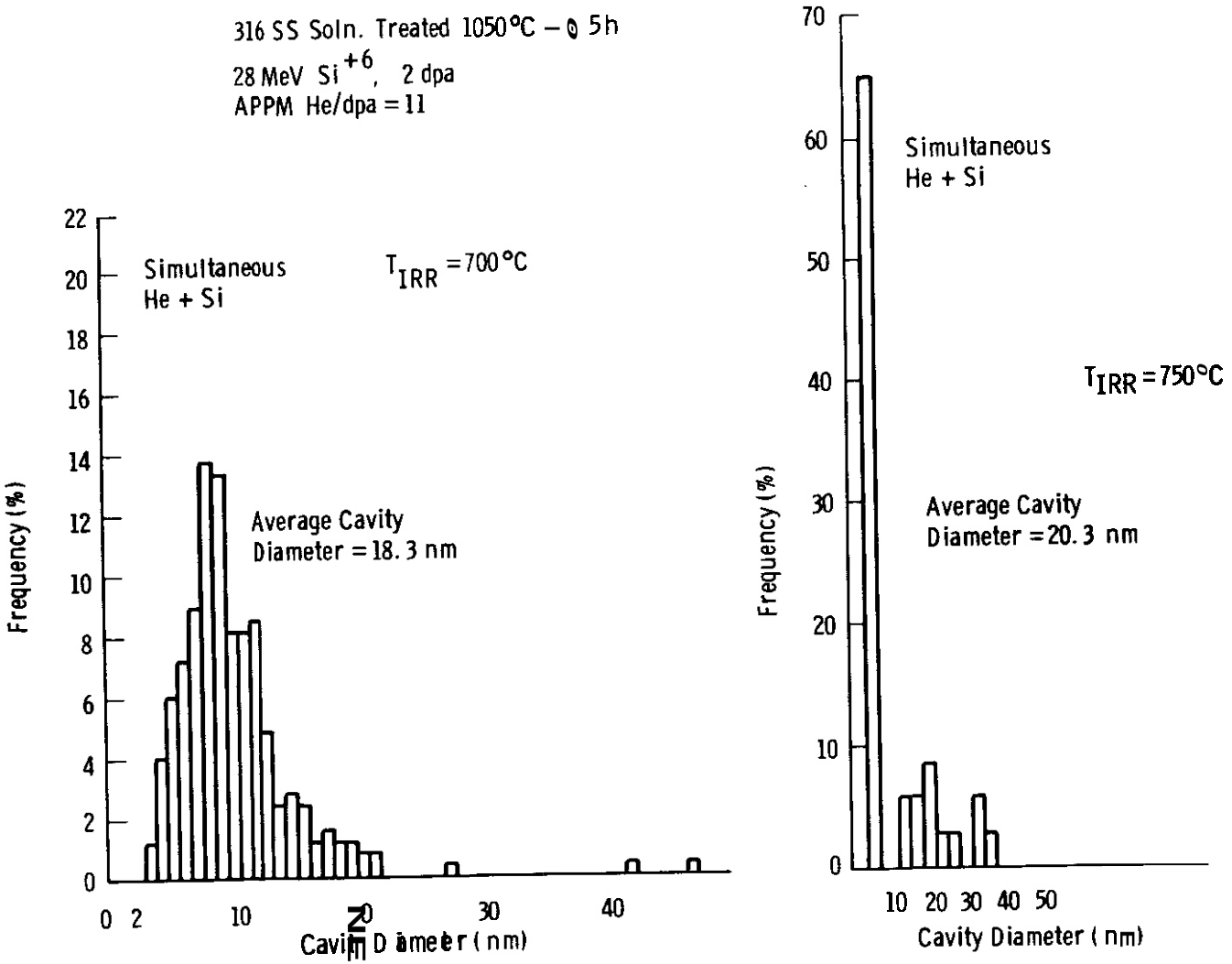

FIGURE 3 Effect of Irradiation Temperatures on Cavity Size Distribution in Dual Ion Irradiated Solution Treated 316 SS.

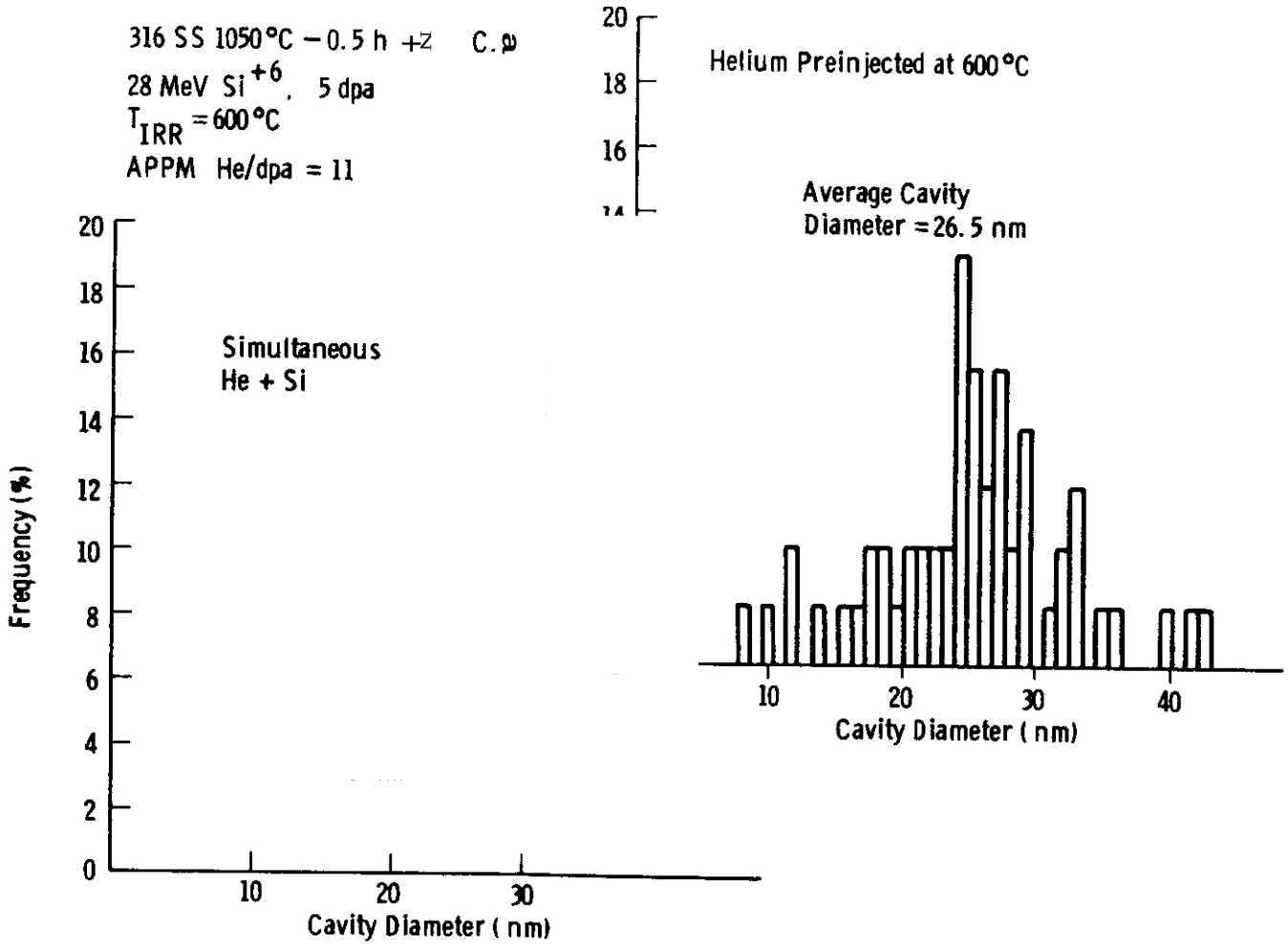

FIGURE 4. Effect of Simultaneous Injection vs. Elevated Temperature Implantation of Helium on Cavity Size Distributions in 20% Cold Rolled 316 SS.

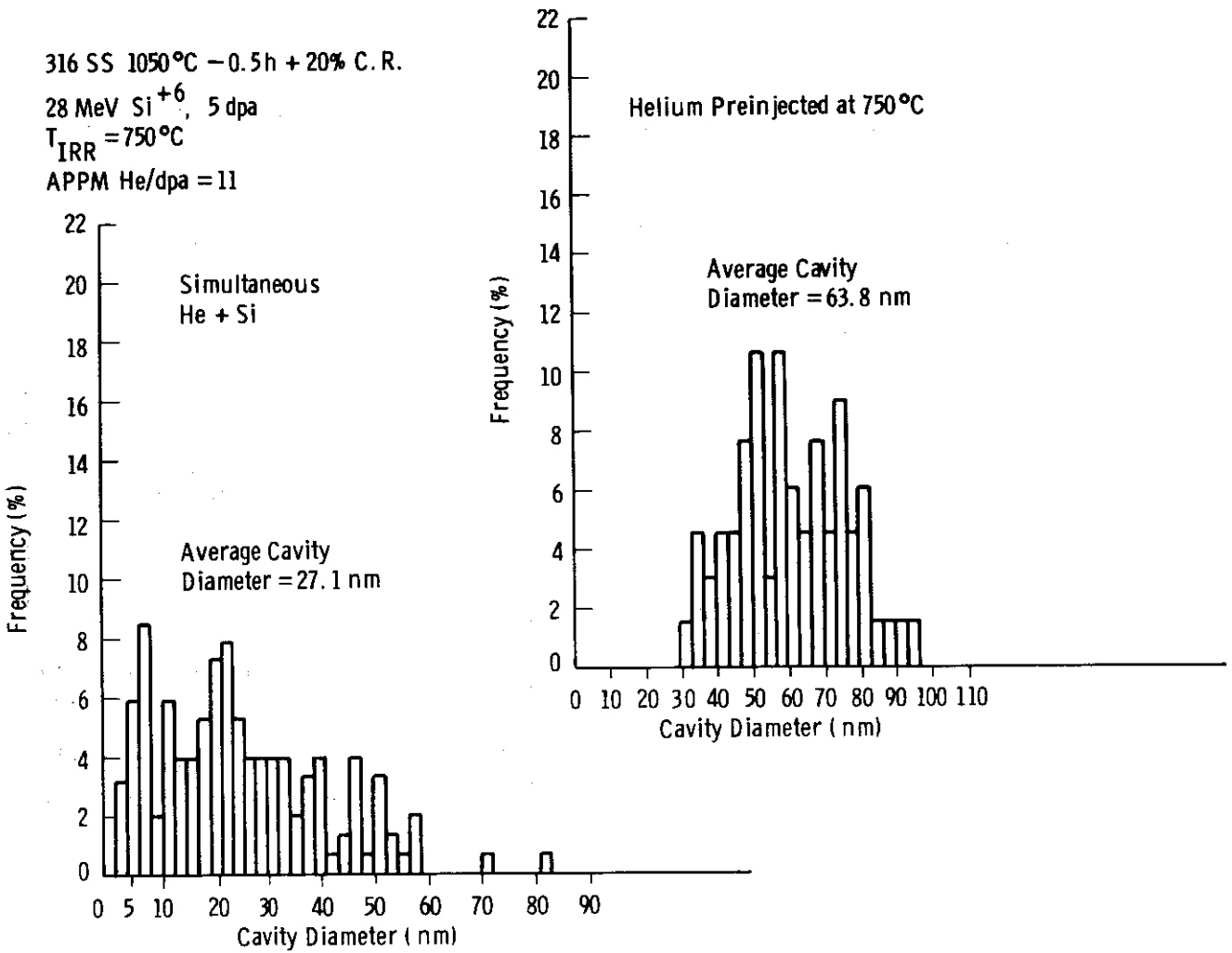

FIGURE 5. Effect of Simultaneous Injection vs. Elevated Temperature Pre-Implantation of Helium on Cavity Size Distributions in 20% Cold Rolled 316 SS.

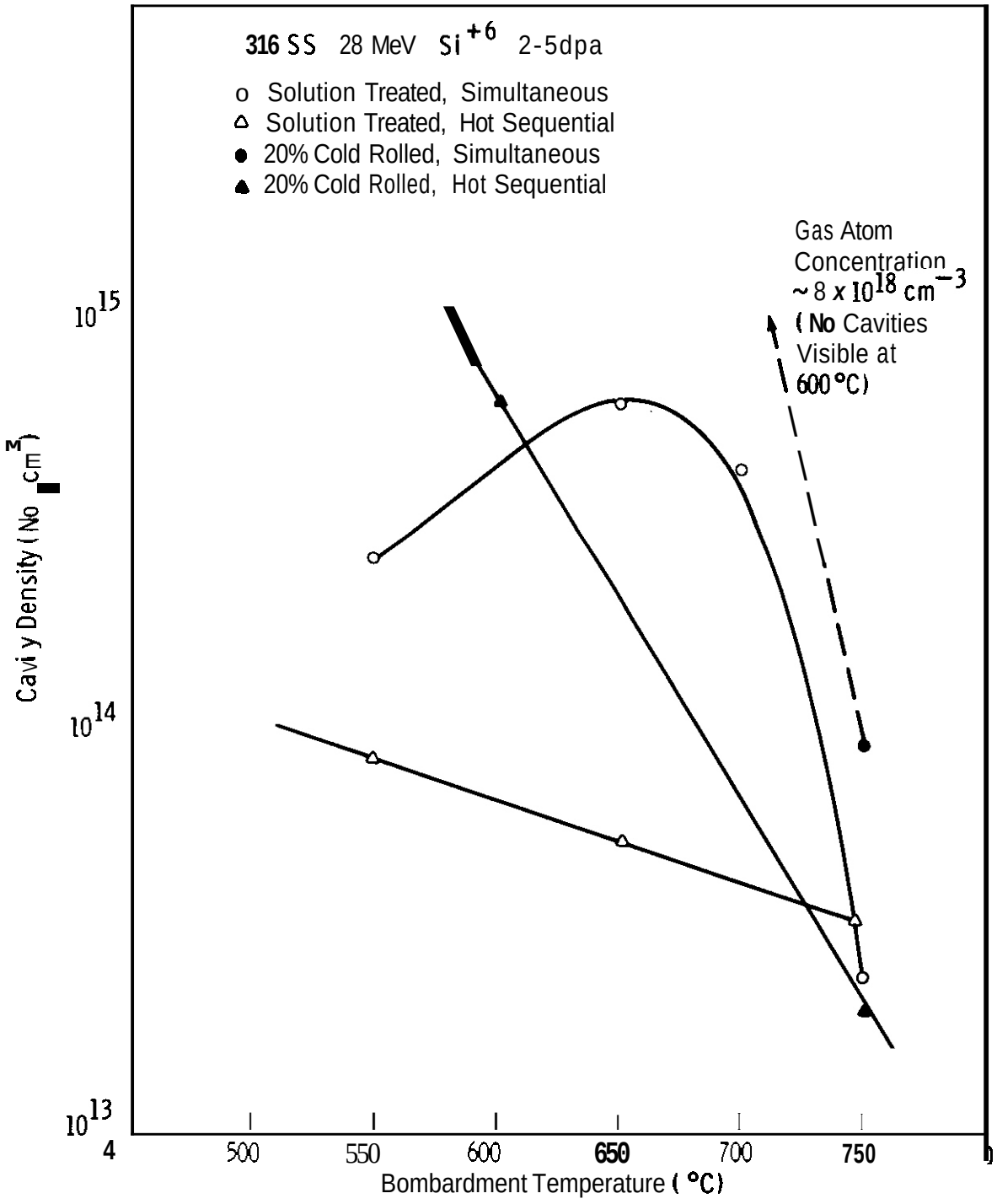

FIGURE 6. Preliminary Comparison of the Effects of Thermomechanical Processing and Simultaneous Injection vs. Elevated Temperature Pre-Implantation of Helium on the Temperature Dependence of the Cavity Number Density in 316 SS.

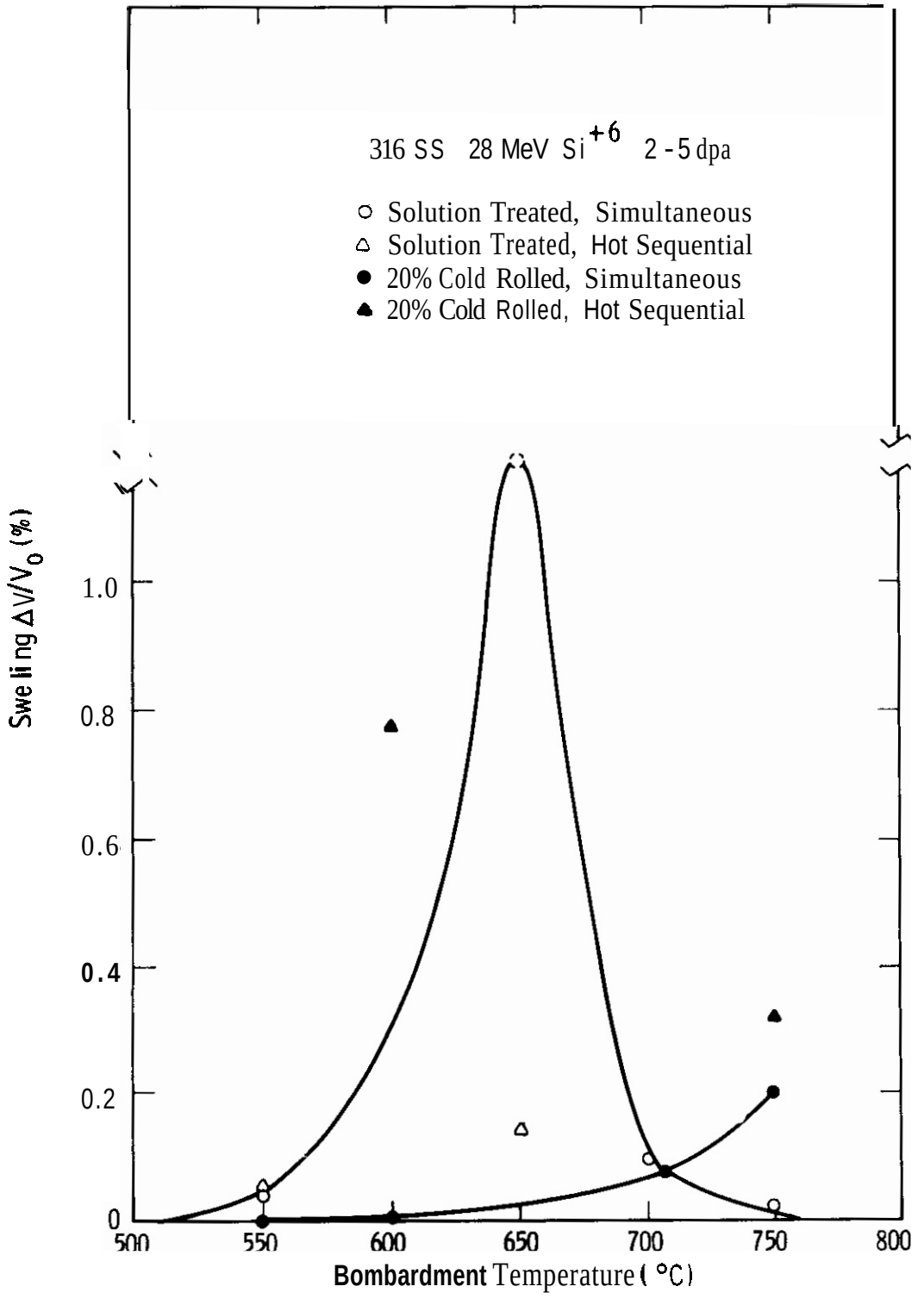

FIGURE 7. Preliminary Comparison of the Effects of Cold Work and Simultaneous Injection versus Elevated Temperature Pre-Implantation of Helium on the Temperature Dependence of Swelling in 316 SS.

uc-20. c

DISTRIBUTION FOR OAFS QUARTERLY REPORTS

UC-20 (117)
UC-20c (78)
APPROVED SPECIAL DISTRIBUTION (82)

Argonne National Laboratory (5)
9700 South Cass Avenue
Argonne, Illinois 60439

L. R. Greenwood
S. D. Harkness
V. H. Maroni
F. V. Nolfi, Jr.
H. Wiedersich

Atomics International (1)
Component Engineering and Technology Division
North American Rockwell
8900 DeSoto Avenue
Canoga Park, California 91304

H. Farrar, IV

Battelle-Northwest (5)
P. O. Box 999
Richland, Washington 99352

J. L. Brimhall
A. B. Johnson
R. H. Jones
L. C. Schmid
D. Styris

Brookhaven National Laboratory (2)
Associated Universities
Upton, New York 11973

Chairman, Department of Nuclear Energy
A. N. Goland

DISTRIBUTION (cont'd.)

Department of Energy
Washington, D.C. 20545

Office of Fusion Energy (6)
J. F. Clarke, ETM
F. E. Coffman, ETM
N. A. Davies, ETM
J. F. Decker, ETM
E. E. Kintner, ETM
M. Roberts, ETM

Materials and Radiation Effects Branch, ETM (25)

Assistant Director for Materials Technology, RRT (2)
J. W. Bennett
P. B. Hemmig

General Atomic Company (3)
P. O. Box 81608
San Diego, California 92138

G. R. Hopkins
S. Rosenwasser
L. Rovner

Lawrence Livermore Laboratory (2)
University of California
P. O. Box-808
Livermore, California 94550

M. W. Guinan
C. M. Logan

Los Alamos Scientific Laboratory (3)
University of California
P. O. Box 1663
Los Alamos, New Mexico 87544

O. J. Dudziak
W. Green
D. M. Parkin

DISTRIBUTION (cont'd)

Massachusetts Institute of Technology (2)
Cambridge, Massachusetts 02139

O. K. Harling
K. C. Russell

McDonnell-Douglas Astronautics (2)
P. O. Box 516
St. Louis, Missouri 63166

J. Davis
D. Kummer

Mound Laboratory (1)
P. O. Box 32
Miamisburg, Ohio 45342

Manager, Technology Applications and Development

Naval Research Laboratory (3)
Metallurgy Division, Code 6390
Washington, D. C. 20375

I. Manning
F. A. Smidt
J. A. Sprague

North Carolina State University (1)
Department of Nuclear Engineering
Raleigh, North Carolina 26707

J. R. Beeler, Jr.

Oak Ridge National Laboratory (6)
P. O. Box Y
Oak Ridge, Tennessee 37830

Director, Thermonuclear Division, Bldg. 9201-2
L. A. Berry
R. J. Colchin, Bldg. 9201-2
F. G. Perey
C. Weisbin

DISTRIBUTION (cont'd)

Plasma Physics Laboratory (3)
Princeton University
P. O. Box 451
Princeton, New Jersey 08540

C. Osgood
W. Price
K. Wakefield

Sandia Laboratories (2)
Albuquerque, New Mexico 87115

F. L. Vook

Sandia Laboratories (3)
Livermore, California 94550

W. Bauer (2)
W. Wilson

University of Michigan (1)
Nuclear Engineering Department
College of Engineering
Ann Arbor, Michigan 48105

T. Kammash

Westinghouse Electric Corporation (3)
Research and Development Center
Beulah Road
Pittsburgh, Pennsylvania 15234

J. Choyka
H. R. Holland
J. A. Spetznagel

*U.S. GOVERNMENT PRINTING OFFICE : 1979 0-281-704/42